36427

National Library of Canada | Bibliothèque nationale du Canada

CANADIAN THESES ON MICROFICHE | THÈSES CANADIENNES SUR MICROFICHE

NAME OF AUTHOR/*NOM DE L'AUTEUR* ROBERT HUGH McCAMIS

TITLE OF THESIS/*TITRE DE LA THÈSE* BACKWARD ANGLE CROSS SECTIONS AND ANALYZING POWERS FOR PROTON ELASTIC SCATTERING FROM HELIUM-4 AT INTERMEDIATE ENERGIES

UNIVERSITY/*UNIVERSITÉ* ALBERTA

DEGREE FOR WHICH THESIS WAS PRESENTED/*GRADE POUR LEQUEL CETTE THÈSE FUT PRÉSENTÉE* DOCTOR OF PHILOSOPHY

YEAR THIS DEGREE CONFERRED/*ANNÉE D'OBTENTION DE CE GRADE* 1978

NAME OF SUPERVISOR/*NOM DU DIRECTEUR DE THÈSE* DR. G. A. MOSS

Permission is hereby granted to the NATIONAL LIBRARY OF CANADA to microfilm this thesis and to lend or sell copies of the film.

The author reserves other publication rights, and neither the thesis nor extensive extracts from it may be printed or otherwise reproduced without the author's written permission.

L'autorisation est, par la présente, accordée à la BIBLIOTHÈQUE NATIONALE DU CANADA de microfilmer cette thèse et de prêter ou de vendre des exemplaires du film.

L'auteur se réserve les autres droits de publication; ni la thèse ni de longs extraits de celle-ci ne doivent être imprimés ou autrement reproduits sans l'autorisation écrite de l'auteur.

DATED/*DATÉ* FEBRUARY 7, 1978 SIGNED/*SIGNÉ* R H McCamis

PERMANENT ADDRESS/*RÉSIDENCE FIXÉ* DEPARTMENT OF PHYSICS
UNIVERSITY OF MANITOBA
WINNIPEG, MANITOBA R3T-2N2

NL-91 (3-74)

National Library of Canada

Cataloguing Branch
Canadian Theses Division

Ottawa, Canada
K1A 0N4

Bibliothèque nationale du Canada

Direction du catalogage
Division des thèses canadiennes

NOTICE

The quality of this microfiche is heavily dependent upon the quality of the original thesis submitted for microfilming. Every effort has been made to ensure the highest quality of reproduction possible.

If pages are missing, contact the university which granted the degree.

Some pages may have indistinct print especially if the original pages were typed with a poor typewriter ribbon or if the university sent us a poor photocopy.

Previously copyrighted materials (journal articles, published tests, etc.) are not filmed.

Reproduction in full or in part of this film is governed by the Canadian Copyright Act, R.S.C. 1970, c. C-30. Please read the authorization forms which accompany this thesis.

AVIS

La qualité de cette microfiche dépend grandement de la qualité de la thèse soumise au microfilmage. Nous avons tout fait pour assurer une qualité supérieure de reproduction.

S'il manque des pages, veuillez communiquer avec l'université qui a conféré le grade.

La qualité d'impression de certaines pages peut laisser à désirer, surtout si les pages originales ont été dactylographiées à l'aide d'un ruban usé ou si l'université nous a fait parvenir une photocopie de mauvaise qualité.

Les documents qui font déjà l'objet d'un droit d'auteur (articles de revue, examens publiés, etc.) ne sont pas microfilmés.

La reproduction, même partielle, de ce microfilm est soumise à la Loi canadienne sur le droit d'auteur, SRC 1970, c. C-30. Veuillez prendre connaissance des formules d'autorisation qui accompagnent cette thèse.

THIS DISSERTATION
HAS BEEN MICROFILMED
EXACTLY AS RECEIVED

LA THÈSE A ÉTÉ
MICROFILMÉE TELLE QUE
NOUS L'AVONS REÇUE

NL-339 (3/77)

THE UNIVERSITY OF ALBERTA

BACKWARD ANGLE CROSS SECTIONS AND ANALYZING POWERS FOR PROTON ELASTIC SCATTERING FROM HELIUM-4 AT INTERMEDIATE ENERGIES

by

© ROBERT HUGH McCAMIS

A THESIS

SUBMITTED TO THE FACULTY OF GRADUATE STUDIES AND RESEARCH IN

PARTIAL FULFILMENT OF THE REQUIREMENTS FOR THE DEGREE OF

DOCTOR OF PHILOSOPHY

in

NUCLEAR PHYSICS

DEPARTMENT OF PHYSICS

EDMONTON, ALBERTA

SPRING, 1978

THE UNIVERSITY OF ALBERTA

FACULTY OF GRADUATE STUDIES AND RESEARCH

The undersigned certify that they have read, and recommend to the Faculty of Graduate Studies and Research, for acceptance, a thesis entitled "Backward Angle Cross Sections and Analyzing Powers for Proton Elastic Scattering from Helium-4 at Intermediate Energies," submitted by Robert Hugh McCamis in partial fulfilment of the requirements for the degree of Doctor of Philosophy in Nuclear Physics.

G.A. Moss
Supervisor

G. Roy

P. Kitching

J.B. Kennaher

F.E. Vonmeulen

R.D. Klem
External Examiner

Date 11 January 1978

ABSTRACT

Backward elastic scattering of protons from ^{4}He in the intermediate energy region has been studied by measuring differential cross sections for ten proton energies between 185 and 500 MeV in the angular range 144^0 to 168^0 in the laboratory system. The p-^{4}He analyzing powers have also been measured for seven energies in the same angular region. In addition, differential cross sections at six proton energies and analyzing powers at three energies are also presented for the reaction ^{4}He (p,d) ^{3}He.

The elastic scattering differential cross sections do not show the marked backward peaking that has been observed at both lower and higher energies. The possible structure in the 180^0 elastic scattering excitation function suggested for energies near 240 MeV is not observed. The analyzing powers are large and negative, and show strong dependence on both energy and angle. Changes in the cross section angular distributions, the analyzing power angular distributions, and the 180^0 excitation function are all evident near 200 MeV. The results obtained in this experiment are compared to previous measurements.

In contrast, the ^{4}He (p,d) ^{3}He differential cross sections are strongly backward peaked. The cross sections and the 180^0 excitation function for ^{4}He (p,d) are very similar to those for the ^{3}He (p,p) reaction. The ^{4}He (p,d) analyzing powers are small and negative, and show less energy dependence than do the p-^{4}He elastic scattering analyzing powers.

Several theoretical interpretations applicable to these data are discussed. The elastic scattering results are not in close agreement with existing triton exchange model calculations at the lower energies. Some phenomenological comparisons of the ^{4}He (p,p) and ^{4}He (p,d) cross sections are discussed. Suggestions are made for possible theoretical calculations and for future experimental measurements which may clarify the reaction mechanisms involved.

ACKNOWLEDGEMENTS

I am very grateful to my supervisor, Dr. G. A. Moss, for his assistance and guidance throughout all phases of this project.

I greatly appreciate the keen interest and support of Dr. J. M. Cameron, who contributed to the experiment in many ways.

I am grateful to Dr. C. A. Goulding, whose enthusiasm warmed me to the subject of cryogenics. My special thanks go to Dr. D. A. Hutcheon, Dr. C. A. Miller, and Dr. J. G. Rogers for their patient explanations and their able assistance in so many aspects of this work. I also wish to thank the other members of the elastic scattering group, Mr. M. S. de Jong, Dr. L. G. Greeniaus, Dr. B. T. Murdoch, Dr. G. Roy, Dr. A. W. Stetz, and Dr. W. T. H. Van Oers for their invaluable assistance in the preparation of the apparatus, in the data collection, and for many helpful discussions. In particular, the assistance of Mr. de Jong and Drs. Goulding, Murdoch and Van Oers in the commissioning and operation of the liquid target is gratefully acknowledged.

I am very grateful to Randy Churchman and Herb Coombes for their outstanding technical support in keeping the equipment running so well, for their explanations of many electronic gadgets, and for their friendship.

The assistance of countless operators, technicians, and other support staff who made TRIUMF such an excellent facility is gratefully acknowledged. I am grateful to Dr. J. R. Richardson and

Dr. J. T. Sample for their support.

I wish to thank Dr. H. W. Fearing, Dr. J. Kallne, Dr. H. S. Sherif, and Dr. A. W. Thomas for many enlightening discussions.

A very special thanks goes to my typists, my wife, Betty, and Miss M. Lowe, for doing such an excellent job of typing this thesis, in spite of many complications and early deadlines.

The financial assistance of the Atomic Energy Control Board, the National Research Council of Canada, and the University of Alberta during the course of this work is gratefully acknowledged.

Finally, my greatest thanks and appreciation go to my loving wife, Betty, for everything that she has done to make this thesis a reality, and for her many sacrifices towards that end.

To Betty

November, 1977

TABLE OF CONTENTS

CHAPTER		PAGE
I.	INTRODUCTION	1
II.	EXPERIMENTAL APPARATUS	6
	2.1 Choice of Method	6
	2.2 The Accelerator and the Beam Line	10
	2.3 The Liquid ^{4}He Target	13
	2.3.1 The Cryogenics of the Target	13
	2.3.2 The Target Positioning Mechanism	19
	2.4 The Scattering Chambers and the Detectors	22
	2.4.1 The Scattering Chamber	22
	2.4.2 The Polarimeter	24
	2.4.3 The Principal Detectors	25
	2.4.4 The Monitor Counters	31
	2.5 The Electronic System and Data Acquisition	35
	2.5.1 The Backward Angle Electronics	35
	2.5.2 The Target Thickness Electronics	42
	2.5.3 The Monitor Electronics	45
	2.5.4 The Polarimeter Electronics	48
	2.5.5 The Data Acquisition System	48
	2.6 Data Analysis	54
	2.7 Dead Time Corrections	63
III.	EXPERIMENTAL RESULTS	67
	3.1 Normalizations	67

CHAPTER PAGE

3.1.1 Beam Flux Normalizations 67

3.1.2 Target Thickness Determination 71

3.1.3 Target Bubbling Tests 77

3.1.4 The Target Thickness and Beam Movements ... 78

3.2 Data Corrections and Uncertainties 81

3.2.1 Data Corrections 81

3.2.2 Data Uncertainties 82

3.3 The Elastic Scattering Differential Cross Sections . 86

3.4 The Elastic Scattering Analyzing Powers 97

3.4.1 The Beam Polarization Calibration 97

3.4.2 Calculation of the Analyzing Powers 100

3.4.3 The Elastic Scattering Analyzing Powers .. 102

IV. THEORETICAL INTERPRETATIONS 109

4.1 The Triton Exchange Model 109

4.2 Non-Eikonal Multiple Scattering Model 116

4.3 Nucleon Isobar Models 120

4.4 Phenomenology of the Present Cross Sections 122

V. CONCLUSIONS 131

***

REFERENCES 134

APPENDIX A. $^{4}He(p,d)^{3}He$ DIFFERENTIAL CROSS SECTIONS AND ANALYZING POWERS 141

APPENDIX B. MANDELSTAM VARIABLES 155

LIST OF TABLES

TABLE		PAGE
1.	Signals Scaled	43
2.	ORION Magnetic Tape Event Structure	51
3.	Spectra Stored in Memory	53
4.	Ion Chamber Gain vs. Proton Energy	70
5.	Target Thickness Information	75
6.	Elastic Scattering Cross Sections	89
7.	Polarimeter Analyzing Powers	99
8.	Elastic Scattering Analyzing Powers	103
9.	^{4}He(p,d) Cross Sections	146
10.	^{4}He(p,d) Analyzing Powers	151

LIST OF FIGURES

FIGURE		PAGE
1.	A plot of the kinematics for the reaction p + ^{4}He → p + ^{4}He in the region of interest, showing the correlation between the ^{4}He lab. angle and the proton lab. angle.	8
2.	Kinematics for the reaction p + ^{4}He → p + ^{4}He: (a) proton energy vs. proton lab. angle and (b) ^{4}He energy vs. ^{4}He lab. angle.	9
3.	A schematic diagram of the beam line 4B beam transport system.	11
4.	The helium target cryogenic details, with (a) fill inlet, (b) interior pressure gauge, (c) gas boiloff line, (d) mechanical coupling, (e) vacuum system connection, (f) outer and (g) inner radiation shields, (h) main liquid ^{4}He vessel, (i) cell boiloff standpipe, (j) fill tube receptacle, (k) target cell, (l) dummy cell, (m) vertical position stop ring, (n) rotation sprocket key, (o) spacer bolts (1 of 3 shown), (p) radiation shield extension, (q) bottom spacers, and (r) scintillation screen. The scale is approximate, especially for small dimensions.	14
5.	The ^{4}He target cell, showing the method of attaching the cell to the tubes from the main liquid reservoir.	16
6.	The target rotation and elevation mechanism, showing (A) the low position, and (B) the middle position. Details include (a) the main cryostat, (b) rotation motor, (c) chain and sprocket drive, (d) pneumatic cylinder, (e) compressed air inlet, (f) stop defining middle position, (g) sprocket retention bearing, (h) scattering chamber, (i) beam line vacuum, (j) Kapton windows, (k) beam plane, (l) elevation expansion volume, and (m) added O-ring seal.	20
7.	A schematic diagram of the scattering chamber and the experimental apparatus.	23
8.	The correction to the measured polarimeter asymmetry due to the carbon contribution as a function of beam energy.	26

FIGURE		PAGE
9.	The positions of the MWPC's and the other detectors upon the four booms.	28
10.	The efficiency of the central region of the telescope (as discussed in the text and (Ca-77)) as a function of incident proton energy (taken from (Ca-77)). Where not shown, the uncertainty in the measured value is less than the size of the point. The solid line is a calculation (St-75) using reaction cross sections.	32
11.	A schematic block diagram of the electronics used for the back angle measurements.	36
12.	A block diagram of the electronics located in the experimental hall which were used for the back angle measurements. The legend in this figure is common to all of the electronics diagrams.	37
13.	A block diagram of the first portion of the electronics located in the remote counting room, used for the back angle measurements (continued in Figure 14). The relative timing of various signals is shown at key points (all pulse widths are in nsec). The low pass filters (LPF's) removed high frequency noise originating in the NaI amplifiers.	39
14.	The second portion of the electronics located in the remote counting room, used for both the back angle and target thickness measurements.	40
15.	The electronics in the experimental hall which were used for the target thickness measurements.	44
16.	The portion of the electronics, located in the remote counting room, associated with the target thickness measurements.	46
17.	A block diagram of the stationary monitor counter electronics.	47
18.	A block diagram of the polarimeter electronics.	49
19.	A typical, on-line E_p-vs.-E_α spectrum, taken at E_{beam} = 350 MeV, $\theta_p = 152^0$, $\theta_\alpha = 10^0$. The lines show the preliminary energy windows used to define elastic scattering events.	56
20.	The on-line, front-back timing spectrum corresponding to Figure 19.	57

FIGURE		PAGE
21.	(a) The events of Figure 19 projected onto the E_p axis. The dashed lines show the preliminary energy window indicated in Figure 19. (b) The same data as (a), but with a timing window applied. The final energy window defining elastic scattering events is indicated by the dashed lines.	59
22.	An on-line spectrum of events plotted as a function of proton energy, showing a prominent inelastic proton scattering peak. The spectrum was obtained for an energy of 185 MeV for $\Theta_p = 158^0$.	60
23.	An on-line E_p-vs.-E_α spectrum with an empty target, taken at an energy of 350 MeV for $\Theta_p = 168^0$, $\Theta_\alpha = 4^0$. The windows indicated are the windows used to define elastic scattering events for a full target run (Figure 19).	62
24.	A block diagram of the electronic system that provided the 'dead time' pulses.	65
25.	A plot of the ion chamber gain as a function of beam energy. The measured points are circled. The curve is proportional to the energy loss of protons in helium. The other points were obtained assuming the proportionality of the gain to the proton energy loss.	69
26.	A plot of the results of the target bubbling tests as a function of the incident beam current. The error bars indicate statistical uncertainties only. The solid line is the weighted mean of the six points, with the statistical uncertainty in this value indicated by the dashed lines.	79
27.	A scale diagram of a cross section of the target cell, with a typical beam spot. The shape of the bowed windows is schematic only.	80
28.	The elastic scattering differential cross sections as functions of $\cos \Theta_{cm}$ and Θ_{cm}. The lines represent an exponential fit to the data as a function of $\cos \Theta_{cm}$.	92
29.	The elastic scattering cross sections extrapolated to 180^0, as a function of proton energy. The pluses are the present data, the circles are data from previous experiments (see text for references).	95

FIGURE PAGE

30. The elastic scattering differential cross sections vs. cos Θ_{cm}, for the following energies: ⊙: 185 MeV, present data; ⊡: 300 MeV, present data; ▲: 440 MeV, present data; ●: 147 MeV, (Co-59); +: 156 MeV, (Co-75); ⊗: 298 MeV, (Be-76b); x: 438 MeV, (Be-76b); ⊕: 648 MeV, (Be-76b). The curves are triton exchange model calculations (Le-76) at 298, 438 and 648 MeV. 96

31. The elastic scattering analyzing powers as a function of Θ_{lab}, shown separately for each beam energy. The uncertainties shown are the statistical uncertainties only. The data indicated by crosses in (a) are from (Co-59) at 147 MeV. 105

32. A contour plot of the elastic scattering analyzing powers as functions of Θ_{lab} and proton energy. The straight lines indicate the range of the measurements at each energy. 107

33. (a) A pictorial representation of the triton exchange mechanism for p-^{4}He elastic scattering. (b) A similar representation for the direct scattering mechanism. (c) The symbolic diagram for triton exchange. (d) The triton exchange diagram including absorption in both entrance and exit channels. 110

34. The ^{4}He single particle wave function in momentum representation as a function of Q^2. 113

35. Multiple scattering diagrams for a hadron 'x' scattering from a nucleus 'A': (a) single scattering, (b) double scattering, (c) triple scattering, and (d) quadruple scattering. 118

36. Proton-deuteron backward elastic scattering via (a) nucleon exchange, (b) nucleon isobar exchange, and (c) the 'triangle' mechanism. 121

37. The elastic scattering differential cross sections plotted as a function of the variable 'u'. The curve is the expected u-dependence of the cross section, if the reaction is dominated by triton exchange. 124

38. The elastic scattering differential cross sections as a function of the variable '-t'. The curve proportional to $t^{-2.5}$ is purely phenomenological, to show the trends of the data. 125

FIGURE

PAGE

39. The $^4He(p,d)^3He$ differential cross sections as a function of the variable 'u'. The curve shows the u-dependence expected if the reaction is dominated by deuteron exchange. 127

40. The $^4He(p,d)^3He$ differential cross sections as a function of the variable '-t'. 128

41. (a) The triton exchange diagram for p-^{4}He elastic scattering. (b) The deuteron exchange diagram for the reaction $p + {}^4He \rightarrow d + {}^3He$. (c) The deuteron exchange diagram for p-^{3}He elastic scattering. 129

42. The differential cross sections for the reaction $^4He(p,d)^3He$ vs. cos Θ_{cm} and Θ_{cm}. The lines represent an exponential fit to the data as a function of cos Θ_{cm}. 148

43. The ratios of the 180^0 extrapolated cross sections for the reactions indicated as a function of proton energy. 149

44. The analyzing powers for the reaction $^4He(p,d)^3He$ as a function of Θ_{lab}, shown separately for each beam energy. The uncertainties shown are the statistical uncertainties only. 152

45. A diagram of the general process a + b → c + d, in the center of mass system. 157

CHAPTER I

INTRODUCTION

The goal of this study was to measure differential cross sections and analyzing powers for proton elastic scattering on helium-4 at large scattering angles for energies between 185 MeV and 500 MeV. If one employs a particle exchange mechanism to explain the backward scattering cross sections, then it is expected that the large momentum components of the wave function of the exchanged particle in the initial nucleus are probed and considerable nuclear structure information could be extracted. Comprehensive polarization angular distributions in the backward direction would also aid in clarifying the details of the reaction mechanism, as one is then sensitive to interference between different amplitudes. The motivation behind the experiment, then, was to provide data which would assist in testing recent theoretical predictions in this region.

One of the first experiments on proton-^{4}He elastic scattering at intermediate (approximately 200-800 MeV) or high energies ($\geq$ 800 MeV) was done by Palevsky *et al.* (Pa-67) at 1 GeV. Another early experiment was by McManigal *et al.* (McM-65) at 725 MeV but over a limited angular range. Shortly thereafter, Boschitz *et al.* (Bo-68) and Gotow *et al.* (Go-68) did experiments at 587 MeV and 540 MeV, respectively. However, it was not until a measurement by Baker *et al.* (Ba-74) which repeated the 1 GeV experiment and showed an important difference from the Palevsky data (Pa-67) that the interest in p-^{4}He

scattering broadened considerably. Many theoretical papers followed the early data. Most of these discussed the 1 GeV data (for example, see Ba-67, Cz-67, Ku-70, Ik-72 and Gu-75). Other experiments followed at 156 MeV (Co-75), 580 and 720 MeV (Ve-75), 600 MeV (Fa-76), 438, 648 and 1036 MeV (Be-76a), and at 350, 650, 1050, and 1150 MeV (As-77). The 1050 MeV data of (As-77) provided the absolute normalization of the Baker data, which was arbitrarily normalized. The majority of these experiments concentrated on the first minimum in the differential cross section, the region of the discrepancy in the 1 GeV data. Two very recent experiments (Ge-77 and Kl-77) independently remeasured the cross sections at 1 GeV and both experiments favoured the Baker data in shape, although they disagreed in absolute magnitude. A recent calculation (Wa-77) of a multiple-diffraction theory, including the effects of the $\Delta(1236)$-intermediate state process agreed with the latest experiments (Ge-77 and Kl-77).

A common characteristic of these data was that they were limited to forward angles. Few data points (except Co-75) were taken past $\theta_{cm} \simeq 50\text{-}70^0$. The intermediate angle region and the back angle region above 156 MeV were largely unexplored. A second limitation was that little polarization data existed. Experiments having polarization measurements included only McManigal (McM-65), Gotow (Go-68), and Klem et al. (Kl-77a), again all in the forward region.

Recently, however, Berger et al. (Be-76b) measured backward p-^{4}He elastic scattering cross sections at equivalent proton energies (their experiment used a helium-4 beam on a H_2 target) of 298, 438,

648 and 840 MeV and found some very interesting results. They reported that the slope of the cross section near $\theta_{cm} = 180^0$ was mildly negative at 298 MeV, slightly positive at 438 MeV, and sharply positive at 648 and 840 MeV.

Previous experiments extending to the backward region at 100 MeV (Go-70), 147 MeV (Co-59) and 156 MeV (Co-75) all showed strong backward peaking of the cross section. Only Cormack et al. (Co-59) reported measuring polarizations in the region. A single data point also existed at 665 MeV at $\theta_{cm} = 169^0$ (Ko-70).

In contrast to the scarcity of p-^{4}He data, however, p-d backward elastic scattering has been exhaustively studied. From 14 MeV to 2.5 GeV proton laboratory energy, the experimental data display a backward peak rising from 140^0 to 180^0 c.m. by typically one order of magnitude (Du-74 and We-77). Many experiments (for example, Vi-70, Al-72, Ko-73a and references in Du-74) have also documented the 'bump' in the extrapolated 180^0 p-d elastic scattering cross section as a function of energy between 300 and 1000 MeV. While one-nucleon exchange dominates the low-energy 180^0 cross sections (Du-74), much speculation has taken place over the cause of this 'bump'. N*-isobar exchange (Ke-69) and meson-plus-nucleon exchange, the so-called triangle graphs (Cr-69 and Ko-73b, for example) have been among the mechanisms proposed, but neither approach has been adequately shown to be solely responsible for the observed phenomena (No-74 and We-77).

Frascaria et al. (Fr-77) have measured p-^{3}He backward elastic scattering cross sections at 415, 600 and 800 MeV. Their data showed

small backward peaking and a much broader and less pronounced bump in the 180^0 excitation function than was evident for the p-d case.

Returning to the p-^{4}He picture at backward angles, Kopeliovich and Potashnikova (Ko-71) performed a calculation in terms of the triton exchange model and predicted a sharp dip in the 180^0 excitation function for p-^{4}He scattering at approximately 190 MeV. After the recent Berger experiment (Be-76b) was performed, Lesniak, Lesniak and Tekou (Le-76) did further calculations on the triton exchange model. Whereas Kopeliovich and Potashnikova used the plane wave Born approximation (PWBA), Lesniak et al. improved the theory by taking into account the distortion of both the incoming and outgoing waves, an effect found to be most important in that the PWBA cross sections were reduced by one to two orders of magnitude at 438 and 648 MeV. Their theoretical calculations fit the experimental results (Be-76b) fairly well in magnitude, although the shapes of the angular distributions of the cross sections were not reproduced, especially at 298 MeV. They also suggested that a minimum might occur in the 180^0 excitation function near 240 MeV. Lesniak et al. qualified this by adding: "This structure at 240 MeV may be however displaced by several tens of MeV or partially filled in by absorption effects." They went on to state: "The width of the minimum (if present) may be of the order of 40 MeV or less." This theory, and others which may also be important in backward p-^{4}He scattering will be discussed in Chapter IV.

It was decided to use the unique properties of the TRIUMF cyclotron (polarized beam, easily variable energy and excellent energy definition) to investigate p-^{4}He backward scattering in this important energy region. Cross section data were taken at ten energies between 185 MeV and 500 MeV, employing small (25 MeV) energy increments below 300 MeV in a careful search for the predicted structure in the cross sections. The analyzing powers were measured simultaneously at seven energies in this range. Differential cross sections at six energies and analyzing powers at three energies are also presented for the reaction ^{4}He (p,d) ^{3}He in this region. These data will be compared to the elastic scattering of protons from both ^{4}He and ^{3}He.

The results of these measurements are presented in the remainder of the thesis. The experimental apparatus is described in Chapter II. The experimental data obtained are presented in Chapter III. Chapter IV discusses some theoretical interpretations applicable to these data. The conclusions of the experiment are summarized in Chapter V.

CHAPTER II

EXPERIMENTAL APPARATUS

2.1 Choice of Method

Most experiments in nuclear physics at intermediate energies can be performed in a variety of ways, with each method having particular advantages and disadvantages. In planning an experiment, each choice of method must be carefully weighed. It was decided to perform this experiment using a liquid helium-4 cryogenic target, and detector telescopes consisting of a multiwire proportional counter (MWPC), a plastic scintillator, and a NaI (Tl) detector.

The cryogenic target was necessary, because the very low cross sections (100-1000 nb/sr) in the region dictated as dense a target as possible to provide reasonable counting rates in the detectors. A gaseous helium target would have been less complicated to design and to operate, but could not have provided the necessary target thickness without being unreasonably long (0.5 cm of liquid helium-4 is equivalent to 3.5 metres of gaseous helium at STP).

Since the first excited state of helium-4 is 20 MeV above the ground state (Fi-73), high resolution is not required of the detectors. Thus, detector telescopes including a cylindrical NaI (Tl) detector (12.5 cm in diameter by 7.5 cm thick) with an overall resolution of approximately 1% (St-75) were chosen for the experiment. These telescopes had the advantage over a magnetic spectrometer (the

other common detector system used for these types of experiment) that they made it mechanically (and economically) feasible to mount identical detector systems on either side of the beam, reducing the problems due to false asymmetries, and the time involved in collecting reasonable data. This is especially important in considering analyzing power data.

The MWPC's were used to determine the position of particles (both the scattering angle and vertical coordinate) as they entered the detector telescopes. The MWPC's add an important degree of freedom to later analysis of the data (see Section 2.6), since the fact that a particle passed through any given area of these counters could, at that time, be made a requirement for further analysis, in addition to the on-line, event-defining logic. In this regard, MWPC's have the advantages that they are much less massive than collimators would need to be for the particle energies involved, and have none of the edge scattering problems that collimators have.

The back telescopes, measuring the angle and energy of the scattered protons, kinematically determined the reaction, but additional telescopes with a MWPC and a passing counter detected alpha particles in the forward direction. Protons scattered from ^{4}He between $\Theta_{LAB} = 144^0$ and 168^0 have associated recoil alpha particles between 13^0 and 4^0, as can be seen in Figure 1. The proton and alpha particle energies in these angular ranges are shown in Figure 2. The proton-alpha coincidence requirement provided redundant kinematic information that was extremely beneficial in minimizing backgrounds in the experiment.

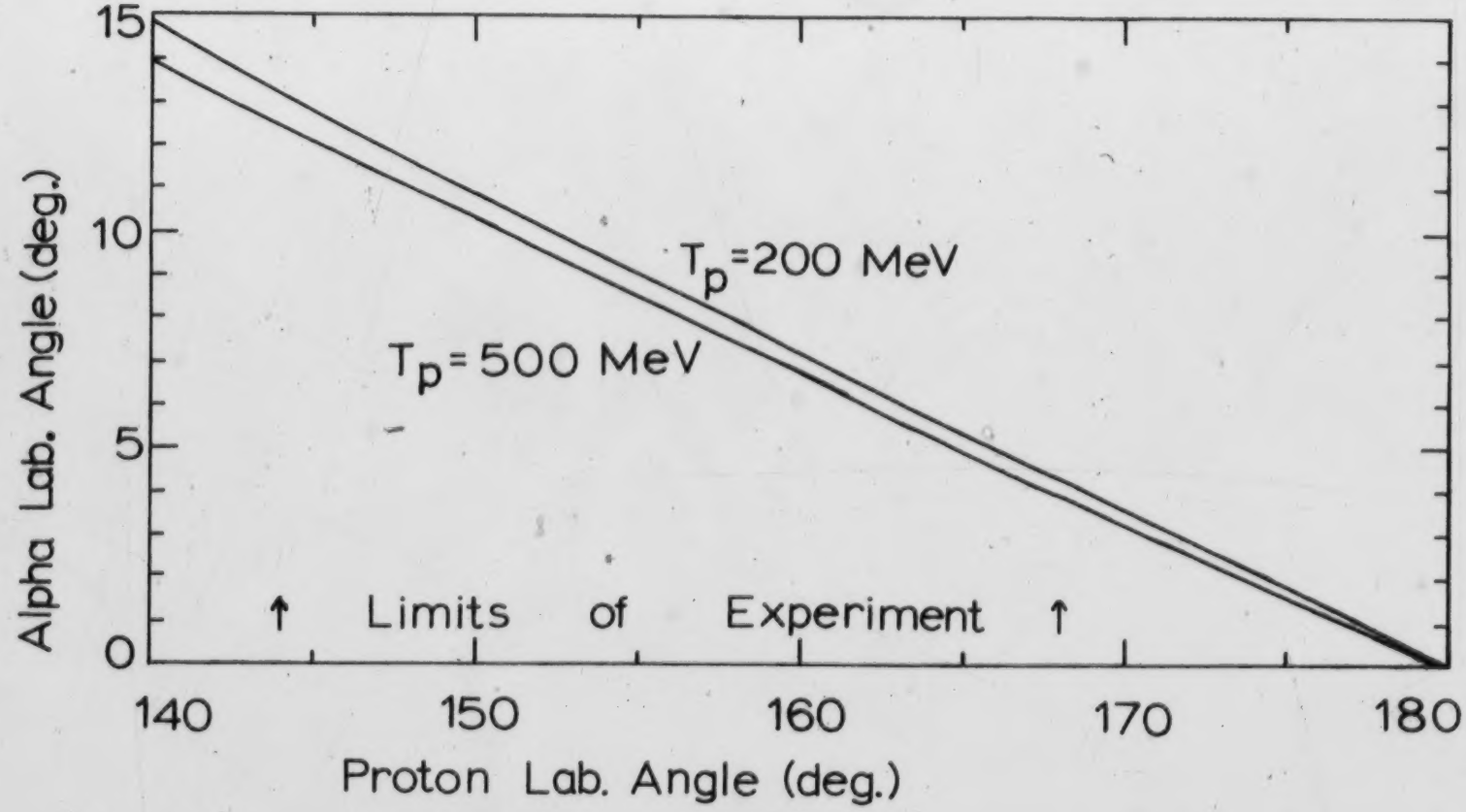

FIGURE 1. A plot of the kinematics for the reaction p + ^{4}He → p + ^{4}He in the region of interest, showing the correlation between the ^{4}He lab. angle and the proton lab. angle.

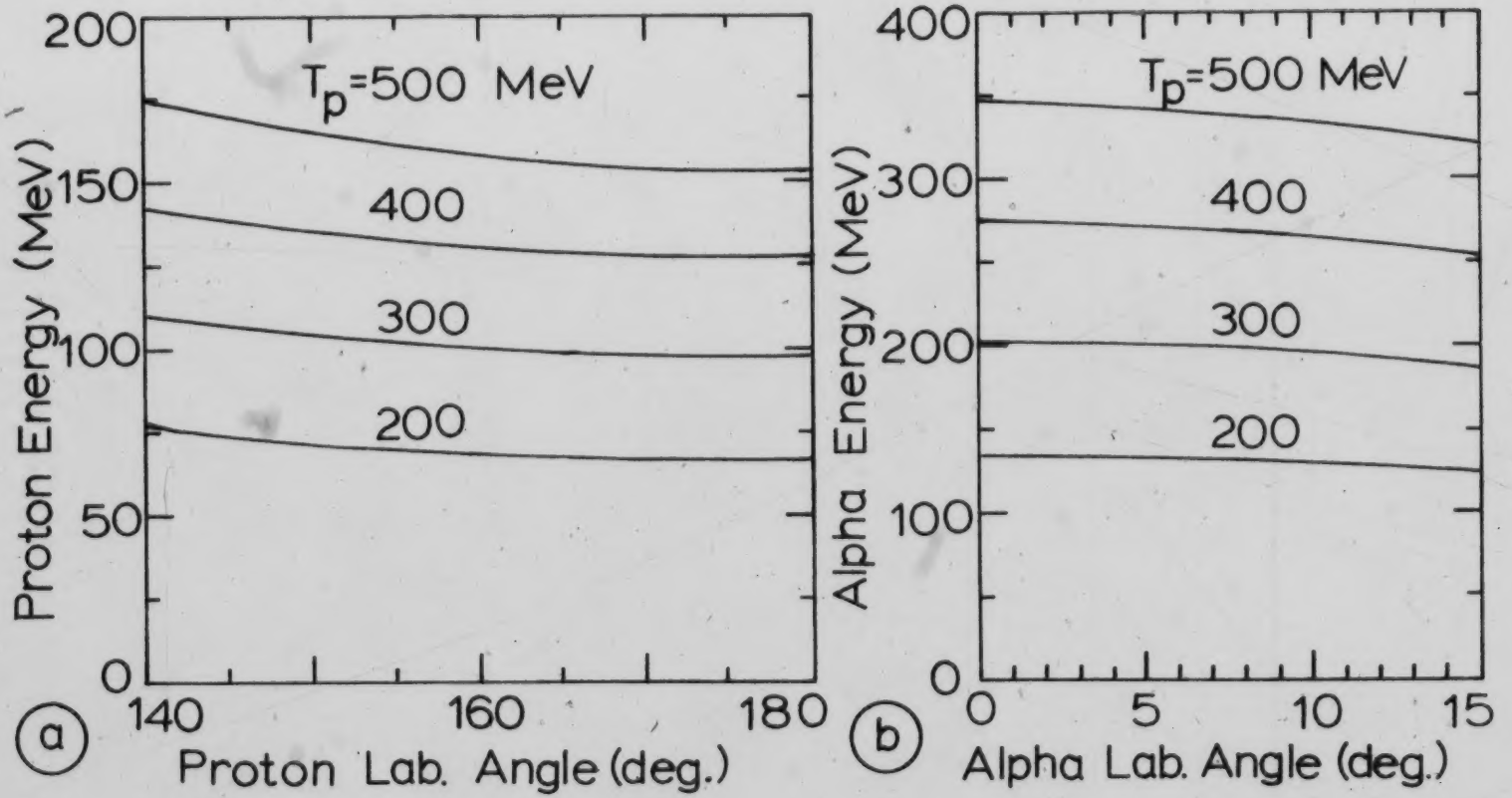

FIGURE 2. Kinematics for the reaction p + ^{4}He → p + ^{4}He: (a) proton energy vs. proton lab. angle and (b) ^{4}He energy vs. ^{4}He lab. angle.

2.2 The Accelerator and the Beam Line

The experiment was performed on the external proton beam line 4B of the 525 MeV TRIUMF cyclotron, a joint project of the Government of Canada, the University of Alberta, the University of British Columbia, Simon Fraser University, and the University of Victoria. TRIUMF is a sector-focussed H^- cyclotron which has been described in the literature (for example, Ri-65, Vo-66, Wa-70, Wa-71, Ri-73, and Ri-75).

Two ion sources were available when the experiment was performed, an unpolarized H^- source (primarily used during high current ($\geq$ 1.0 μA) operation for meson production) and a polarized H^- source of the Lamb-shift type (which produced low beam currents ($\leq$ 20 nA), primarily for nucleon-induced experiments). The polarized source (Ro-72, Ro-75) produced either positive polarization (spin up), negative polarization (spin down) or zero polarization; this polarization could be remotely selected, either from the main cyclotron control room or from the experimental station. The polarized source produced up to 80% polarization during the experiment, with normal operation near 70%. Both sources were used for the experiment, with typical beam currents on target of approximately 3-5 nA, although occasionally higher or lower currents were used.

Beam line 4B is shown schematically in Figure 3. EXT4 (an abbreviation for extraction probe, beam line 4) is a device which strips the H^- ions to H^+ ions. These ions then curve in the opposite direction in the main magnetic field and come out of the cyclotron, providing nearly 100% extraction efficiency. This probe, or stripper,

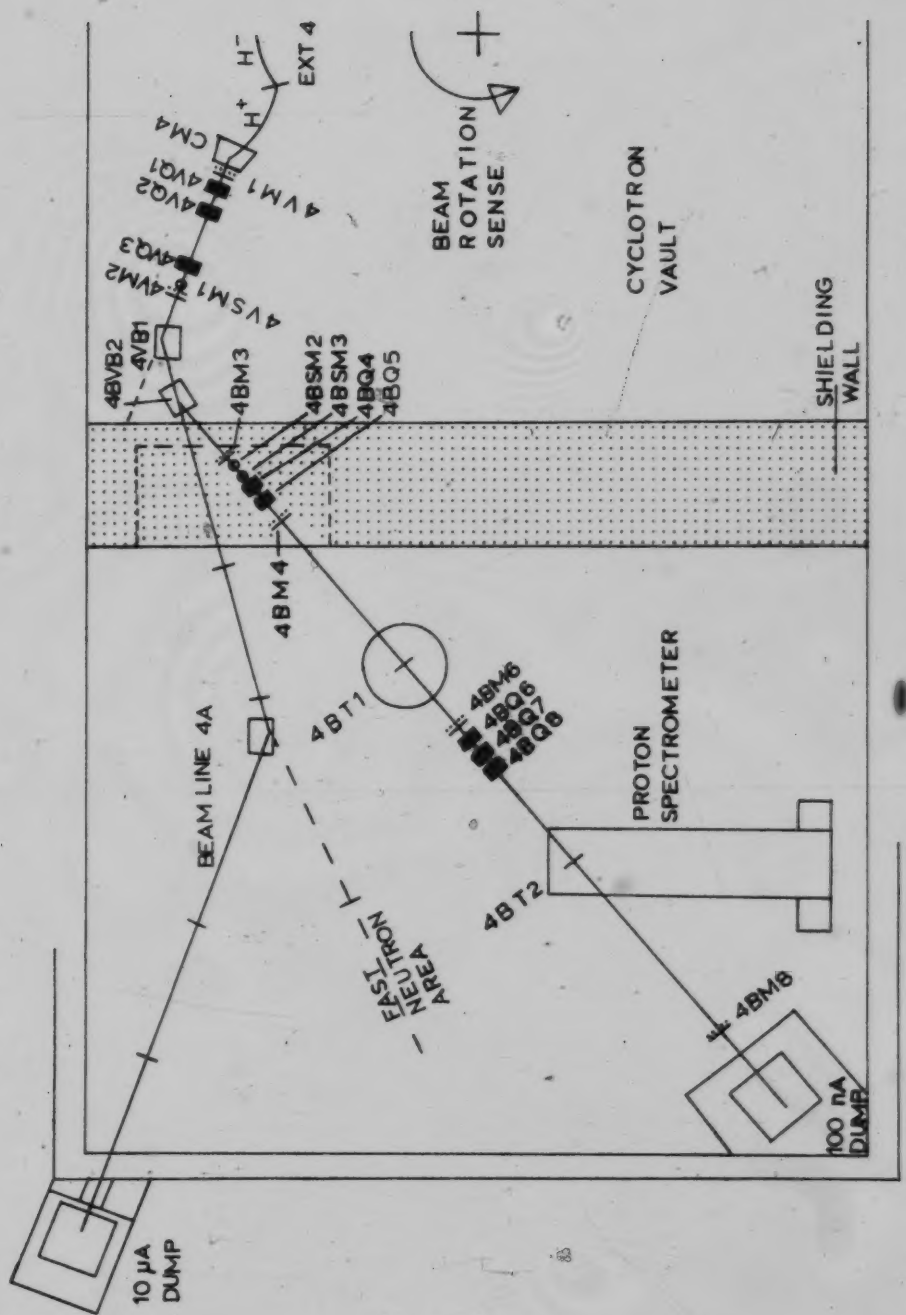

FIGURE 3. A schematic diagram of the beam line 4B beam transport system.

is a thin foil or wire of various shapes and materials (eg. carbon or aluminum), depending on operating conditions defined by the desired intensity and the beam properties requested by the other cyclotron users working in the meson production area. The stripper can be moved to select any energy between 185 MeV and 525 MeV. The stripper position and the value of the cyclotron magnetic field enable beam energies to be determined to within ± 1 MeV. CM4 is a combination magnet, collecting the H^+ beam and bending it into the beam line. Quadrupoles 4VQ1 (beam line 4, vault section, quadrupole number 1), 4VQ2 and 4VQ3 and a small steering magnet 4VSM1 (providing steering in the vertical direction) position the beam at the entrance to the bending magnets. If the bending magnet 4BVB2 is off, the first bending magnet 4VB1 directs the beam along beam line 4A. If 4BVB2 is on, the beam is directed along beam line 4B. Quadrupoles 4BQ4 and 4BQ5 and steering magnets 4BSM2 and 4BSM3 focus and position the beam at 4BT1, the target position used for the present experiment. Quadrupoles 4BQ6, 4BQ7 and 4BQ8 collect the beam after the target and focus it into the beam dump.

The elements labelled 4VM1, 4VM2, 4BM3, 4BM4, 4BM6 and 4BM8 are beam profile monitors, normally wire chambers or 'harps', which present a wire-by-wire profile of the beam in two dimensions to the control room. This information is used to tune the beam line to a particular energy or to monitor the beam profile after the target (4BM6) to ensure that the beam does not drift off center or defocus with time. In addition, a scintillator screen mounted at the target position 4BT1, viewed by a closed circuit TV monitor, is also used

for beam tuning purposes. During the experiment, the beam spot at 4BT1 was normally approximately 1 cm in diameter, with occasional beams, especially at lower energies, up to 2 cm in diameter.

2.3 The Liquid ^{4}He Target

2.3.1 The Cryogenics of the Target

As has been discussed in Section 2.1, the experiment was performed using a liquid helium-4 cryogenic target. The cryogenic features of the target are shown in Figure 4. The target was designed with vapour-cooled thermal radiation shields, similar to an Orsay liquid helium target (Bu-70). Two concentric thermal radiation shields, 'f' and 'g', surround the main helium reservoir 'h' to prevent direct heat transfer from the 300^{0}K outer vessel to the 4.2^{0}K helium reservoir. The shields are cooled by cold helium boiloff gas from the main reservoir, which passes through 0.3 cm i.d. copper tubing soldered in helical fashion to the shields. Thinwall stainless steel tubing links are used to isolate the three main components thermally, with couplings 'd' utilizing replaceable aluminum gaskets to allow for disassembly. Three nylon bolts, 'o', 120^0 apart serve to keep each shield concentric with the reservoir or the inner shield, to prevent contact between these components. (Nylon is used because it has low thermal conductivity and because it does not become brittle at cryogenic temperatures.) Any direct contact would destroy the thermal isolation and cause the liquid helium to vapourize. A cylindrical copper extension 'p' to the outer shield surrounds the sample cell region.

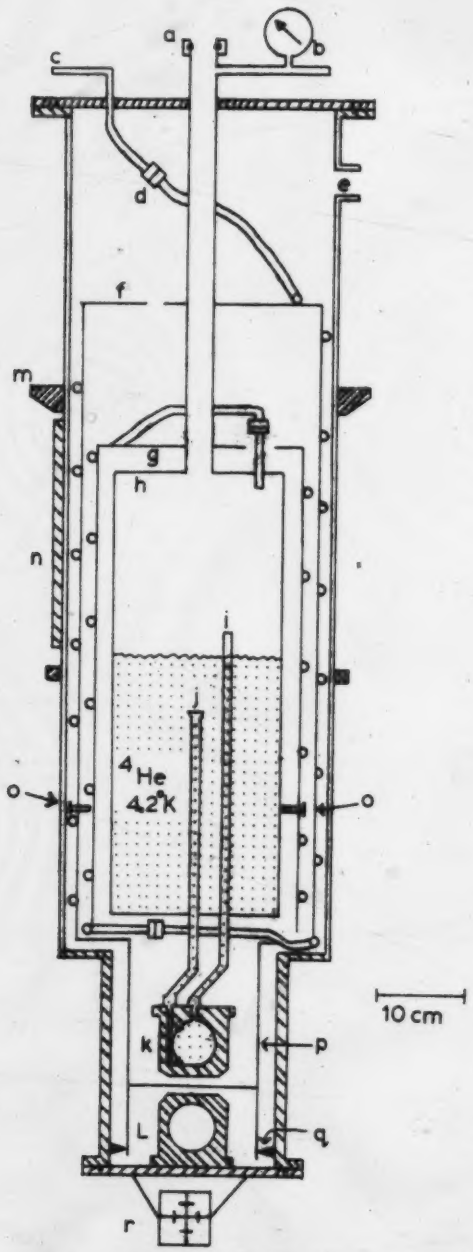

FIGURE 4. The helium target cryogenic details, with (a) fill inlet,(b) interior pressure gauge,(c) gas boiloff line,(d) mechanical coupling,(e) vacuum system connection,(f) outer and (g) inner radiation shields,(h) main liquid ^{4}He vessel,(i) cell boiloff standpipe,(j) fill tube receptacle,(k) target cell,(l) dummy cell,(m) vertical position stop ring,(n) rotation sprocket key, (o) spacer bolts (1 of 3 shown),(p) radiation shield extension, (q) bottom spacers, and(r) scintillation screen. The scale is only approximate, especially for small dimensions.

Another spacer 'q' keeps this extension and the outer thermal shield concentric with the outer vessel.

The reservoir, the exterior surfaces of the two radiation shields and the feed and boiloff tubes to the target cell are all insulated with eight to ten layers of crinkled, aluminized mylar (superinsulation) alternated with layers of nylon mesh to thermally separate each layer of aluminized mylar. In addition, the bottom extension piece is wrapped with one layer of superinsulation so that heat cannot pass directly to the sample cell from the outside. With this insulation, the reservoir (15 litre capacity) suffices to keep the cell full for up to 36 hours.

Another feature of the target was the ability to change target cells with reasonable ease to accomodate different experimental requirements. Target cells, shown in Figure 5, consist of brass or stainless steel bodies with 5.0 cm square apertures, and with thicknesses of 0.5 to 2.0 cm. The target cell used for the present experiment was 0.5 cm thick (nominally) and was constructed of brass. A brass cell was used because it was much easier to attach windows to it. These windows (25 μm nickel foil) were soldered directly onto the cell bodies. Thin plates were bolted onto the body on top of the nickel windows to prevent the foil from peeling off under the one atmosphere (or more) pressure that is exerted outward from the target cell during operation.

Originally, the cells were attached to the main body of the cryostat with a coupling using indium seals. A groove, 1 mm wide and 1 mm deep was machined around the feed and boiloff apertures on

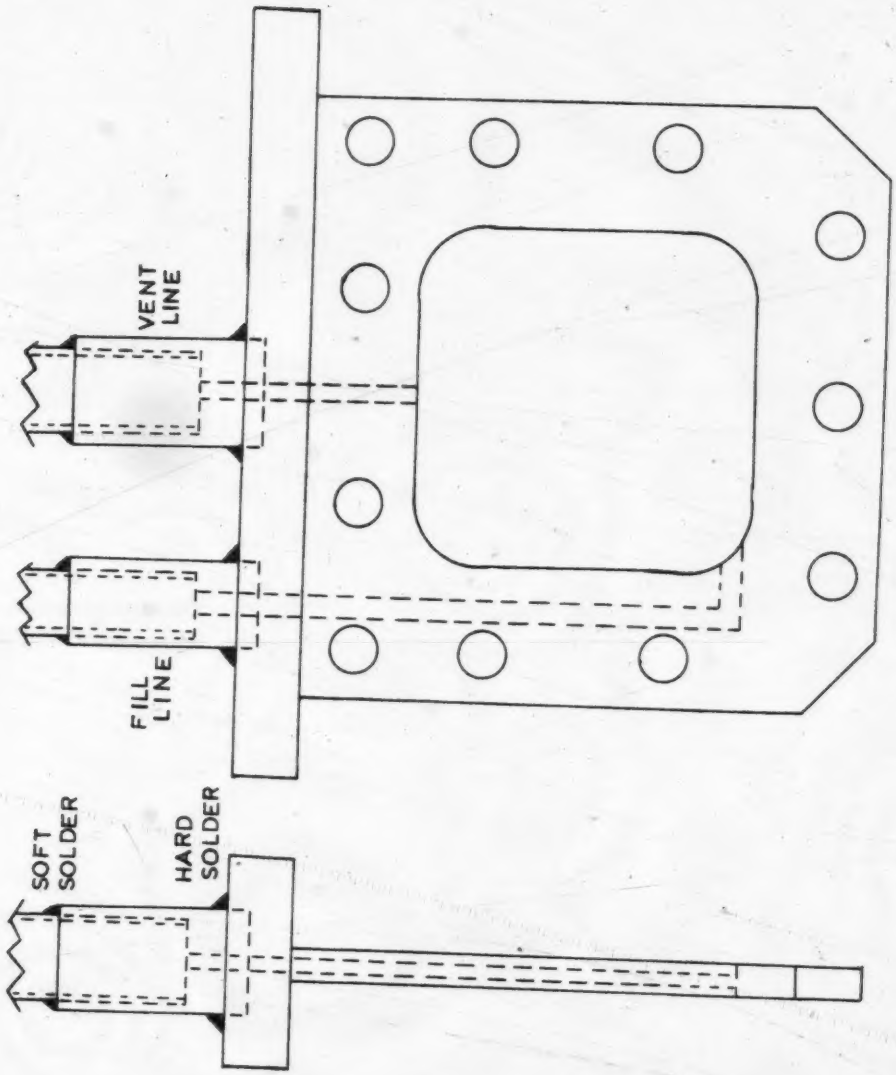

FIGURE 5. The ^{4}He target cell, showing the method of attaching the cell to the tubes from the main liquid reservoir.

the top of the cell body. These grooves were carefully filled with indium wire and the cell body was bolted onto a stainless steel block at the end of the tubes coming down from the reservoir. This block had two matching projections on it and when the two parts were bolted tightly together, the indium wire was expected to flow, making a leak-tight seal around the two apertures. However, difficulties were experienced due to the repeated failure of these seals under thermal cycling, so a more straightforward coupling method was adopted. Two stubs were hard-soldered onto the top of the sample cell (see Figure 5), and the block on the feed and boiloff tubes was removed. Then the stubs on the sample cell were passed over the ends of the tubes and soft-soldered into place. Although some care had to be taken during this soldering due to the abundance of extremely flammable superinsulation in the immediate vicinity, this method of attaching the target cells has proved to be very reliable, even after repeated thermal cycling.

As can be seen in Figure 4, the target cell is gravity filled, with liquid helium entering the cell from the bottom. The helium gas boiloff emerges from a top hole in the cell through a 25 cm high standpipe 'i' inside the reservoir, in order to minimize the accumulation of gas in the target region.

The insulating vacuum space is pumped with a standard 5.0 cm diameter oil diffusion pump, backed by a mechanical pump which is also used to pump out the vacuum space to a rough vacuum. The valves in the vacuum system are pneumatic and are controlled by a protective interlock system, utilizing thermocouple vacuum gauges with setpoints

connected to the interlock circuitry. Should the cryostat pressure or the pressure in the diffusion pump rise past these setpoints, valves are automatically closed and the diffusion pump heater is turned off to prevent damage to any part of the system. A high vacuum ionization gauge is monitored continuously from the remote controls location, as are valve positions and the reservoir level (this latter capability was not utilized during the present experiment). Typical pressures in the vacuum vessel were 3×10^{-3} Pa at room temperature, $6\text{-}10\times10^{-4}$ Pa with LN_2 in the reservoir during the precooling period, and $1\text{-}4\times10^{-4}$ Pa with liquid helium. (The many layers of superinsulation inside the cryostat trap air and act as virtual leaks, making the room temperature pressure higher than might be expected.)

A typical start-up sequence began by pumping the cryostat to a high vacuum for at least eight hours, and preferably twenty-four hours. Then the helium reservoir was filled with liquid nitrogen. This precooling stage allowed the radiation shields to be cooled by the N_2 boiloff gas and lasted another eight to twenty-four hours. Then the liquid nitrogen was blown out and a small resistive heater heated the target cell to about $90^{\circ}K$ to ensure that the liquid nitrogen was exhausted before the liquid helium transfer was initiated. The liquid helium transfer tube was inserted into the feed line 'j' in the reservoir and a sufficiently high pressure ($\approx$ 13 kPa) was maintained in the helium container to ensure an adequate flow of cold gas through the target cell and then through the relatively long radiation shield tubing. When optimized, the initial transfer rate

was 3-4 litres of liquid helium per hour and approximately 2½ hours were required to initiate liquid formation in the target vessel. During initial tests, diode sensors were installed on the target cell and on the inner and outer radiation shields, in order to monitor the cooling rates. The shields reached ultimate low temperatures of 20°K and 80°K, respectively. Approximately 30 litres of liquid helium were required for the initial filling. The target was refilled routinely every 24 hours, with a refill typically requiring one half hour. The helium lifetime was so constant during the experiment that it was not necessary to use the reservoir level sensing apparatus.

2.3.2 The Target Positioning Mechanism

A necessary addition to the target is an empty target cell that can be quickly inserted into the beam to determine contributions, if any, from the cell body and the windows. The target assembly therefore includes a 'dummy' cell and a scintillator screen for beam focussing and alignment ('l' and 'r', Figure 4, respectively), as was discussed in Section 2.2. A remote controlled target elevator is used to position the assembly at any one of the three positions. In addition, some experimental detector configurations, eg. detecting scattered particles near 90°, require that the target be rotated about a vertical axis. The target elevation and rotation system accomplishes both of these motions while maintaining the beam line vacuum integrity. Figure 6 shows these systems, with the target in

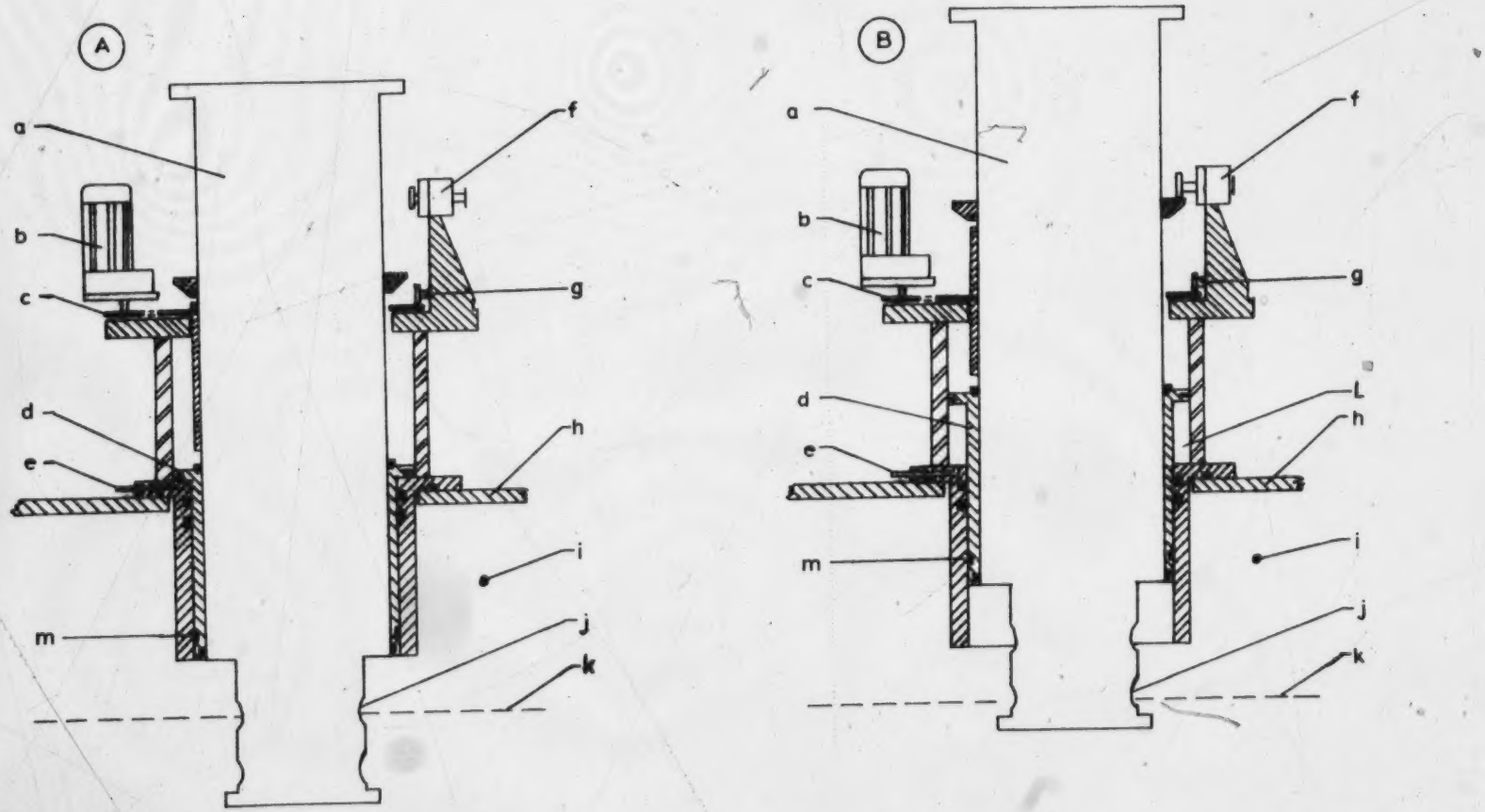

FIGURE 6. The target rotation and elevation mechanism, showing (A) the low position, and (B) the middle position. Details include (a) the main cryostat, (b) rotation motor, (c) chain and sprocket drive, (d) pneumatic cylinder, (e) compressed air inlet, (f) stop defining middle position, (g) sprocket retention bearing, (h) scattering chamber, (i) beam line vacuum, (j) Kapton windows, (k) beam plane, (l) elevation expansion volume, and (m) added O-ring seal.

the lowest position (Figure 6 (A)), which is the real target position, and in the middle position (Figure 6 (B)), the dummy target position. The elevation system is pneumatic, with the cryostat mounted inside a brass cylinder 'd' that serves as a pneumatic plunger. Lifting is accomplished by opening a solenoid valve to a compressed air line 'e'. The air, entering the expansion space 'l' provides the lifting force against the large atmospheric loading. Lowering is accomplished by opening a venting solenoid valve. Microswitches sense that the assembly has reached the desired position and close the appropriate valve as well as sending a confirming signal to the control panels. To reach the middle position (the dummy cell), three equally spaced plungers 'f' are activated and act as stops against which the cryostat stops. Therefore, the middle position must be reached from below (the full target) and the cryostat may not go from the middle to the high position without being lowered first to allow the plungers to retract. Rotation is accomplished via an electric motor 'b' with a chain drive 'c' and a direct potentiometer angle readout. (The target rotation capability was not needed for the present experiment.)

A set of four O-rings, one above the expansion space 'l', two immediately below the space and one further O-ring at the base of the brass cylinder 'd', serves as a combination sliding-rotating seal. This last O-ring 'm' had to be added when it was determined that the brass cylinder, which was a casting, was porous, allowing air to seep past the upper two O-rings and enter the vacuum space 'i' below. This added O-ring corrected the deficiency to the point

where tests showed that the lifting operation had a minimal effect on the rough beam line vacuum.

2.4 The Scattering Chambers and the Detectors

2.4.1 The Scattering Chamber

The general features of the beam line were presented previously (Section 2.2). In this section, the apparatus directly associated with the experiment will be discussed. This apparatus is shown in Figure 7. The scattering chamber used for the experiment was a rectangular box, measuring approximately 80 cm long by 60 cm wide with an extension piece, the 'horn', attached downstream from the target. This horn, 185 cm long and 142 cm wide at the large end, permitted the detection of scattered particles in the angular region from 3^0 to 15^0. Also, since the scattering box and the horn were maintained at a rough vacuum, multiple scattering effects of a long flight path were minimized. The upstream end of the scattering box had a flange on it, enabling scattered protons to emerge through thin windows over the angular range from 141^0 to 172^0. In addition, the sides of the box had apertures enabling particles to emerge through thin windows between 35^0 and 105^0.

The windows on the upstream side of the box consisted of 130 μm Kapton-H foil,* while the side windows were of 250 μm Kapton

---

*Kapton-H Polyimide Foil, E. I. du Pont de Nemours and Co. Inc., Circleville, Ohio 43113.

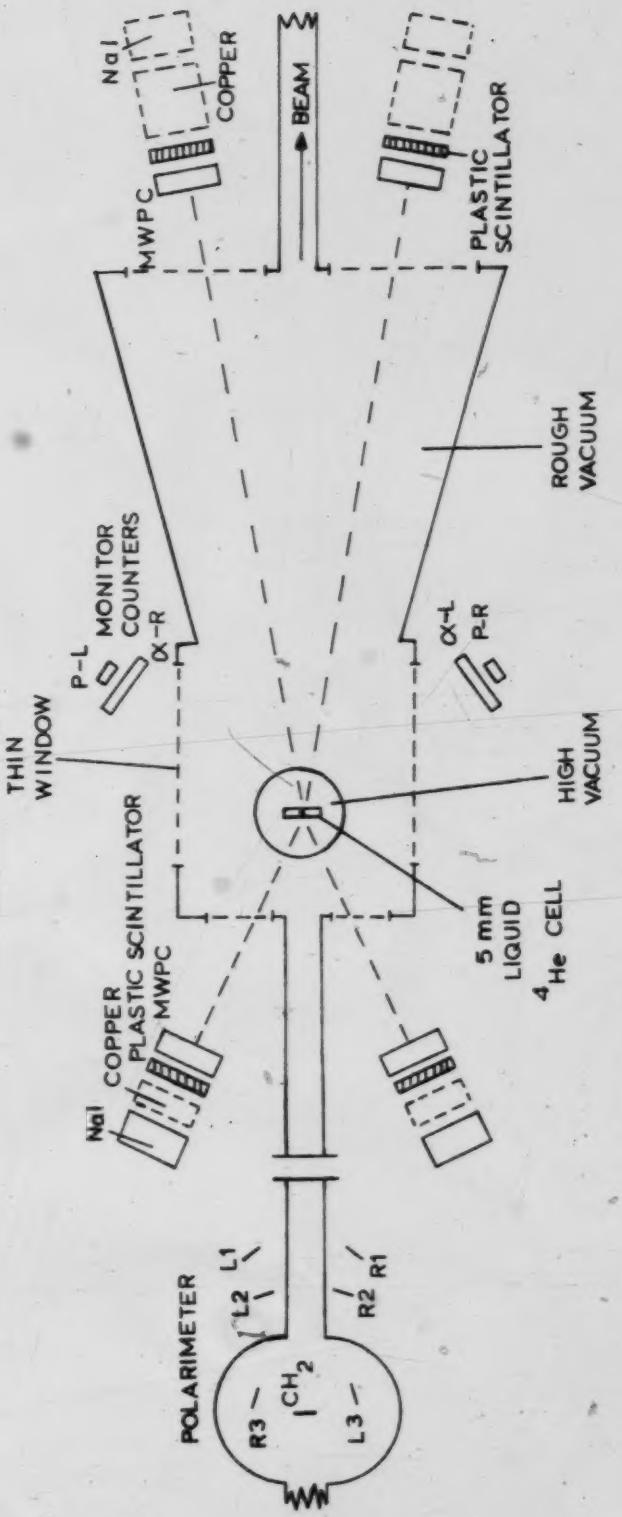

FIGURE 7. A schematic diagram of the scattering chamber and the experimental apparatus.

foil, as were the windows on the horn. Also at the exit of the horn, thin sheets of aluminum, from 0.079 cm to 0.318 cm, depending upon the beam energy, served to prevent low energy electrons from entering the detectors. In addition, the helium target had 80 μm of Kapton around the target cell to separate the (good) target vacuum from the (rough) scattering box vacuum. A thin metal foil (7.5 μm aluminum) was placed in the beam line at the entrance to the experimental area to separate the main machine vacuum system from the experimental vacuum system.

2.4.2 The Polarimeter

About 250 cm upstream from the helium target location, a polarimeter was located to monitor the beam polarization during the experiment. Elastic proton-proton scattering was chosen as the calibrating reaction because of its relatively flat cross section and because the angle at which its analyzing power is maximum changes slowly with the beam energy. The polarimeter target was a 5 mg/cm^2 CH_2 foil; p-p scattering was measured at a laboratory angle of 17^0. Two detectors on each side of the beam (see Figure 7) formed a telescope which detected scattered protons at forward angles while other detectors, located inside the vacuum chamber, detected the corresponding recoil protons. Detectors L1 and R1 (see Figure 7) determined the solid angle acceptance of the system. These detectors were oriented to have a solid angle independent of beam position at the target. This was done by rotating L1 and R1 so that they pointed

to a position downstream from the polarimeter target. With this configuration, if the beam moved so that the scattering angle to L1 was larger (smaller cross section), then the effective solid angle defined by L1 would increase so that the count rate would be approximately independent of the move. Lead shielding was placed around the polarimeter to reduce backgrounds from the polarimeter and the beam line foil in the primary detectors.

Coincidences L1·L2·L3 and R1·R2·R3 were counted, as were accidental coincidences between the same detectors with one signal (L3 or R3) being delayed by 43 nsec, the time between consecutive beam pulses from the cyclotron. Typically, accidental coincidences were less than 1% of real coincidences, with occasional runs having accidental rates up to 2%. A remote controlled polarimeter target changer was used to change to a carbon foil, so that contributions to the measured polarimeter asymmetries from C (p, 2p) could be measured under identical beam conditions. The corrections to the measured polarimeter asymmetry due to carbon are given as a function of beam energy in Figure 8.

2.4.3 The Principal Detectors

The principal detectors for the experiment were mounted on four detector support arms or 'booms'. These booms, which were remotely movable, were denoted by FL (front (i.e. downstream), left), BR (back, right), FR and BL, as were the detectors mounted on each boom. The four booms and the positions of the MWPC's and the other

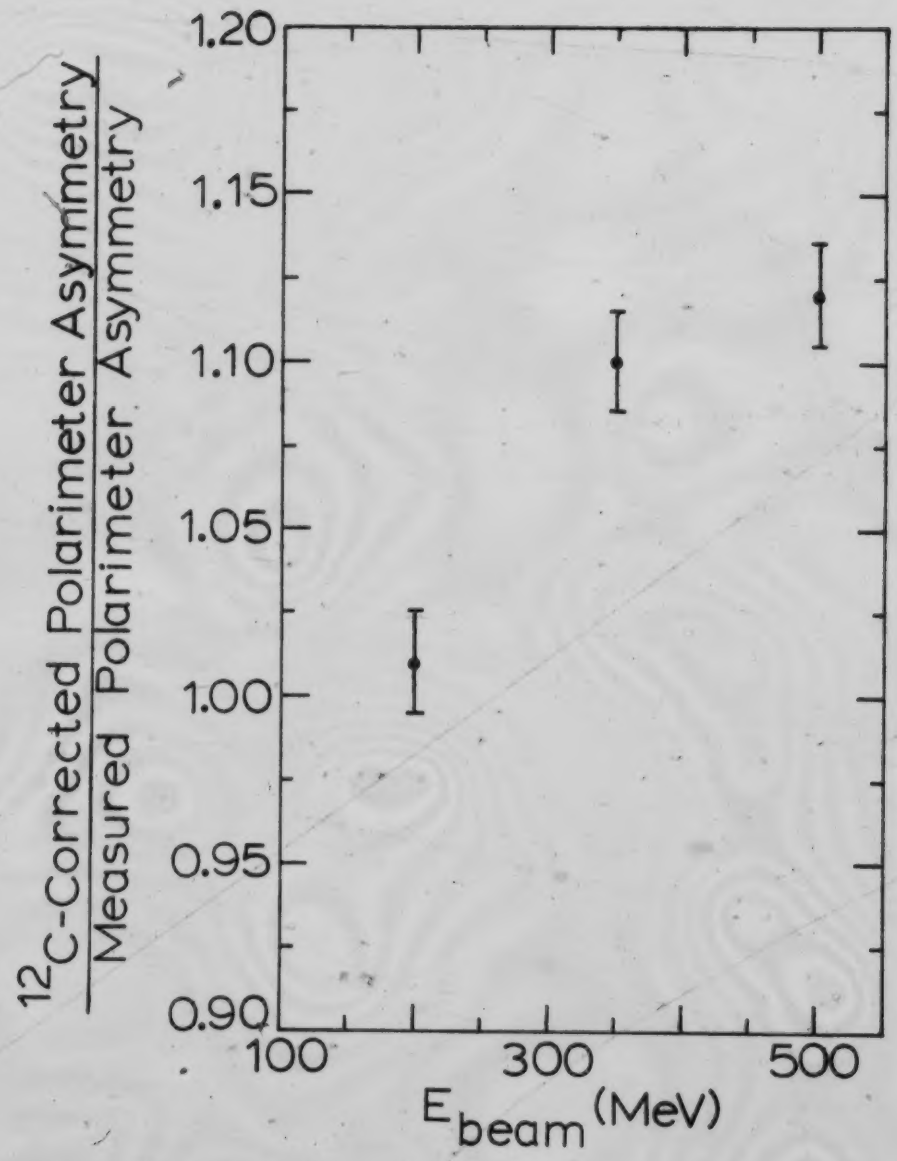

FIGURE 8. The correction to the measured polarimeter asymmetry due to the carbon contribution as a function of beam energy.

counters on the booms are shown in Figure 9. The booms are 20^0 wide in order to accommodate a variety of detector configurations and for greater stability. In order to allow the detectors to cover the required angular ranges, the detectors were mounted at the edges of the booms, as is shown in Figure 9. The detectors on the front booms were mounted 7^0 toward smaller angles, while detectors on back booms were mounted 6^0 towards larger angles. These offsets were determined to an accuracy of $\pm 0.05^0$. The centers of the forward detectors were able to see scattering angles as small as 4^0, and the centers of the backward detectors could observe particles scattered up to 168^0. The limits in both cases occured when detector mounting frames encountered the beam pipe or its supports.

The boom angles were determined to an accuracy of 0.1^0 by a system of fine slots, one degree apart, machined into a large ring. A photosensitive cell looking through the slots at a light-emitting diode emitted a signal when the boom was centered on one of the slots. Larger, binary-coded holes drilled in the ring and read in an identical manner indicated the angular setting where the boom was located.

The detectors on each boom were arranged into a detector telescope. Each telescope (St-75) consisted of a MWPC, a thin plastic scintillator and a 12.5 cm diameter by 7.5 cm thick NaI(Tl) crystal mounted on a 12.5 cm diameter photomultiplier tube.

The MWPC's had both X and Y sense planes (scattering angle and vertical distance, respectively) with 2 mm wire spacings. The

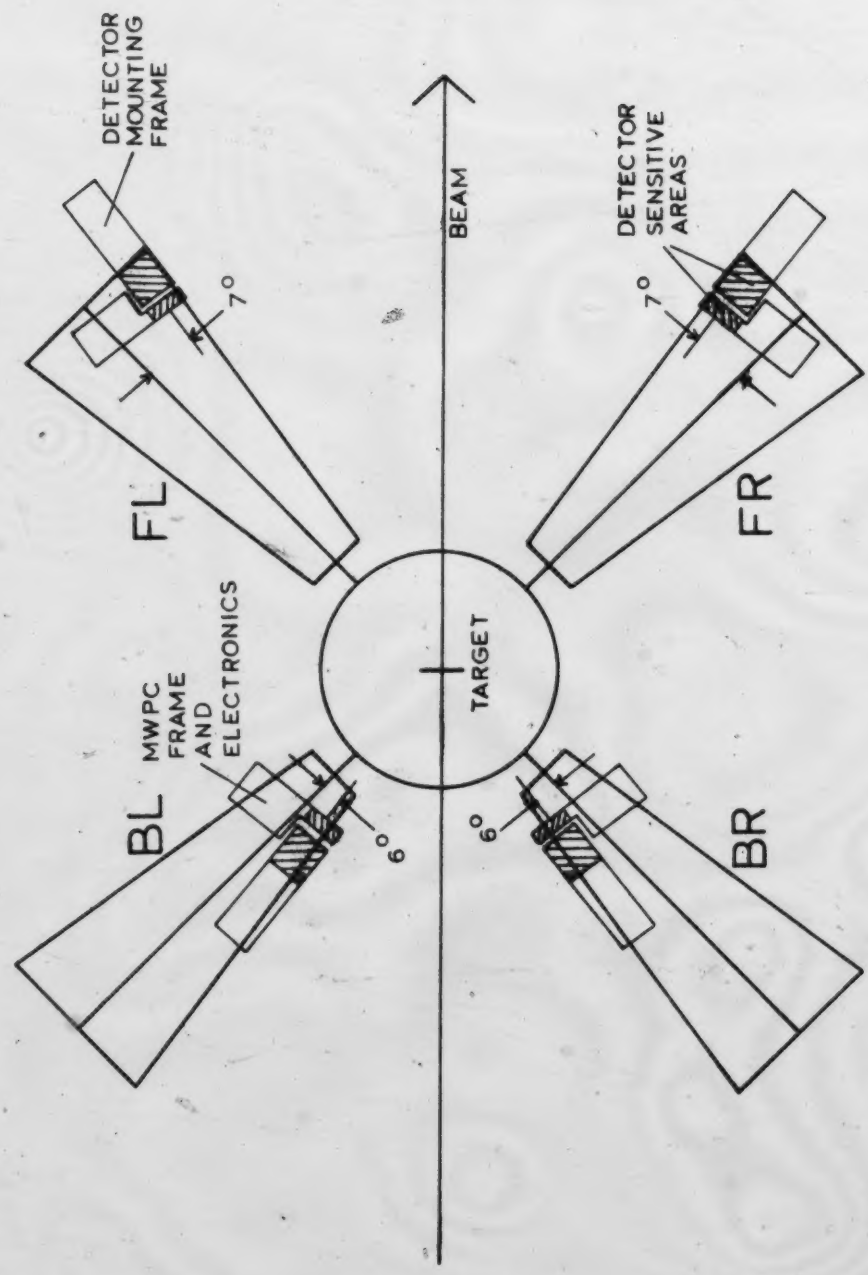

FIGURE 9. The positions of the MWPC's and the other detectors upon the four booms.

back MWPC's were 64 wires by 64 wires, while the front MWPC's were 128 wires vertically by 64 wires horizontally. However, the plastic scintillators in the front telescopes limited the effective size of these detectors to the central 64 wires by 64 wires. The MWPC's consisted of a plane of high voltage wires (normally held at -5 kV), one sense plane, a HV plane, the other sense plane, and another HV plane. A special, 'magic' gas mixture (75% Ar bubbled through methylal ($CH_2(OCH_3)_2$) at 0^0 C, 24.5% isobutane (C_4H_{10}), and 0.5% freon-13B1 ($CBrF_3$)) (Ch-72) was circulated through the chambers and was contained by 25 μm Kapton windows on the chambers. The wire chamber readout system is based on an amplifier per wire system and has been fully described by Cairns and Dawson (Ca-75). The wire chamber data was not included in the event-defining logic.

The distance from the target center to the middle HV plane (midway between the solid angle defining X and Y sense planes) of the BL wire chamber was D_{BL} = 109.5 ± 0.2 cm and, similarly, D_{BR} = 109.6 ± 0.2 cm. While the solid angles of the front and back wire chambers were nearly matched (taking into account the appropriate kinematic transformations), the front wire chambers were placed so that the back wire chambers determined the solid angles. The front wire chambers were placed at distances of D_{FL} = 267.2 ± 0.2 cm and D_{FR} = 267.4 ± 0.2 cm.

The second detector in each telescope was a thin plastic scintillator (constructed of Pilot B scintillator). These counters were used for their excellent timing properties and also to obtain

energy loss signals from particles passing through them. The plastic scintillators (3 mm thick)in the back telescopes were set to have a high gain so that protons would yield large signals. The plastic scintillators (6 mm thick) in the front telescopes were set with much lower gains and higher thresholds, so that these counters would be much less sensitive to the numerous protons at these angles, but more sensitive to alpha particles passing through them. When the front telescopes were used to detect small angle elastically scattered protons, their plastic scintillators were set at a higher gain to make them proton-sensitive.

The NaI counters were used to measure the total energy of particles. The NaI detectors, 7.5 cm thick, will stop 150 MeV protons, so protons with higher energies were degraded in energy to less than that energy by an appropriate thickness of copper. On the back booms, protons of interest stopped in the NaI detectors at all incident beam energies except 500 MeV (see Figure 2), where 1.25 cm of copper was used between the plastic scintillator and the NaI detector. On the front booms, only the MWPC and the plastic scintillator were incorporated into the back angle measurements. However, the full telescopes were used to detect 13^0 and 14^0 elastically scattered protons to determine the helium target thickness by normalizing the results to previous measurements (see Section 3.1). In those circumstances, 16.5 cm of copper were needed in the front telescopes at 500 MeV, with lesser amounts at 350 MeV and 200 MeV (9.2 cm and 2.4 cm, respectively).

Because of the large amounts of copper inserted into the telescopes, the detector efficiency was significantly affected. An extensive set of efficiency calibration measurements were performed; the details have been previously published (Ca-77). For example, the measured efficiency of the central region of the telescope is shown in Figure 10 (taken from (Ca-77)) as a function of incident proton energy. Also illustrated is a calculation (St-75) of this efficiency using reaction cross sections. The central region of the telescope is the region of the NaI crystal where edge effects do not contribute significantly. The size of this region decreases with increasing proton energy (Ca-77).

2.4.4 The Monitor Counters

In addition to the detectors mounted on the four booms, four stationary counters viewed the target to monitor variations in target thickness from run to run (see Figure 7). The design criteria for these counters were that they detect elastically scattered protons and the associated alpha particles in coincidence (for background minimization) and that the count rates be maximized. The target cell geometry was such that the maximum angle that particles could leave the cell without striking the cell body was 70^0. Thus, all counters had to be placed at smaller angles than that. In order for the alpha particles to have sufficient energy to be detectable, the alpha particle counters must be located at smaller angles than the proton detectors at low beam energy, and at

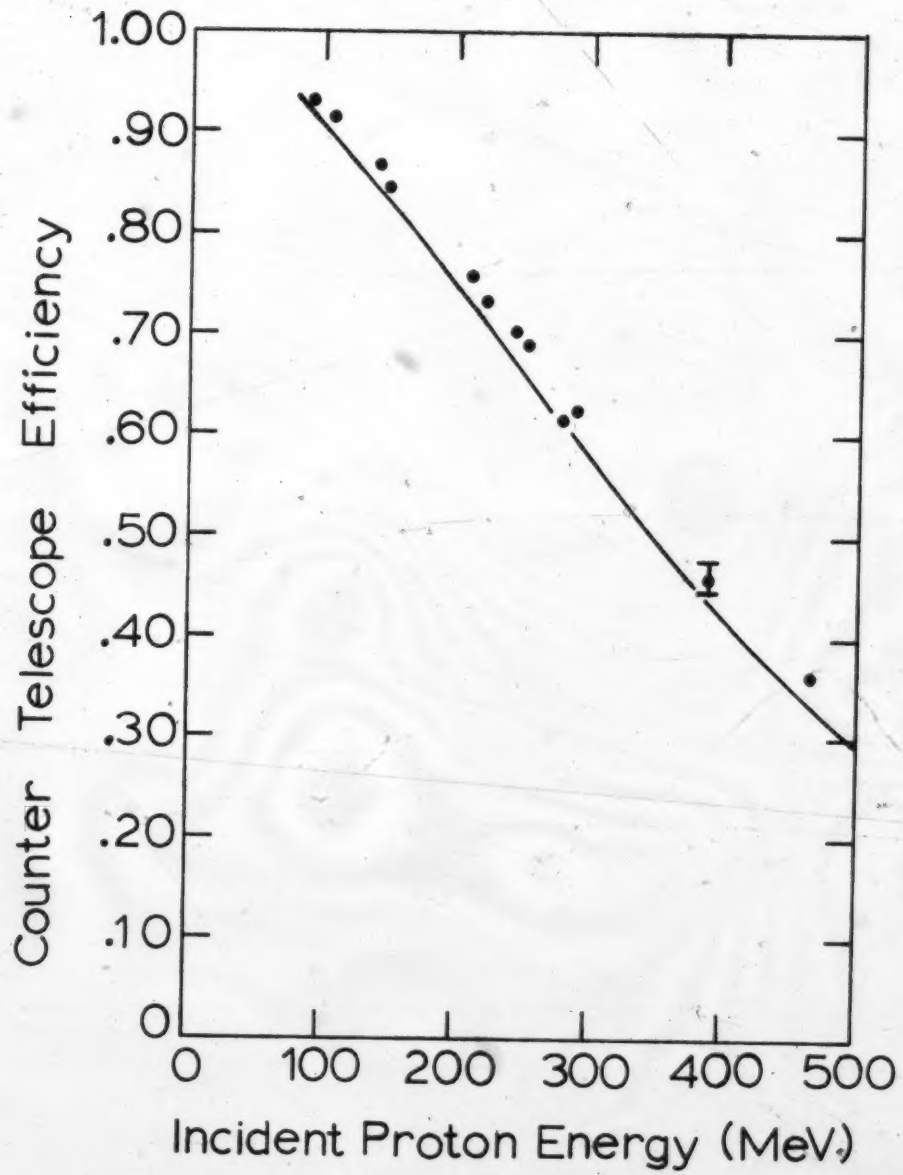

FIGURE 10. The efficiency of the central region of the telescope (as discussed in the text and (Ca-77)) as a function of incident proton energy (taken from (Ca-77)). Where not shown, the uncertainty in the measured value is less than the size of the point. The solid line is a calculation (St-75) using reaction cross sections.

the same angle or smaller angles at high beam energy. The count rate requirement could be met by detecting the protons at as small an angle as possible, since the elastic scattering cross section, the main contribution to the monitor counts falls rapidly with increasing proton angle. These requirements were somewhat contradictory, so compromises had to be reached.

Two separate configurations were used during data taking. The first configuration, $\Theta_p = \Theta_\alpha = 54^0$ was used for beam energies above 350 MeV while the second, $\Theta_p = 66.5^0$, $\Theta_\alpha = 47^0$ was necessary below 350 MeV to obtain alpha particles of detectable energy. It is worth noting that since the elastic scattering cross sections rise rapidly with lower energy, the change in proton angle did not result in lower count rates for the low energy configuration. At 200 and 185 MeV, alpha particles originating at the upstream edge of the helium cell would not have enough energy to reach the counters, but no solution could be found for this problem. Thus, at these very low energies, the monitors effectively viewed only part of the target. Identical counter configurations were used on either side of the beam, and their outputs were summed to eliminate the effects of using a polarized beam.

The proton counters were used to define the solid angle acceptance of the proton-alpha pair and were 5.0 cm wide by 2.5 cm high. They were mounted approximately 1 meter from the target and were constructed of 6 mm plastic scintillator, as were the alpha particle counters. The alpha particle detectors were designed to be

large enough to detect all of the alpha particles defined by the proton counter at all energies for which one configuration would be used. Thus the monitor counters did not have to be moved each time the beam energy was changed. The alpha particle detectors were 12.7 cm by 12.7 cm; this size also took into account the multiple scattering that the relatively low energy alpha particles would undergo. Blocks of copper absorber (1.3 cm for beam energies less than 350 MeV, 2.5 cm otherwise) were placed in front of the proton counters to stop the alpha particles so that only protons would be detected. True coincidences P-L·α-L and P-R·α-R (see Figure 7) were collected, as were random coincidences where one signal was delayed one beam burst time interval.

The number of monitor counts for an empty target run was always less than 4% of that for a full target run (appropriately normalized). The monitor counters actually monitored the product of beam current and target thickness. The ratio of monitor counts to one of the beam current monitors, i.e. the ion chambers or the total polarimeter counts (see Section 3.1), was a measure of the relative target thickness alone. The ratio of monitor counts to polarimeter counts varied at any one energy by as much as 12%. However, no correlation was seen between this variation and apparently relevant experimental parameters such as the beam current, the time elapsed since the target was last filled, etc. Moreover, similar runs with differing monitor results yielded the same differential cross sections, within the experimental uncertainties.

2.5 The Electronic System and Data Acquisition

2.5.1 The Backward Angle Electronics

The data was collected and processed by an integrated system of fast NIM logic and CAMAC electronics. Figure 11 shows, in a most general way, the configuration used for the experiment. A three-fold coincidence on either the left or right side (left or right here referring to the side which detected the proton) defined a possible elastic scattering event and initiated logical processes in the electronics and in the acquisition computer, which, as an example, would request data from the MWPC's.

The electronics system was formed in two sections. One section, shown in Figure 12, was located in the experimental hall, near the detectors, and was primarily involved with the MWPC data. The EVENT FAST signal caused any information in the wire chambers to be held, each separate wire having its own memory element. The MWPC controller then waited a preset time while the remote electronics decided if the event was valid or not. If so, a MASTER GATE signal, also called an EVENT SLOW signal, would enable the MWPC information being held to be read into the computer via a CAMAC input register. The controller would clear and reset itself upon receipt of a CLEAR signal (if no MASTER GATE signal was received within the required time limit, approximately 1 μsec, a CLEAR signal was internally generated). In the meantime, the EVENT FAST signal had latched the

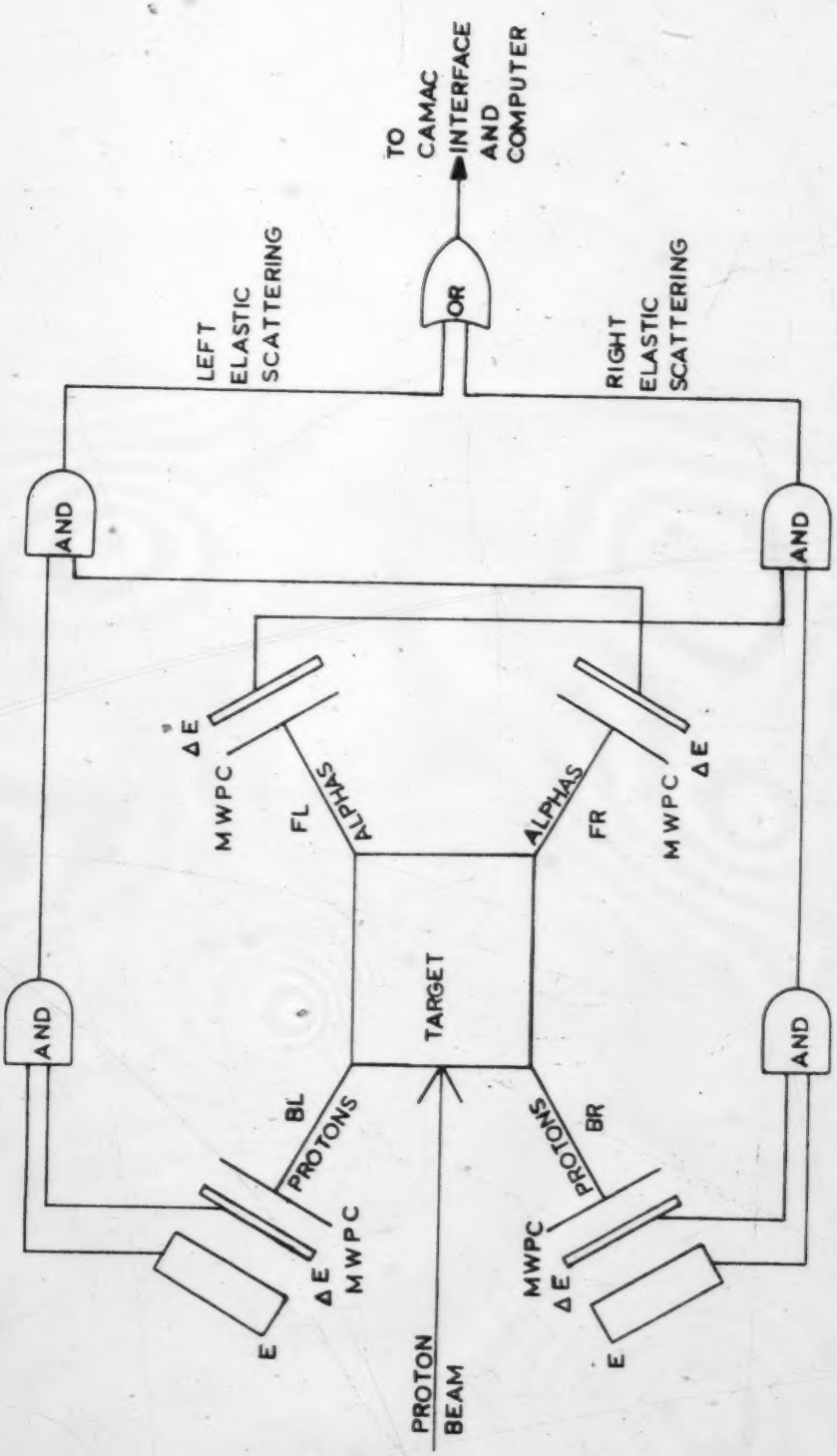

FIGURE 11. A schematic block diagram of the electronics used for the back angle measurements.

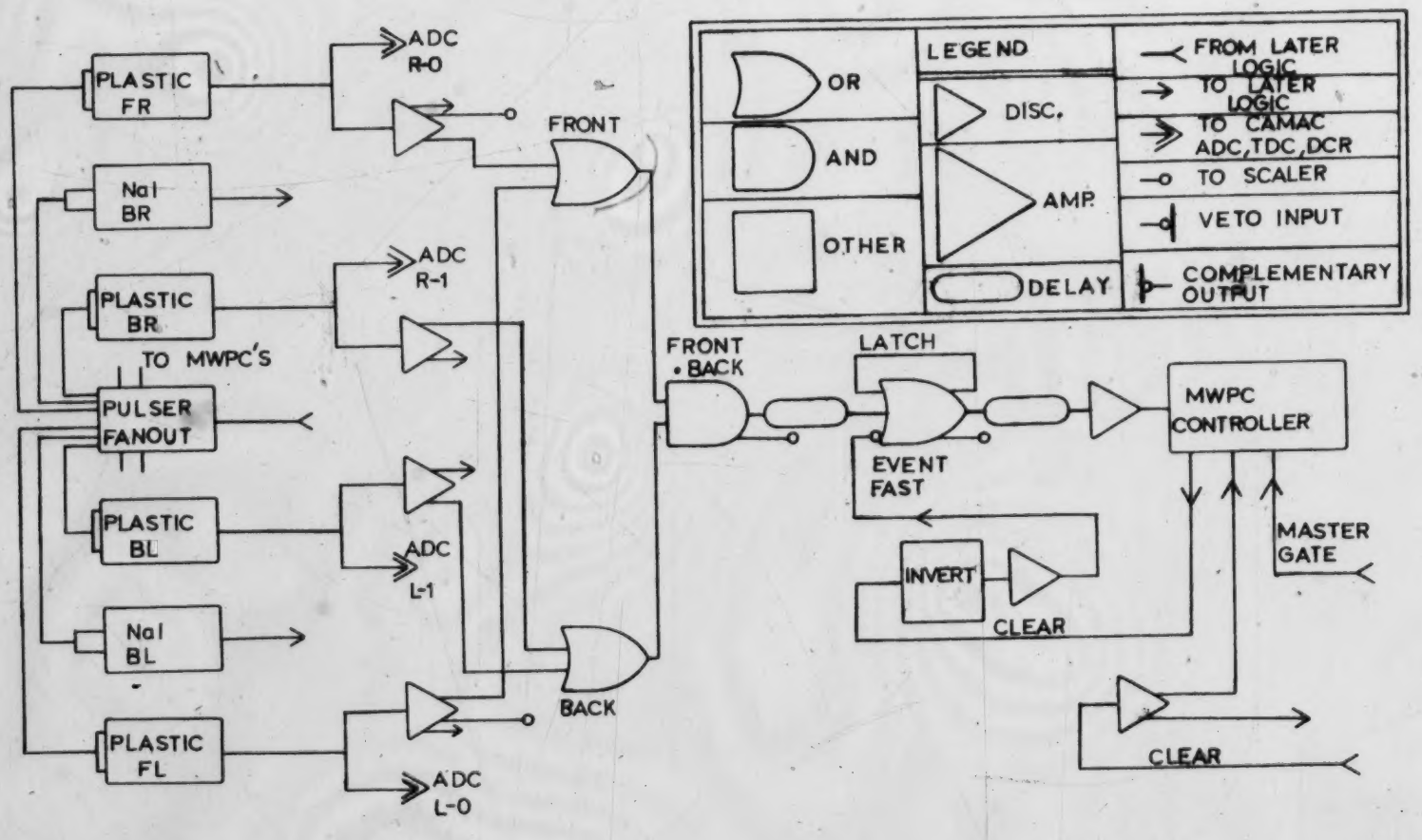

FIGURE 12. A block diagram of the electronics located in the experimental hall which were used for the back angle measurements. The legend in this figure is common to all of the electronics diagrams.

OR gate, preventing another event from starting until the first one was safely dealt with. At an appropriate time during the reset sequence, the controller cleared the latch, readying the EVENT FAST gate for another event. The latching process created a dead time which had to be accounted for; this problem is fully discussed in Section 2.7.

The majority of the electronics system was located in the remote counting room. One part of the remote electronics is shown in Figure 13; the exact symmetry of the electronics on the two sides should be noted. This stage of the electronics took the signals from the various detectors and made the basic decision whether to read the signals into the computer for further processing or to reject them. The relative timing arrangement of various signals is shown at important locations in the figure.

Figure 14 presents the second stage of the remote electronics, which dealt mainly with the control signals needed by the various components of the electronic system. The signals COMPUTER NOT BUSY and EVENT DONE, shown in Figure 14, were formed by the data acquisition computer in an output register in the CAMAC system. The MASTER GATE, similarly to the EVENT FAST gate discussed above, was latched while the current event was being processed by the computer.

The LEFT and RIGHT RETIME signals, which were formed in Figure 13, were placed in coincidence with a MASTER GATE signal. These coincidence signals started the left and right time-to-digital converters (TDC's) and gated the left and right analog-to-digital

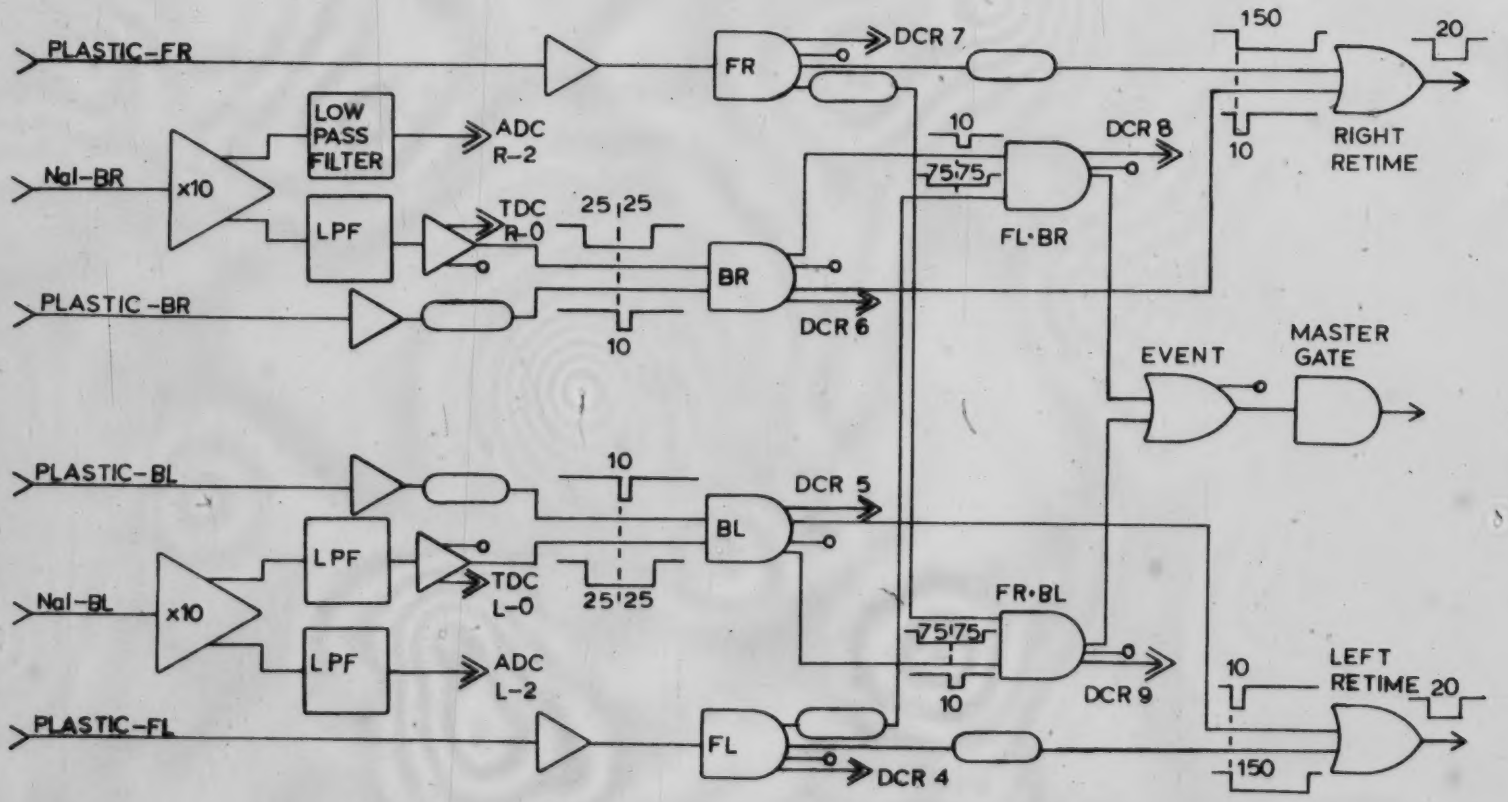

FIGURE 13. A block diagram of the first portion of the electronics located in the remote counting room, used for the back angle measurements (continued in Figure 14). The relative timing of various signals is shown at key points (all pulse widths are in nsec). The low pass filters (LPF's) removed high frequency noise originating in the NaI amplifiers.

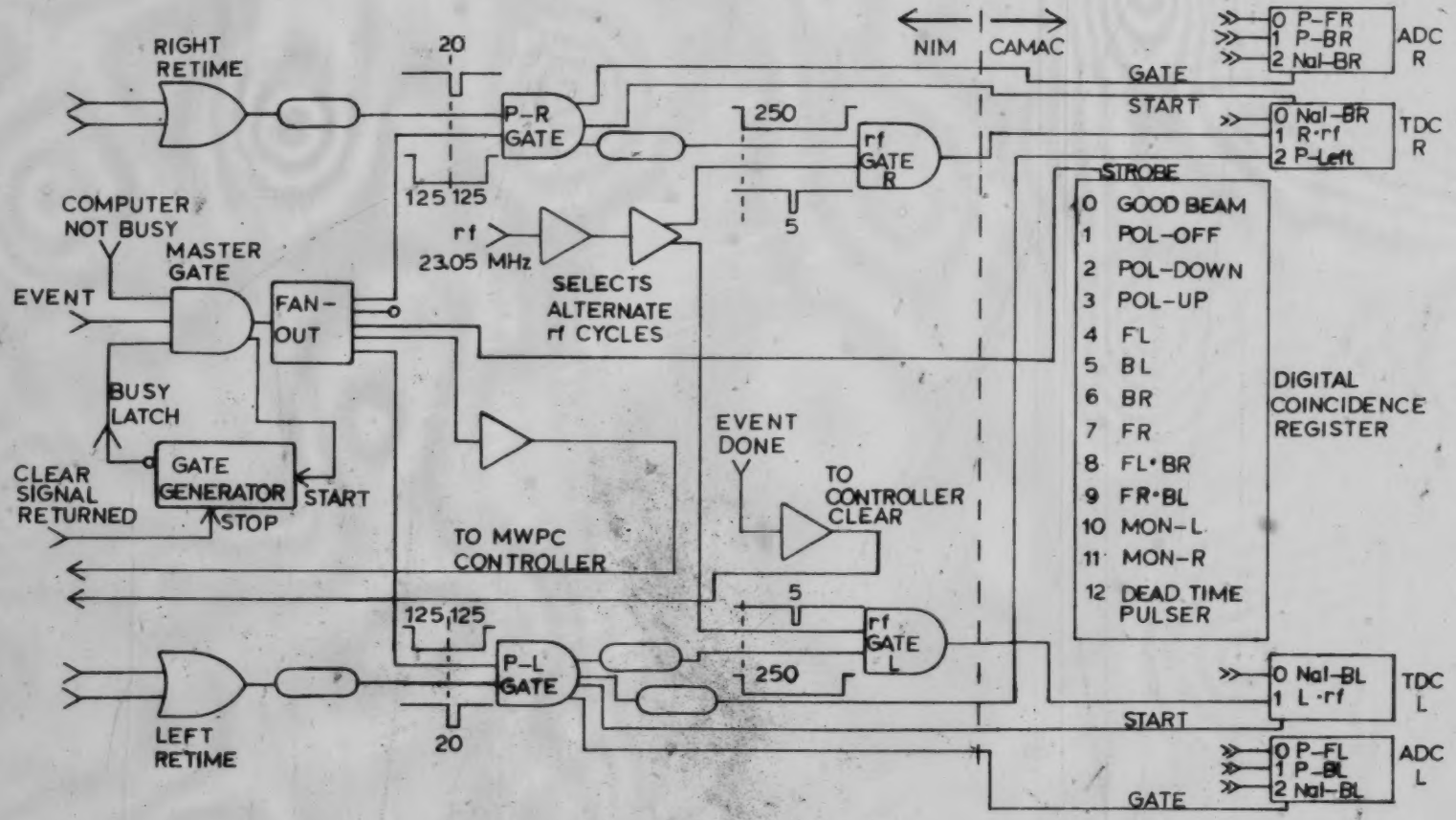

FIGURE 14. The second portion of the electronics located in the remote counting room, used for both the back angle and target thickness measurements.

converters (ADC's). These signals were more appropriate for those tasks than the MASTER GATE signals due to the fact that their timing was determined by either the front or back detector pulses on that side. In contrast, the MASTER GATE timing was set by the time of the BR or BL signals only. For example, the MASTER GATE signal had the time of the BL signal in a FR·BL coincidence; using that to start the right TDC would not have been appropriate.

The ADC's used for the experiment were multi-input (12-fold) CAMAC ADC's of the charge-integrating type (in contrast to the peak-sensing type); separate ADC's were employed for the left and right detectors and were gated as described above. The input signals were appropriately delayed while the logic was being performed.

The TDC's used were octal input (stops) CAMAC TDC's with one (common) start per TDC unit; separate TDC's were used for the left and right sides. The start signal originated with the appropriate plastic scintillator on that side, through the RETIME circuits. A left start signal was also delayed and used as an input to the right TDC, giving left-versus-right plastic scintillator timing.

Another CAMAC unit illustrated in Figure 14 is the digital coincidence register (DCR) (also called a bit pattern unit). This unit's function was to send to the computer a 24-bit word, with each bit representing the status of one input. The inputs used for the experiment are shown in Figure 14. This DCR word was recorded along with the data and was also used in forming spectra for on-line display. The POL-OFF, POL-DOWN, and POL-UP signals were DC-levels

given out by the polarized source spin controller. The GOOD BEAM signal indicated that the beam current from an ion chamber was between a lower and an upper set-point.

In addition to the above CAMAC devices, CAMAC scalers were also used to record the total number of counts from certain devices during a run. Table 1 gives a list of all quantities scaled during the experiment. Some of the sources for the scaler inputs are shown in Figures 12, 13 and 14. Some of the quantities scaled were vital to the usefulness of a run, others were necessary but could be obtained in later analysis in other ways, and still other quantities were not strictly necessary, and were scaled only as an indication that certain devices were functioning.

2.5.2 The Target Thickness Electronics

The target thickness was measured, as discussed fully in Section 3.1, by detecting small angle (13^0 or 14^0) elastically scattered protons in the forward telescopes and normalizing the results to previous measurements. For these measurements, NaI detectors were required on the front arms; the detectors on those front arms were counting single particles, that is to say, there were no inter-arm coincidences. Therefore, the electronics had to be reconfigured to accommodate these facts.

The first part of the electronics, that part which generated the EVENT FAST signal is shown in Figure 15. The prescalers are CAMAC modules which emit a pulse for every N input pulses. The cons-

TABLE 1

Signals Scaled

Elapsed Time - 100 Hz clock
Polarimeter - Left
Polarimeter - Left Accidentals
Polarimeter - Right
Polarimeter - Right Accidentals
Alpha Monitor - Left
Alpha Monitor - Left Accidentals
Alpha Monitor - Right
Alpha Monitor - Right Accidentals
Upstream Ion Chamber Integrator
Downstream Ion Chamber Integrator
Event
Master Gate
Dead Time Pulser
FL
FR
BL
BR
FL·BR
FR·BL
Prescaler Left
Prescaler Right
Constant Fraction Discriminator - BL
Constant Fraction Discriminator - BR
Plastic - FL
Plastic - FR
Back·Front
Event Fast

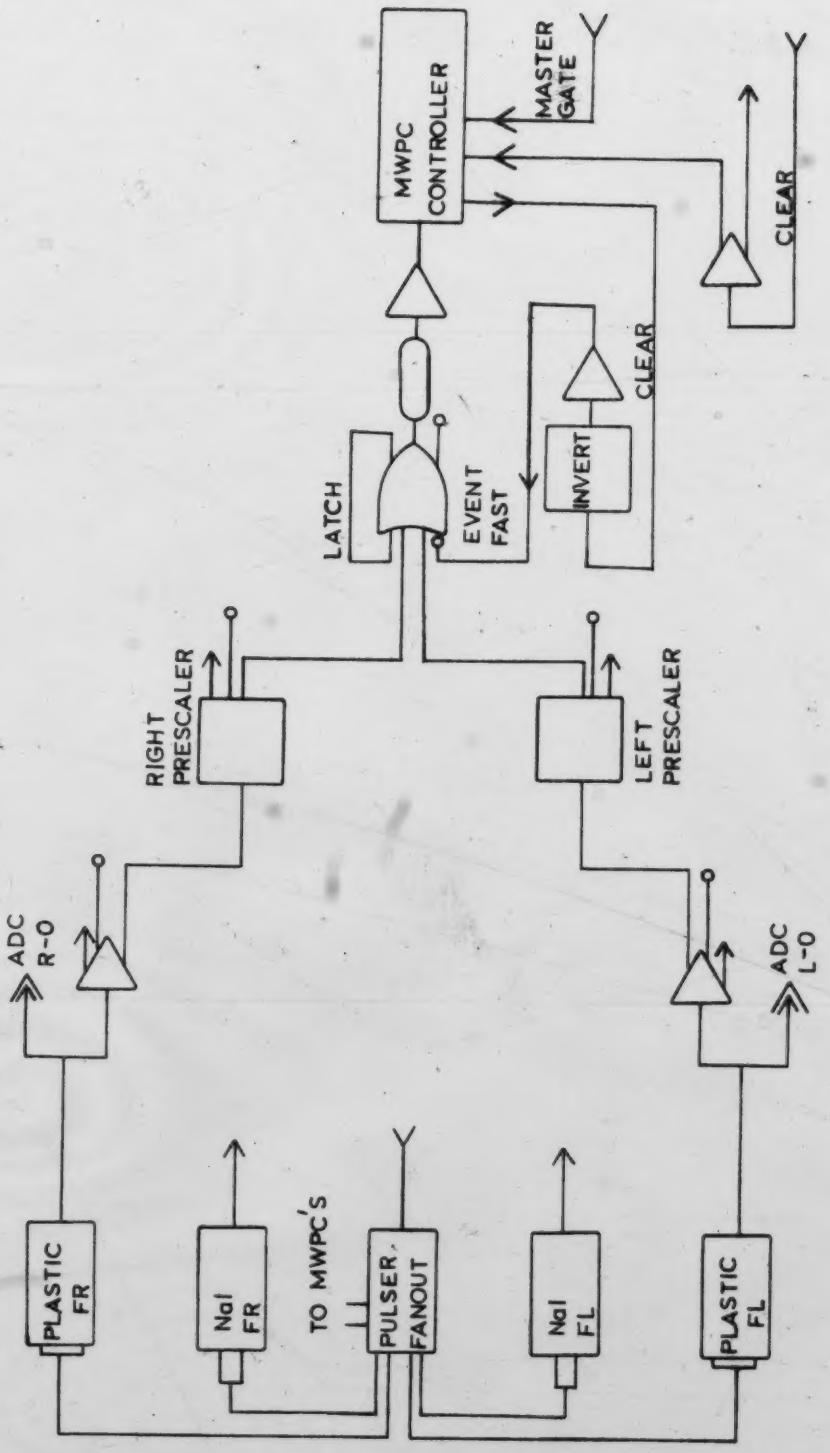

FIGURE 15. The electronics in the experimental hall which were used for the target thickness measurements.

tant N was remotely programmed into the prescaler via the computer. The prescalers were necessary because of the very large ratio of the forward angle differential cross sections to the backward cross sections ($> 10^5$ to 1). The MWPC controller circuitry after the EVENT FAST gate was unchanged, but is shown in Figure 15 for completeness.

The second stage of the electronic configuration, that part which generated the MASTER GATE signals, is shown in Figure 16. Since the target thickness measurements were interwoven with the back angle measurements, the electronics system was designed so that the changes between the two configurations were quickly done and could be accomplished with a minimal disruption to the main body of the electronics. The existing BR and BL electronics subsystems were used for the FR and FL signals in Figure 16 by changing inputs; the FL·BR and FR·BL coincidences became FR·PS-R and FL·PS-L. It should be noted, comparing Figures 13 and 16, that the CAMAC connections were unchanged. The electronics in Figure 14, i.e. everything at or after the MASTER GATE was unchanged.

2.5.3 The Monitor Electronics

The electronics arrangement for the four fixed monitor counters described in Section 2.4 is shown in Figure 17. Real proton-alpha coincidences were detected with this configuration, as were accidental, or simulated coincidences of a proton and an alpha particle from adjacent beam bursts. The two proton discri-

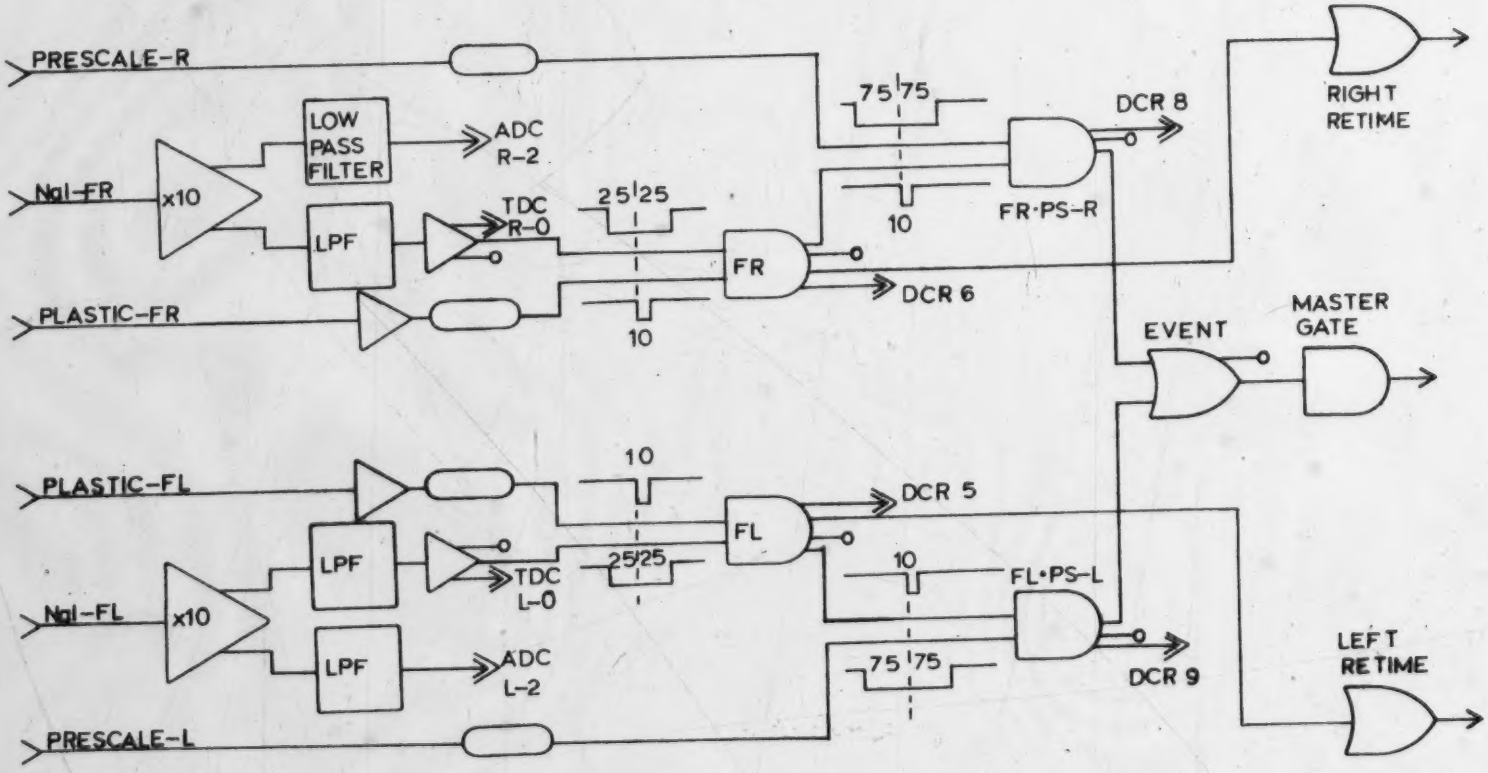

FIGURE 16. The portion of the electronics, located in the remote counting room, associated with the target thickness measurements.

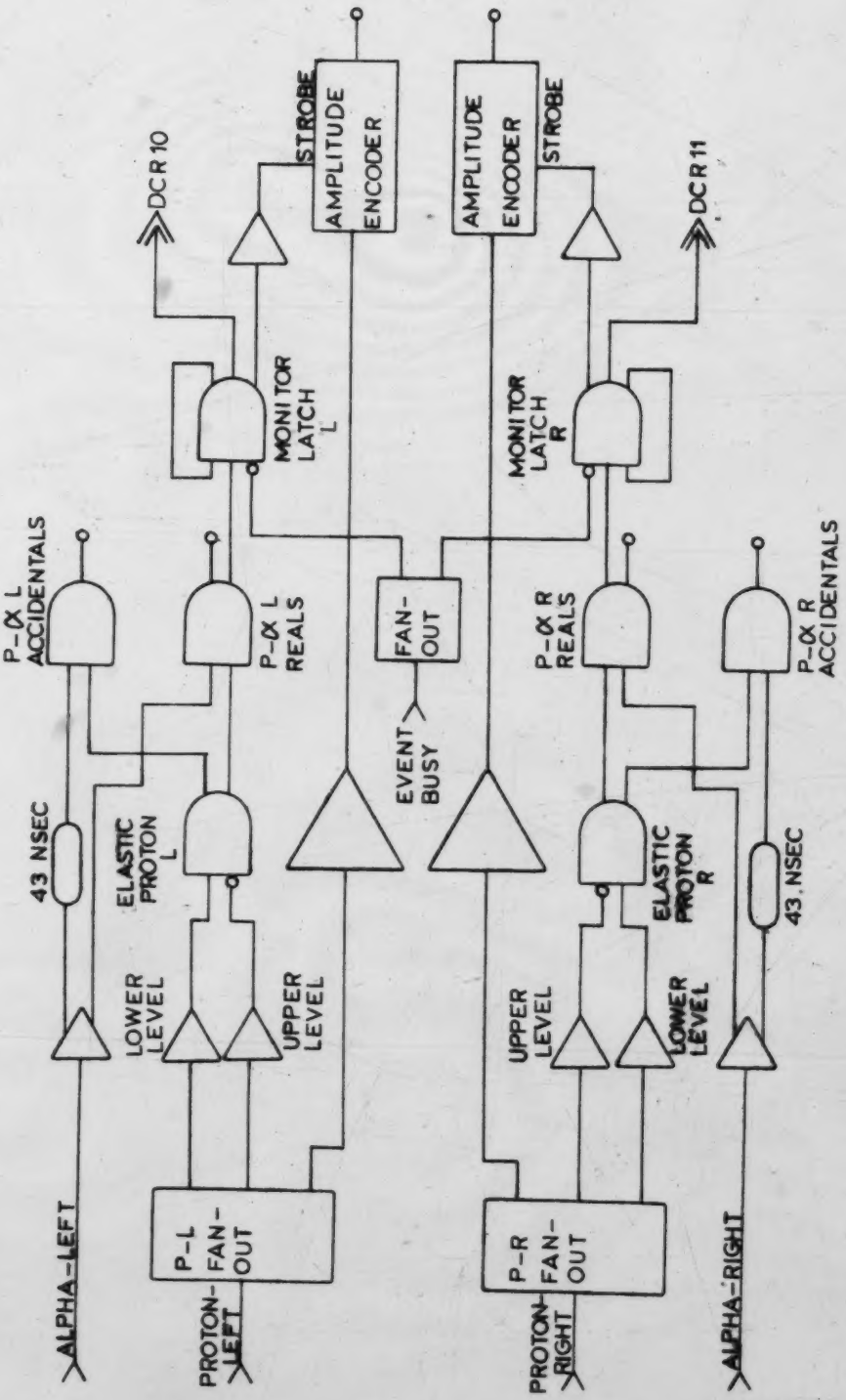

FIGURE 17. A block diagram of the stationary monitor counter electronics.

minators, one below in coincidence and one above in anticoincidence, were used to put a 'window' around the elastically scattered proton signals. The electronics after the real and accidental coincidence gates, including the monitor latches and amplitude encoders, sampled the proton signal pulse heights to guard against gain shifts or discriminator level changes. The amplitude encoders took the proton signals from one side, after amplification and translated the signal into a chain of pulses, the number of which were proportional to the input pulse amplitude. These pulse chains were counted by two special CAMAC scalers. While processing a full event, the computer read the scalers and translated the readings into two pulse height spectra. The monitor latches, which were cleared each time the computer read an event, ensured that only one monitor signal would be processed at a time.

2.5.4 The Polarimeter Electronics

The electronics system for the polarimeter is shown in Figure 18. Triple coincidences on the left and right sides, along with accidental coincidences were scaled following straightforward electronic processing.

2.5.5 The Data Acquisition System

The data acquisition system was centred around a Honeywell H316 minicomputer, interfaced directly to the three-crate CAMAC network. The general structure and operation of the data acquisition

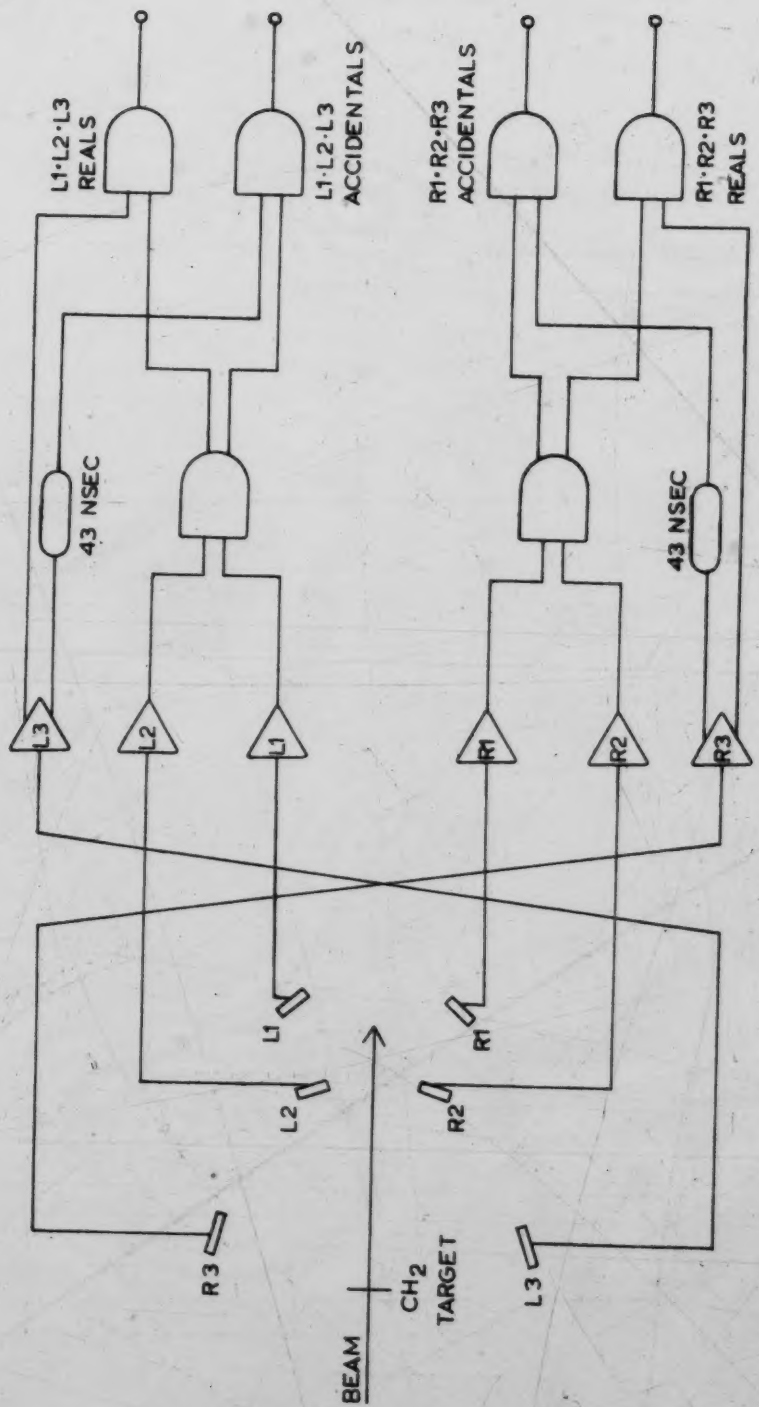

FIGURE 18. A block diagram of the polarimeter electronics.

system have been described in several internal reports (Ro-74, Ro-75a, Ro-75b, and Ro-77). In general, the computer read various parameters generated by the electronic system via the CAMAC interface. The program did a number of simple operations with this data and then wrote the information onto magnetic tape event-by-event, and/or stored selected portions of the data in the computer memory for display.

The magnetic tape event structure, written by the data acquisition program ORION used for the present experiment, is shown in Table 2. Because an arbitrary number of MWPC wires could be struck during a given event, the events had a variable length. Referring to Table 2, the first two words (16 bits per word) were for control purposes only. The third word, the LAM pattern, refers to the CAMAC Look-At-Me signals which are issued by individual CAMAC modules when the module needs the attention of the computer. The next two words, 3 and 4, were the DCR words. Words 5-18 contained the values read from various TDC or ADC channels. Some spare words were included here for flexibility and to act as back-ups. The next four words, the time and event scalers, were recorded for each event so that it would be possible to analyze only part of a file, should something fail part way through it. The next four words, 23 through 26, were the readings of the two scalers connected to the alpha monitor amplitude encoders, as explained previously. The next word in an event contained the number of wires hit (plus one), and the MWPC coordinates (the absolute MWPC wire numbers struck for each event) filled the rest of the event structure.

TABLE 2

ORION Magnetic Tape Event Structure

Word Number	Parameter	Comment
0	- (Length of Event)	
1	Flag (-1 or -2)	
2	LAM PATTERN	
3-4	DCR (24 bits)	
5	TDC L-0	NaI - BL
6	TDC L-1	L·rf
7	TDC R-0	NaI - BR
8	TDC R-1	R·rf
9	TDC R-2	Left Time
10	ADC L-0	Plastic - FL
11	ADC L-1	Plastic - BL
12	ADC L-2	NaI - BL
13	ADC L-3	Spare - Not Used
14	ADC R-0	Plastic - FR
15	ADC R-1	Plastic - BR
16	ADC R-2	NaI - BR
17	ADC R-3	Spare - Not Used
18	ADC R-4	Spare - Not Used
19-20	Scaler - Time	
21-22	Scaler - Event	
23-24	Scaler: α-mon - L	
25-26	Scaler: α-mon - R	
27	MWPC hits + 1	
28-end	MWPC coordinates	

Table 3 presents a list of the 29 spectra that were stored in memory and were available for on-line inspection. Restrictions imposed by the available memory space forced a careful selection of the most useful spectra to display, especially the biparametric spectra, which take up much more room in memory than simple histograms. Column 2 in Table 3 gives the parameter(s) that made up the spectrum, and column 3 lists the number of channels alloted for that spectrum. The fourth column lists the gating requirements for storage of data into that particular spectrum. The first number gives the locations (in octal) of the DCR bits (see Figure 14) that were tested and the second figure is the result (in octal) that was required for the data to be stored in the spectrum. For example, in spectra 13 and 25, bits nine and ten (counting from the least significant bit) were tested; bit nine must have been set, bit ten not set. The fifth and last column in Table 3 gives a description of the spectrum parameters.

The wire chamber spectra, numbers 17 to 24 in Table 3, used decoded wire numbers, i.e. chamber hits were decoded into the appropriate planes. If several adjacent wires in a plane were hit, or if the hits were on non-adjacent wires, but with a gap of two or less wires between the groups, the highest wire number struck was incremented by one count. However, if the hits were on non-adjacent wires with a gap greater than two wires, the last channel in that spectrum was incremented. If no wires in a plane were hit, channel 0 in the spectrum was incremented. Usually, excessive counts in either the first channel (missing hits) or the last channel (non-adjacent mul-

TABLE 3

Spectra Stored in Memory

Spectrum Number	Parameter(s)	Length (channels)	Gating Requirement*	Comments
1	ADC L-0	256	20-20	Plastic - FL
2	Spare - Not Used			
3	ADC L-1	256	40-40	Plastic - BL
4	ADC L-2	512	40-40	NaI - BL
5	ADC R-0	256	200-200	Plastic - FR
6	Spare - Not Used			
7	ADC R-1	256	100-100	Plastic - BR
8	ADC R-2	512	100-100	NaI - BR
9	TDC L-0	256	40-40	NaI - BL
10	TDC L-1	256	20-20	rf · FL
11	TDC R-0	256	100-100	NaI - BR
12	TDC R-1	256	200-200	rf · FR
13	TDC R-2	512	1400-400	FL - BR
14	TDC R-2	512	1400-1000	FR - BL
15	Scaler (23-24)†	256	2000-2000	α-mon - L
16	Scaler (25-26)†	256	4000-4000	α-mon - R
17	Y - FL	128	20-20	
18	X - FL	128	20-20	
19	Y - FR	128	200-200	
20	X - FR	128	200-200	
21	Y - BR	128	100-100	
22	X - BR	128	100-100	
23	Y - BL	128	40-40	
24	X - BL	128	40-40	
25	ADC L-0 vs ADC R-2	4096 (64x64)	1400-400	E_α - FL vs E_p - BR
26	ADC R-0 vs ADC L-2	4096 (64x64)	1400-1000	E_α - FR vs E_p - BL
27	DCR	16	0-0	Low Order 16 Bits
28	LAM PATTERN	16	0-0	
29	RATE	2048	0-0	Number of Events Acquired per Unit Time

*DCR Bits Tested - Value Required

†Event Word Number, See Table 2

tiples), or both, indicated that the count rates were too high in the chamber or that the gas mixture was not optimum.

The last spectrum, number 29, labelled RATE in Table 3 was very helpful in controlling the data taking rate. The computer stored the number of events acquired in successive time intervals into consecutive channels in the spectrum. This spectrum represented the relative data-taking rate as a function of time, and could show, for example, a slow drop in the extracted beam current over a long period of time.

2.6 Data Analysis

The data analysis for the experiment was performed off-line with the data acquisition computer. The data analysis program (described in Ro-75b) was very similar to the data acquisition program, except that it accepted data from magnetic tape instead of the CAMAC interface. The program selected events using the gating procedure described in Section 2.5 and rewrote those events onto magnetic tapes and/or binned that data into selected histograms. While the basic program used the same histograms as the acquisition program (see Table 3), the histogram parameters and gating requirements could be altered to enable other information to be examined. In particular, several other biparametric spectra were examined in the analysis.

In addition, the data analysis program had several software 'windows' that could be placed around regions of interest for selected parameters. The selection of events using these 'windows' was done

with the same gating procedure which has been described for the DCR bits.

A typical, on-line E_p-vs.-E_α spectrum is shown in Figure 19. The prominent peak in the upper right is the dead time pulser (to be discussed in Section 2.7), the peak near the center is the elastic scattering peak and the peak in the bottom left is from the reaction $p + {}^4He \rightarrow d + {}^3He$. The marked prominence of the peaks of interest above the general background shows the efficacy of the E_p-vs.-E_α spectrum in identifying the reaction channels and also illustrates how well the experimental arrangement separated the elastic scattering (and reaction) process(es) from backgrounds.

Analysis of the backward scattering data was initiated by putting generous windows around the proton and alpha energies corresponding to the elastic scattering peak in the E_p-vs.-E_α spectra. The overlap region of the two windows applied at this stage of the analysis is also shown in Figure 19.

These windows were the criteria for the storage of events into the front-back timing spectra (numbers 13 and 14 in Table 3). The on-line spectrum of relative front-back time corresponding to Figure 19, is shown in Figure 20. The three peaks evident are from the elastic scattering reaction, the (p,d) reaction, and the dead time pulser, as indicated in the figure. The two energy windows, applied to this spectrum, produced a very sharp, clean timing peak and a small number of events with a random distribution in time.

The next stage of the analysis used a single window around this timing peak to store events in all spectra. The spectra were

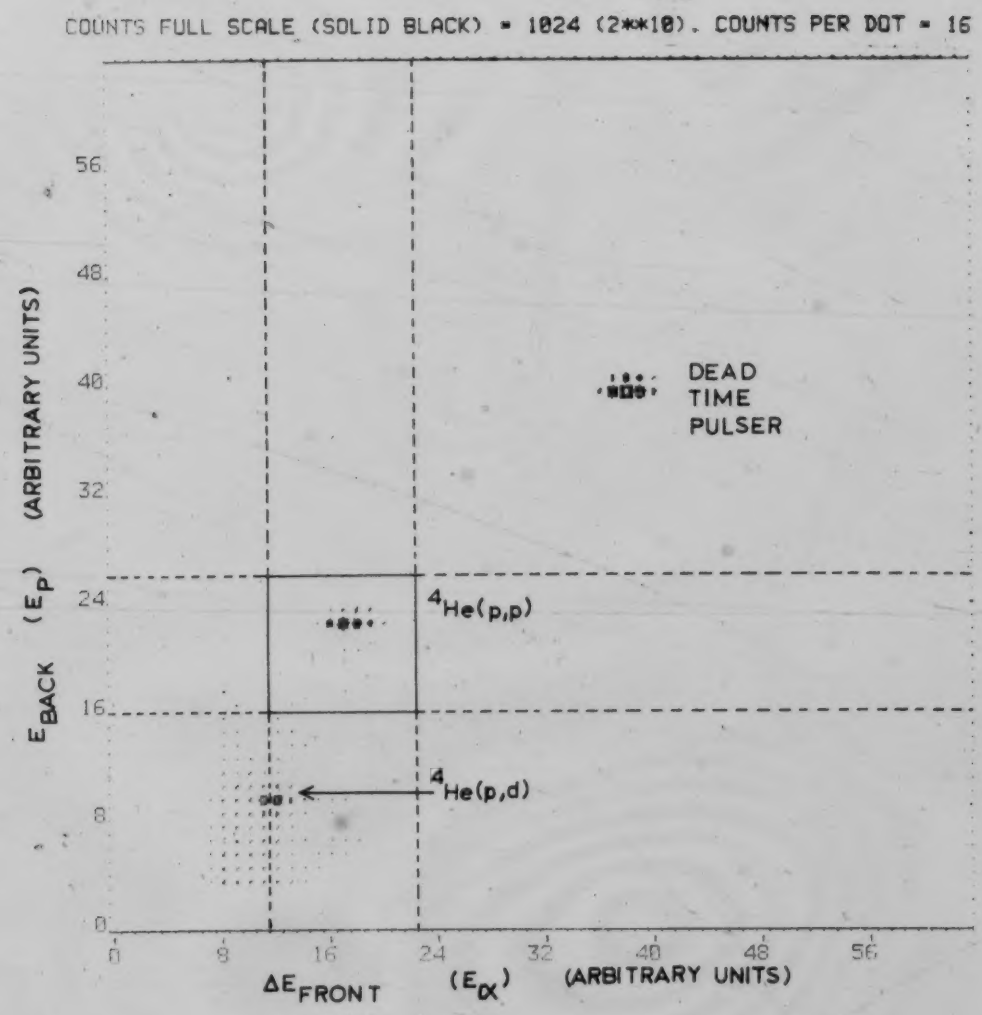

FIGURE 19. A typical, on-line E_p-vs.-E_α spectrum, taken at E_{beam} = 350 MeV, $\theta_p = 152^0$, $\theta_\alpha = 10^0$. The lines show the preliminary energy windows used to define elastic scattering events.

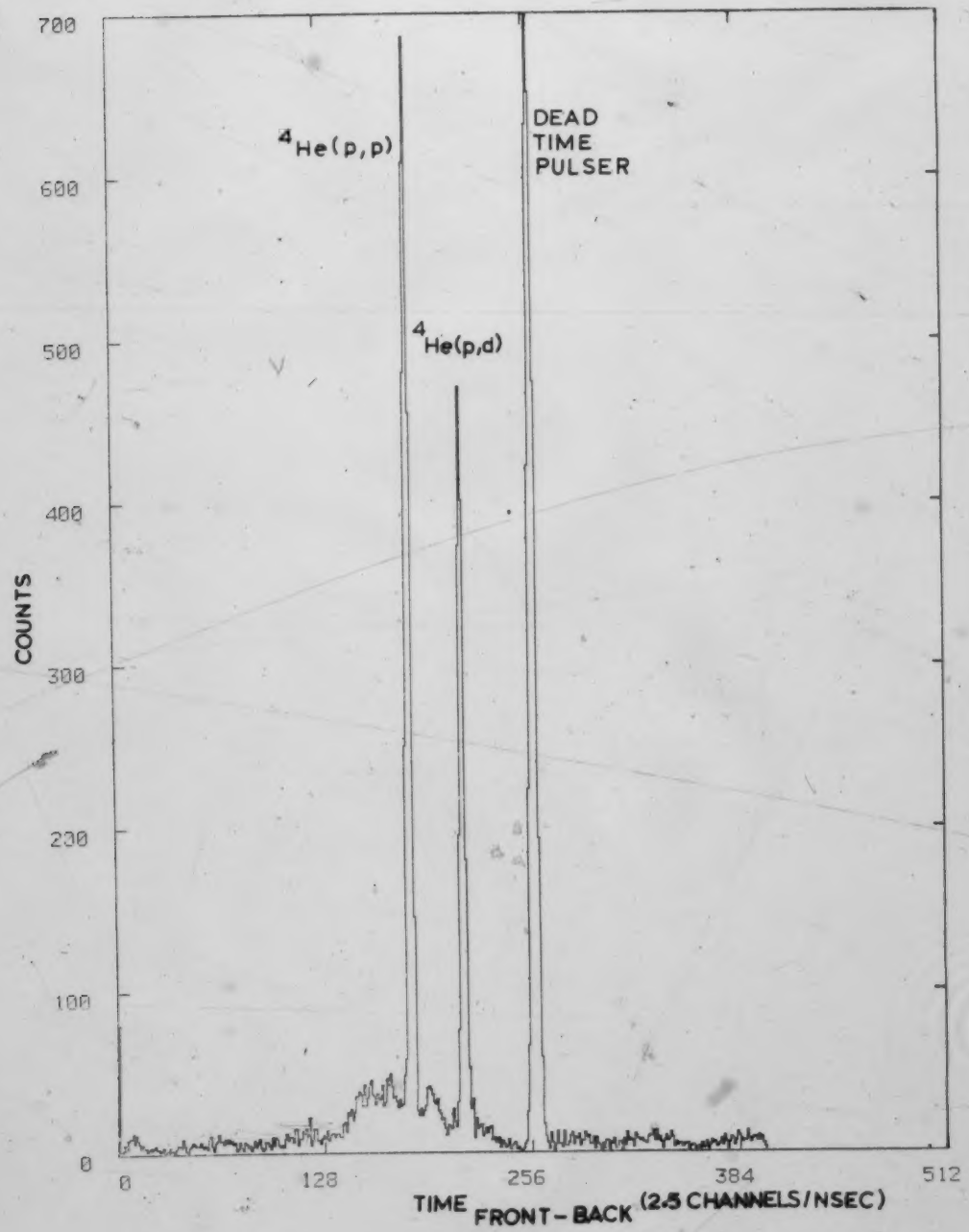

FIGURE 20. The on-line, front-back timing spectrum corresponding to Figure 19.

examined to ensure that elastic scattering events were not being eliminated accidentally. For example, the thresholds in all counters were examined to verify that events of interest were not being rejected.

Next, the one-dimensional energy spectra were examined to select tighter windows on E_p and E_α to better isolate elastic scattering events. As an example, Figure 21 shows the data in Figure 19 projected onto the proton axis. The left half, Figure 21 (a), shows the on-line data, with the preliminary energy window indicated. Figure 21 (b) shows the same data with the timing window applied, and also indicates the final energy window. It should be noted that those events in Figure 21 (b) with less than full energy are mainly elastic scattering events in which the proton underwent a nuclear reaction in the NaI counter.

Events were observed from inelastic proton scattering from ^4He, leaving ^4He in one of three excited states (all particle unstable) with excitation energies just above 20 MeV (Fi-73):

$$p + {}^4He \rightarrow p' + {}^4He^* \rightarrow \begin{cases} p + ({}^3He + n) \\ p + ({}^3H + p). \end{cases}$$

An on-line spectrum of events plotted as a function of proton energy is shown in Figure 22; this spectrum was collected at $\theta_{proton} = 158^0$ (laboratory) at 185 MeV. The inelastic peak, very evident in Figure 22 and also visible in Figure 21, was in all cases cleanly separated

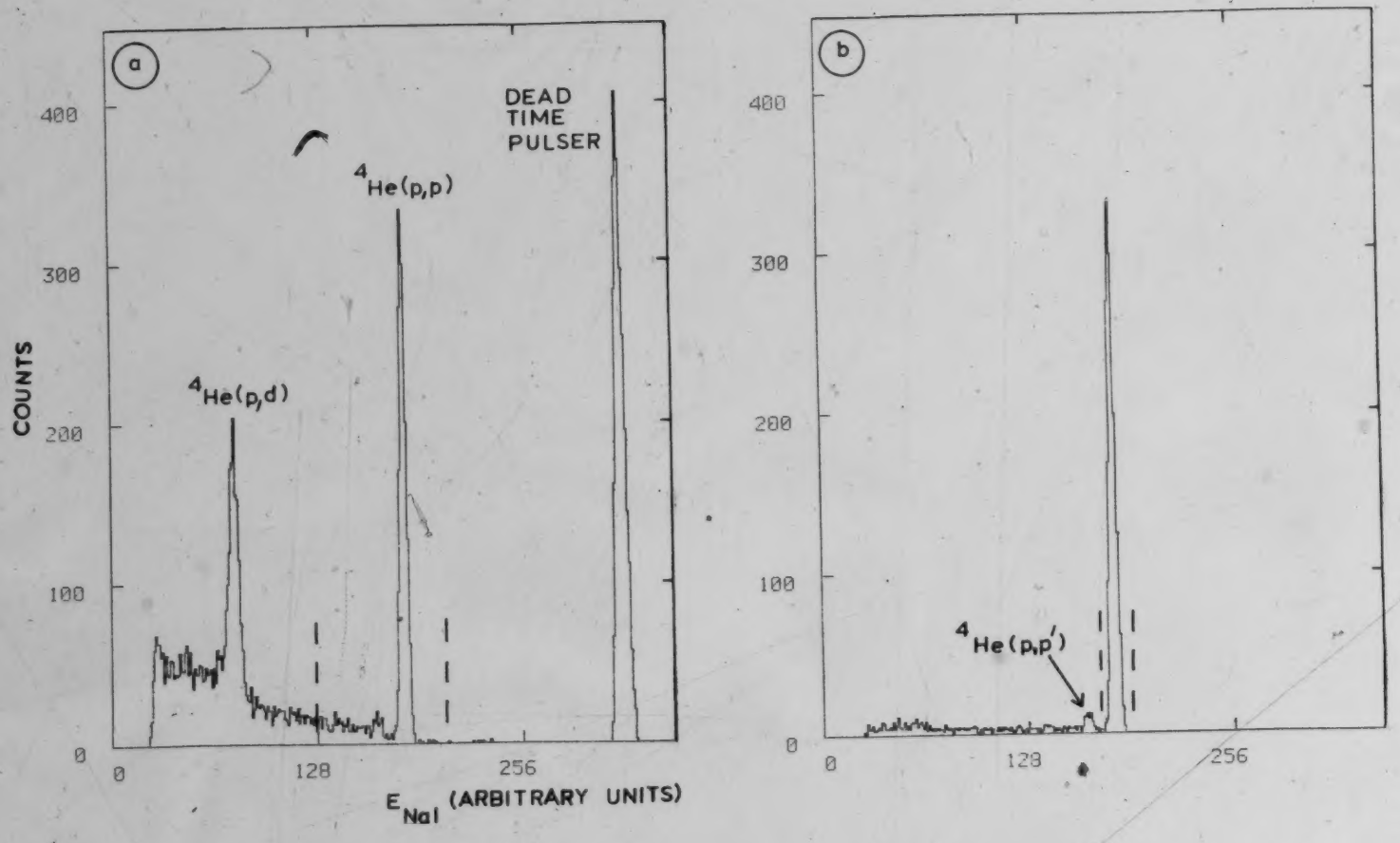

FIGURE 21. (a) The events of Figure 19 projected onto the E_p axis. The dashed lines show the preliminary energy window indicated in Figure 19.
(b) The same data as (a), but with a timing window applied. The final energy window defining elastic scattering events is indicated by the dashed lines.

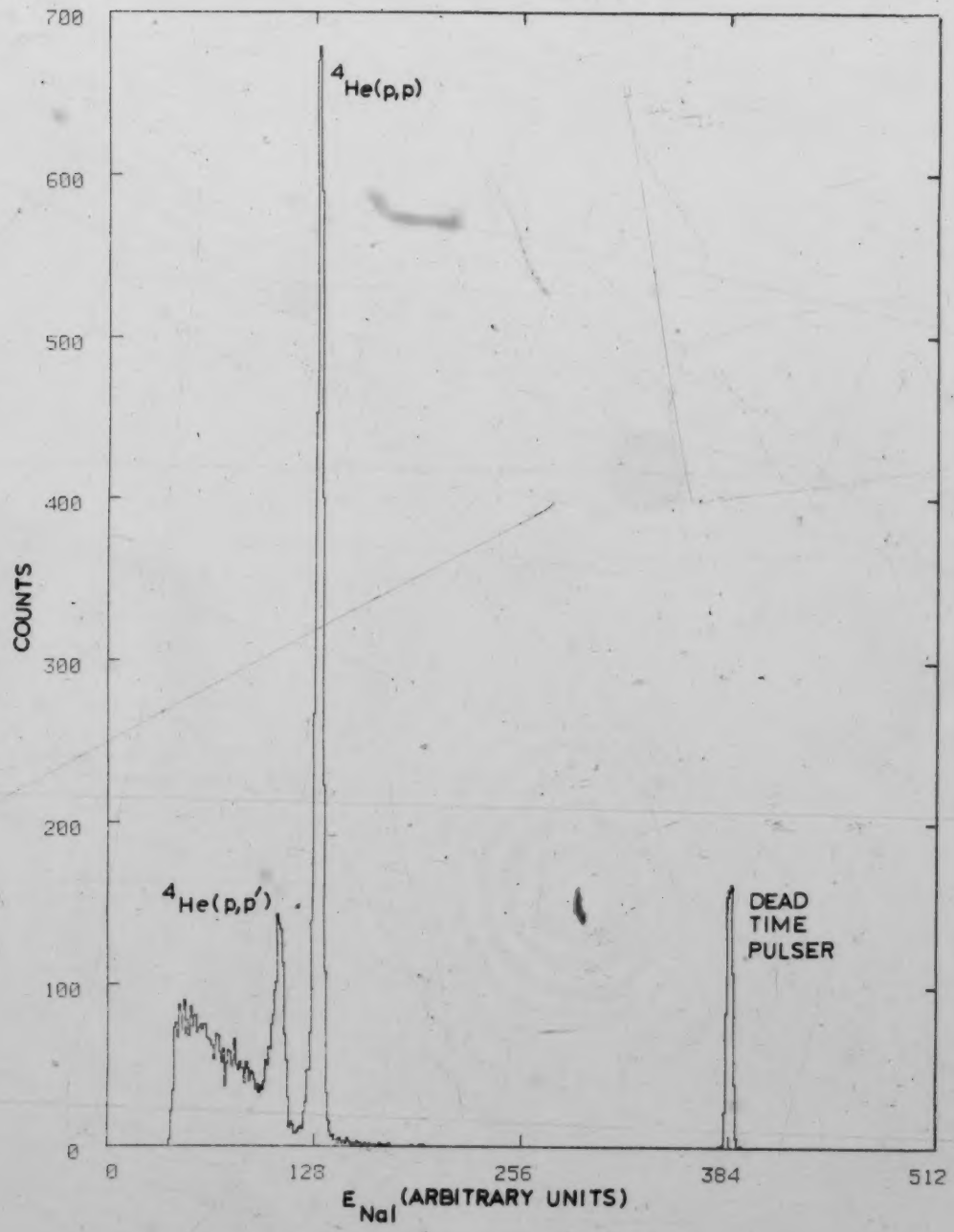

FIGURE 22. An on-line spectrum of events plotted as a function of proton energy, showing a prominent inelastic proton scattering peak. The spectrum was obtained for an energy of 185 MeV for $\theta_p = 158^0$.

from the elastic peak.

The last stage of data selection used the timing window and the smaller energy windows on E_p and E_α to define good elastic scattering events. In addition, windows were placed on the back wire chamber coordinates to accurately define the solid angle for the experiment. This centrally located window was 24 wires wide (2.50^0) by 36 wires high (3.75^0) for an acceptance of 2.88×10^{-3} sr in each arm.

Events satisfying these five criteria were studied using biparametric plots of $X_{FRONT} - Y_{FRONT}$, $X_{FRONT} - X_{BACK}$, and $Y_{FRONT} - Y_{BACK}$ for selected runs. For example, the $X_{FRONT} - Y_{FRONT}$ spectrum was used to determine the optimum size for the back MWPC window.

The number of events satisfying these five criteria (one timing, two energy and two MWPC requirements) were counted for both telescope combinations as valid elastic scattering events. From these numbers the cross sections and analyzing powers presented in Chapter III were calculated.

Several runs were made with the empty target. A typical, on-line E_p-vs.-E_α spectrum for such a run is shown in Figure 23. The windows in Figure 23 are the same windows that would have been used in a target-full run to pick out elastic scattering events (see Figure 19). It should be noted that the empty target was used for approximately one seventh of the charge on target of the run corresponding to Figure 19, but that the scale in Figure 19 is 16 counts per dot as opposed to one count per dot in Figure 23. The

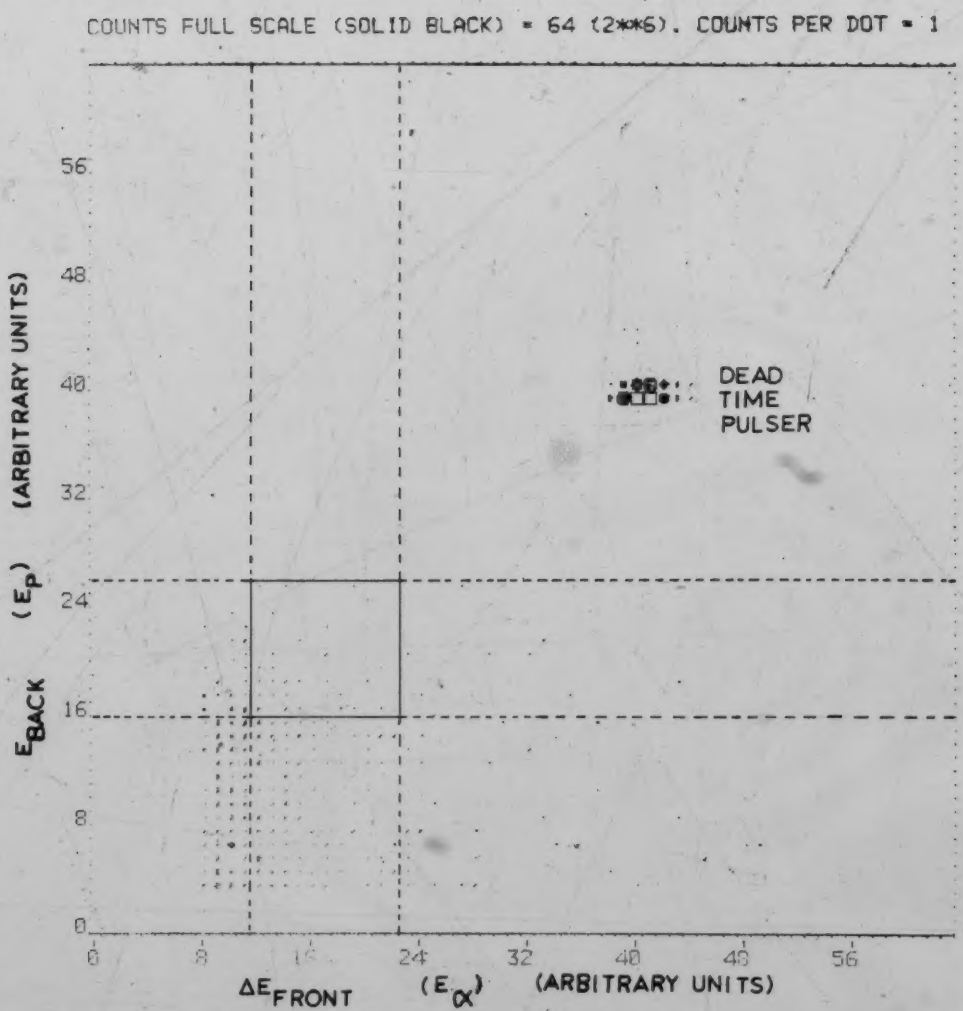

FIGURE 23. An on-line E_p-vs.-E_α spectrum with an empty target, taken at an energy of 350 MeV for $\theta_p = 168^0$, $\theta_\alpha = 4^0$. The windows indicated are the windows used to define elastic scattering events for a full target run (Figure 19).

very low number of counts within the outlined area illustrates that the experiment had virtually no background in the region of interest from the target walls.

To further investigate the possible backgrounds, analyses were made of selected runs with the timing window shifted by the time of one r.f. cycle. This showed that accidental coincidences of a proton and an alpha particle (with the appropriate energies) from different beam bursts were a negligible proportion of valid events.

2.7 Dead Time Corrections

The dead time of a system is defined as that portion of the time that it was unable to accept new data because the system, or any integral part of it, was fully occupied with previous data. The dead time of the present system included that produced by latches on important gates (see Section 2.5), in addition to the computer dead time.

To deal with this, a monitoring system was used which measured the overall dead time of the system. Light-emitting diodes (LED's) were attached to all of the plastic scintillators and NaI detectors and were flashed by a pulser system. These pulses were also applied to one wire of each sense plane of the MWPC's to include them in the monitoring. The fraction of these pulses that was not eventually recorded by the computer was a direct measurement of the composite dead time of the system.

The electronic set-up that provided the 'dead time' pulses

is shown in Figure 24. A source of pulses whose rate was proportional to the beam intensity was provided by the sum of the polarimeter left-plus-right coincidences. The number of counts was prescaled to decrease the LED pulsing frequency to a rate approximately equal to the counting rate of elastic scattering events. Two separate pulsers were used: (1) a triggerable NaI pulser unit which emitted carefully shaped pulses so that the light from the LED's would have approximately the same time distribution as scintillation light from NaI, and (2) a plastic scintillator pulser which was similar, but emitted much faster pulses in accordance with the properties of the plastic scintillator used. The dead time pulses were inserted into the MWPC system between the actual sense wire and the electronics for that wire. The amplitude of the pulser signals was adjusted so that the signals were in a different portion of the spectrum than the pulses of interest (see Figure 19).

To identify pulser events in the data analysis, the DCR bits for the dead time pulser and for the appropriate front-back coincidence were both required. MWPC dead times would be reflected in missing hits, for which channel 0 of the appropriate MWPC spectrum was incremented; in addition, the analysis of real events used back MWPC windows that eliminated non-adjacent multiple MWPC hits (the last channel in the MWPC spectra). In order to include these effects in the dead time analysis, two windows were set to eliminate pulser events with counts in the first and last channels of each sense plane spectrum for the back MWPC's. Since the front MWPC's were not used in the final analysis of real events, it was not necessary to include

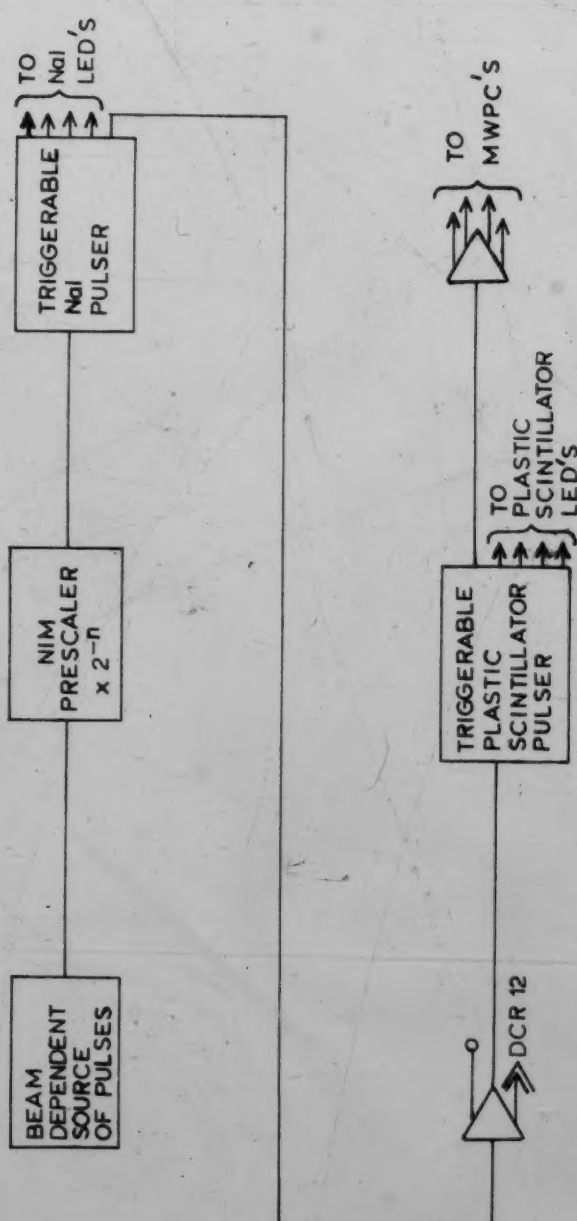

FIGURE 24. A block diagram of the electronic system that provided the 'dead time' pulses.

them in the dead time analysis. The number of pulser events found above was divided by the number of pulser events that were sent to the counters (see Figure 24), to establish the total live time (live time ≡ 1. - dead time). These correction factors were applied to determine the number of events that would have been counted by a totally live system (note that each telescope combination had a separate live time value).

The large angle measurements had low counting rates, so the dead times were correspondingly small. They were found to be less than 5% for the majority of the runs, although a few runs had dead times up to 11%, usually for those runs at the largest backward angle (i.e., the most forward angle for the front counters).

A measure of the computer dead time alone was the ratio of the number of MASTER GATE counts to the number of EVENT counts (see Figures 13 and 14). The EVENT counts were the number of back-front coincidences that were formed, and the MASTER GATE counts were those EVENT signals that were accepted into the computer for processing. The remainder of the EVENT signals were blocked by the MASTER GATE latch discussed in Section 2.5. The computer dead time was found to be the largest contributor to the total dead time of the system, as was expected. Typically, approximately 70% of the total dead time of the system was attributable to the computer, although this ratio did fluctuate somewhat.

CHAPTER III

EXPERIMENTAL RESULTS

3.1 Normalizations

The most crucial factor in measuring accurate cross sections in nuclear physics experiments is the determination of the absolute normalization of the data. The absolute normalization depends on two important factors, the absolute value of the beam current passing through the target, and the effective thickness of the target at the time that the experiment was performed.

3.1.1 Beam Flux Normalizations

The beam intensity was monitored by two helium-filled ion chambers, placed in the beam line downstream of the target location. High purity helium was continuously flushed through the ion chambers to prevent the buildup of impurities that might have changed the gain of the gas. The currents generated by the ion chambers were taken to current integrators, which produced digital outputs proportional to the charge collected. In addition, the total, net counting rate in the polarimeter provided another relative beam intensity monitor. These monitors provided three independent measurements of the relative beam intensity, which produced consistent results at the 3% level throughout the experiment. Small fluctuations ($\leq$ 3%) in the monitor results relative to one another did occur as long term effects, for example over a 24 hour period.

A separate measurement was performed utilizing a Faraday cup having a design similar to the one described by Barrett et al. (Ba-75) to obtain an absolute normalization for the ion chambers. The calibrations were performed at 200 MeV and 500 MeV with beam currents ranging from 60 pA to 11 nA. The ratio of the ion chamber integrated charge to the Faraday cup integrated charge varied within a 2% range, but without any systematic dependence on the average current. The ratio of the sum of the polarimeter left-plus-right counts to the Faraday cup output also varied within a 2% range, again with no systematic dependence on the current.

The ion chamber gain (the current collected / the actual beam current as measured by the Faraday cup) was found to be directly proportional to the energy loss (dE/dx) of protons in helium to within 2%. Therefore the gain of the ion chamber (the upstream ion chamber was chosen as the standard for this experiment) at energies other than 200 and 500 MeV was calculated assuming this proportionality with the proton dE/dx values. The gain of the upstream ion chamber is presented as a function of proton energy in Figure 25, with the actual values of the gain used in the calculations given in Table 4.

The ion chamber normalization uncertainties are estimated to be ± 5%. Approximately one half of this total uncertainty may be considered a relative uncertainty between the ion chamber gains at different energies. Part of this uncertainty originated with the small fluctuations in the results from the two ion chambers and

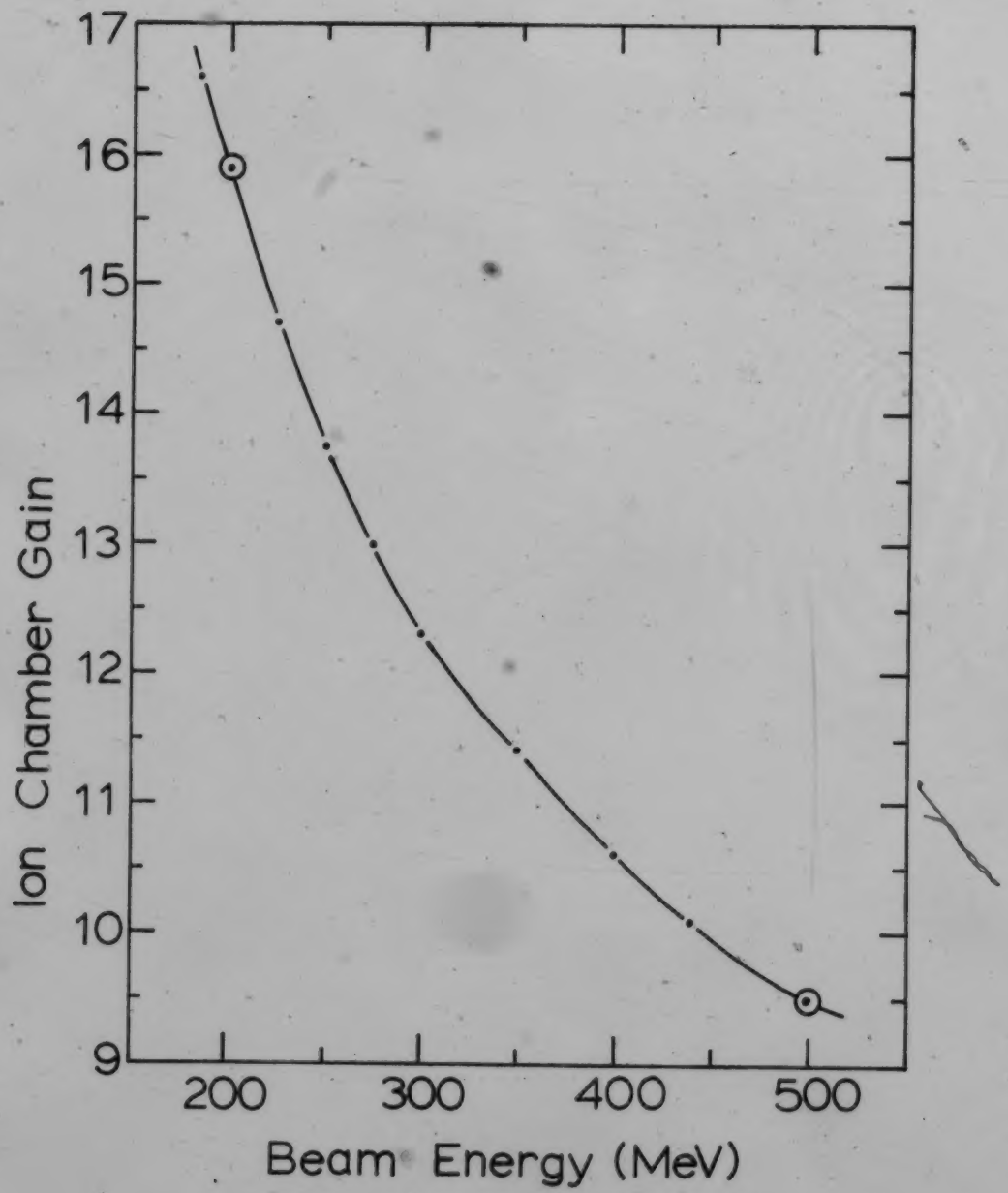

FIGURE 25. A plot of the ion chamber gain as a function of beam energy. The measured points are circled. The curve is proportional to the energy loss of protons in helium. The other points were obtained assuming the proportionality of the gain to the proton energy loss.

TABLE 4

Ion Chamber Gain vs. Proton Energy

Proton Energy (MeV)	Ion Chamber Gain
185	16.6
200	15.9
225	14.7
250	13.75
275	13.0
300	12.3
350	11.4
400	10.6
440	10.1
500	9.5

the polarimeter relative to one another (previously discussed). The assumption that the ion chamber gain follows the proton energy loss may not be strictly correct, also. For example, the ion chambers may not have operated in a strictly proportional mode. The other half of the total uncertainty may be considered an overall scale uncertainty, due to the fact that the Faraday cup itself may not be a perfect charge collector at these energies. (Significant charge loss would not have resulted, however, from nuclear reactions in the ion chambers upstream from the Faraday cup.)

3.1.2 Target Thickness Determination

Although the target cell used for the present experiment (as described in Section 2.3) had a nominal thickness of 5.0 mm, deformation of the nickel foil windows increased that thickness, while the possibility of the liquid helium boiling due to heat input from the beam and/or from some other source could lead to a lower average density of helium nuclei in the target.

Therefore, the target thickness was determined with an in-beam experiment. As discussed previously, the detector configuration (see Section 2.4) and the electronics (see Section 2.5) were designed so that minor modifications changed the setup from measuring back angle cross sections with a front-back coincidence to measuring small angle cross sections with the front telescopes only. The differential cross sections for p-^{4}He elastic scattering have previously been measured between 4^0 and 15^0 (proton laboratory angles) at 200, 350 and 500 MeV by the present experimental group and the results have been reported elsewhere (St-77). This measurement was

performed using an unconventional experimental technique utilizing a gaseous helium target which enabled the absolute cross sections to be determined very accurately. Therefore, those cross sections were used to determine the present, effective target thickness.

The back angle cross sections were measured in two major experimental runs, and the thickness measurement was performed twice during each run: at 500 MeV and 350 MeV during the first run and at 200 MeV and 500 MeV the second.

Because of the larger cross sections and the resulting high count rates at very small angles, the thickness measurements were made at as large an angle as was feasible. The first two measurements were taken at a central angle of 14^0, but, during the analysis, the solid angle defining MWPC windows were shifted to be centered about 13.6^0 to ensure that the detected protons were not affected by the walls of the horn (either by attenuation or by inscattering). The second two runs were done at a central angle of 13^0 to minimize these problems. The resulting target thicknesses were the same for these different angles.

In the analysis of the data, windows were placed on the two wire chambers, defining the active area to be 15 wires wide (0.64^0) by 30 wires high (1.28^0), for a solid angle acceptance of 2.52×10^{-4} sr in each arm. The windows restricted protons to a small, central area of the detector because, as is discussed in reference (Ca-77), the efficiency of the NaI counter telescopes drops very rapidly near the edges for high incident proton energy. The small active area ensured that at each energy, the efficiency would be approxi-

mately constant for all particles selected.

The events satisfying these two windows, having the required DCR bit present (signifying either FL·PS-L or FR·PS-R) and with all dead time pulser events vetoed, were binned according to the proton energy in the NaI counter. The NaI counting rates had been adjusted so that the fraction of the total number of pulses that 'piled-up' was negligible. The number of counts in the full-energy peak was simultaneously corrected for the dead time of the system, as discussed in Section 2.7, and for the prescale factor. Since all signals from the plastic scintillator in each front telescope were prescaled indiscriminately (see Figure 15), the ratio of dead time pulses accepted into the computer to the number sent to the detectors was equal to the product of the prescale factor and the usual dead times in the electronics and the computer. The ratio of the appropriate scaler sums (see Figure 15 and Table 1) provided redundancy in the determination of the prescale factor, which was the largest factor in the above-mentioned product.

Runs were taken with the empty target for each measurement; these runs were analyzed in an identical manner to the target full runs. The difference in the number of counts in the proton energy window between the target full and target empty runs, was used to calculate the target thickness, with the target empty results appropriately normalized according to the relative charge on target for the two runs. The ratio of target empty counts to target full counts ranged from 7% at 500 MeV to 20% at 200 MeV.

The target thickness N_T was calculated for each run according to the formula:

$$N_T = \frac{Y}{\frac{d\sigma}{d\Omega} \times N_P \times \Delta\Omega \times \varepsilon}, \qquad 3.1$$

where:

N_T = the number of target nuclei / cm^2,

Y = the net counts detected,

$\frac{d\sigma}{d\Omega}$ = the differential cross section in cm^2/sr,

N_P = the total number of protons on target,

$\Delta\Omega$ = the solid angle acceptance in sr, and

ε = the counter telescope efficiency (in absolute units).

The cross sections used were the average cross sections over the 0.64^0 wide acceptance window. The number of protons on target was calculated from the ion chamber integrated charge as described earlier in this section. The efficiency measurements (Figure 10 and (Ca-77)), were fitted with a fourth-order polynomial by a least squares fitting routine. This polynomial was then used to calculate the efficiency at any required proton energy.

Table 5 presents the relevant parameters leading to the values of the target thickness obtained in the four separate runs. The final target thickness ($\overline{N_T}$) was taken to be the arithmetic mean of the four individual measurements, resulting in a final target thickness of:

$$\overline{N_T} = 1.455 \times 10^{22} \text{ nuclei/cm}^2.$$

TABLE 5

Target Thickness Information

Beam Energy (MeV)	Lab. Angle (degrees)	$\frac{d\sigma}{d\Omega}$ (mb/sr)	Total Uncertainty in Cross Section (%)	Charge on Target (μcoul)	Target Thickness N_T (nuclei/cm^2)	Total Uncertainty (%)	ΔN_T†
200	13	51.3	4.4	1.760	1.466×10^{22}	5.4	
350	13.6	48.6	3.8	0.235	1.537×10^{22}	5.0	
500	13.6	51.8	3.9	1.248	1.422×10^{22}	5.1	
500	13	60.2	4.0	0.445	1.393×10^{22}	5.4	

$$\overline{N_T} = (1.455 \times 10^{22} \pm 0.063 \times 10^{22}) \text{ nuclei/cm}^2$$

† The components of this uncertainty are discussed fully in the text.

This is, in other units, 96.7 mg/cm^2 or 7.74 mm of liquid ^{4}He, assuming a bubble-free liquid. That indicates a deformation of 1.37 mm for each of the target cell windows. A subsequent measurement of the physical thickness of the target cell, performed by pressurizing the cell and measuring the cell thickness with calipers, corroborated the in-beam measurement.

Two of the four target thickness measurements were performed with polarized beam. The two runs with unpolarized beam (500 MeV, 13.6^0 and 200 MeV, 13^0) had left-right asymmetries close to zero. For the two polarized runs (350 MeV, 13.6^0 and 500 MeV, 13^0), the analyzing powers were calculated (see Section 3.4.2) and found to be in excellent agreement with the values given in (St-77), providing a consistency check against experimental biases.

The errors in the cross sections that are presented in Table 5 are the errors stated in the original paper (St-77) with one exception. That paper lists a 5% uncertainty for the ionization chamber normalization, the same value presented in this section. But, because the same ion chambers were used for both the small angle cross section measurements and the target thickness measurements, it is the relative beam currents, not the absolute currents, that enter eq. 3.1. Therefore, the uncertainty in the absolute normalization does not appear in this calculation, but will appear with the uncertainties associated with the large angle measurements (see Section 3.2). However, a 3% uncertainty in relative ion chamber gains has been allowed for (this uncertainty has also been discussed earlier in this section). This uncertainty was added in quadrature with the

other uncertainties presented by Stetz et al. (St-77) to obtain the cross section uncertainties given in Table 5. Calculations showed that a small angular uncertainty, caused by the effects of the finite beam spot size, resulted in a negligible uncertainty in the cross sections used. Other uncertainties entering into the target thickness values, besides the statistical uncertainty in the number of counts detected in each run (between 1 and 2%) are: the uncertainty in the solid angle determination (1%), the efficiency uncertainty (1% for the 200 MeV and 350 MeV runs, 2% for the 500 MeV runs), the uncertainty in doing the target empty subtraction (1%), and the uncertainty in the dead time corrections (2%). All of these were added in quadrature to yield the total uncertainty in N_T, given in the last column of Table 5.

The uncertainty $\Delta(\overline{N_T})$ in the final target thickness was taken to be the standard deviation from the arithmetic mean, yielding the value:

$$\Delta(\overline{N_T}) = 6.3 \times 10^{20} \text{ nuclei/cm}^2 = 4.3\%.$$

3.1.3 Target Bubbling Tests

In addition to the above measurements, a series of short runs was made at a range of beam currents to investigate the target bubbling question. These measurements were made at $\theta_{proton} = 144^0$ and a beam energy of 185 MeV. Six runs were taken with the beam current varied between 0.25 and 3.80 nA, within a total elapsed time of 2.75 hours. The data were analyzed in the same manner as the regular backward scattering runs. The results, plotted as the number of particles detected per unit charge as a function of beam

current incident on target are presented in Figure 26. The ordinate, referring to eq. 3.1, is proportional to the target thickness, for any particular angular setting of the counters. Also plotted in Figure 26 is the weighted mean of the six results. An examination of the results shows no statistical evidence for beam dependent target bubbling over the range of currents used. That is, the helium target thickness was independent of beam current for the present experiment.

A simple calculation verified the above result, showing that 10 nA of 200 MeV protons would lose approximately 5 milliwatts of power in an 8.0 mm liquid ^{4}He sample. This power would vapourize approximately 2×10^{-3} ml of liquid ^{4}He per second. However, this calculation did not take into account other sources of heat to the target cell.

3.1.4 The Target Thickness and Beam Movements

Another circumstance which could have led to a change in the effective target thickness was a movement of the beam at the target. Since the target windows were not flat, but were bowed, the target thickness was not uniform across the cell face. The situation is illustrated in Figure 27, a scale diagram of the target cell with a typical beam spot. It is probable that most of the foil distortions took place near the edges, and that the radius of curvature of the foils near the center of the target was very large. Thus, the target thickness would be slowly changing near the center,

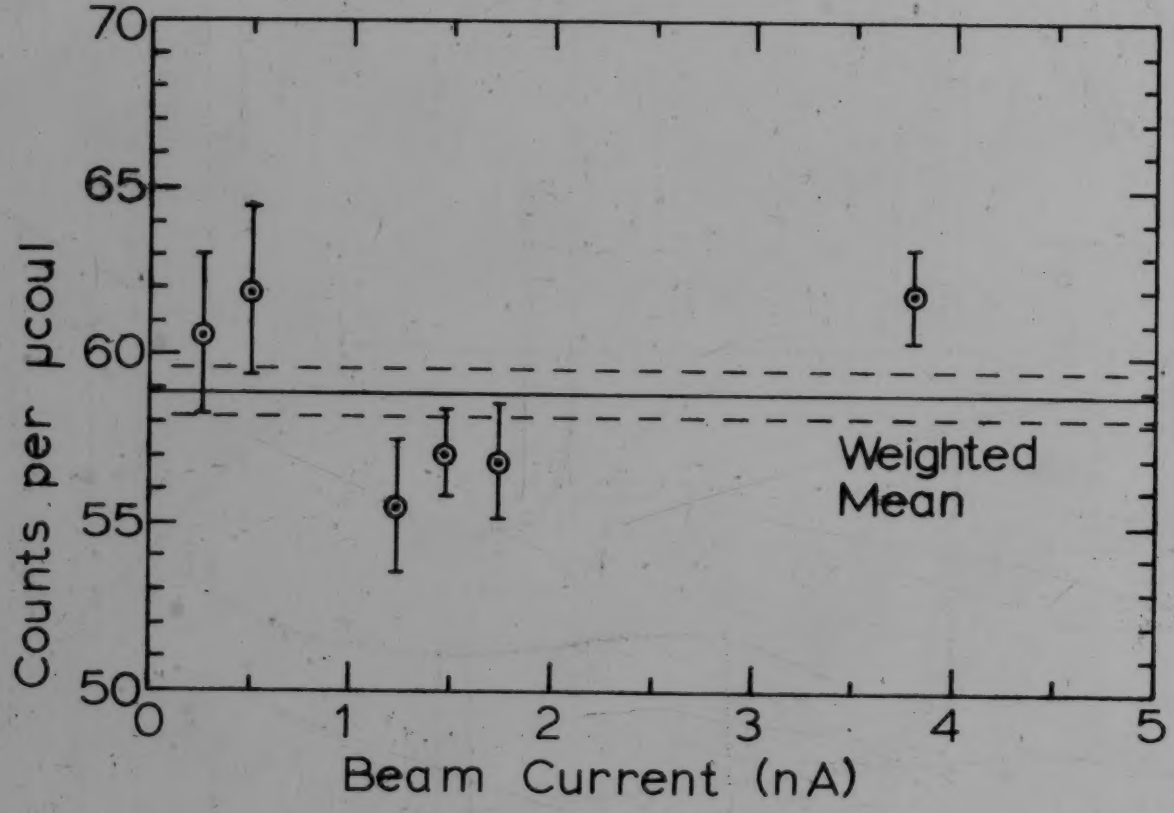

FIGURE 26. A plot of the results of the target bubbling tests as a function of the incident beam current. The error bars indicate statistical uncertainties only. The solid line is the weighted mean of the six points, with the statistical uncertainty in this value indicated by the dashed lines.

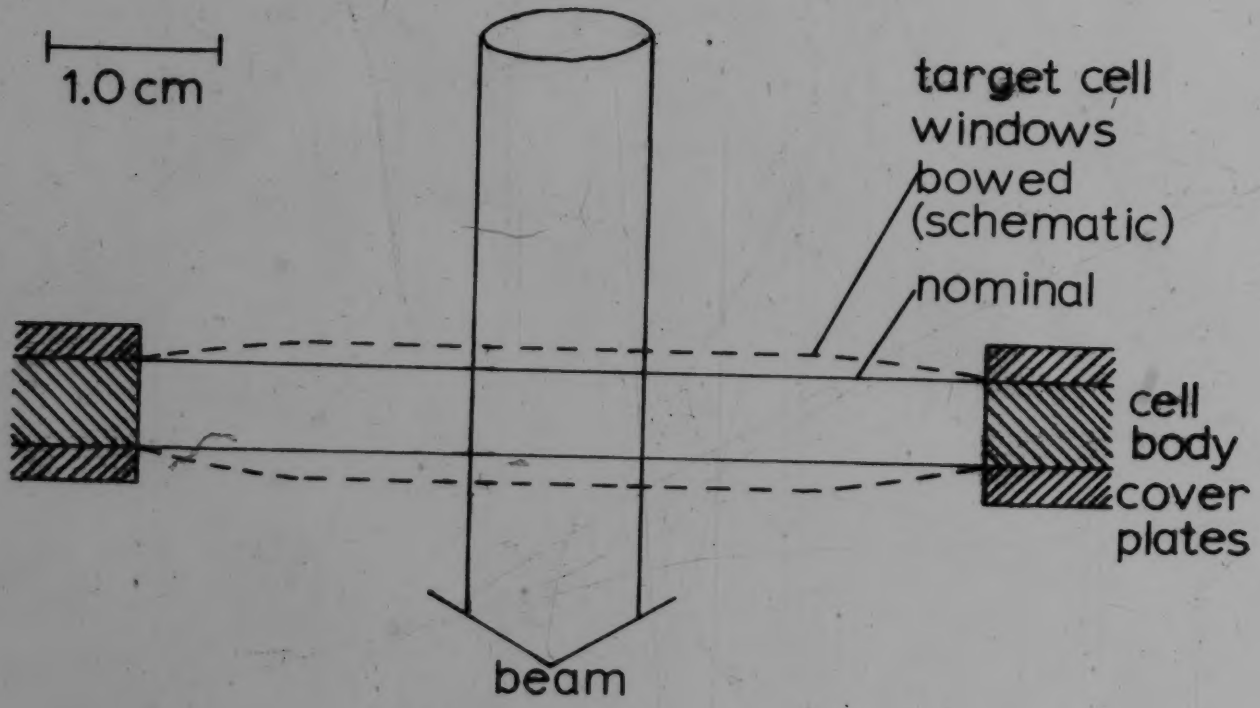

FIGURE 27. A scale diagram of a cross section of the target cell, with a typical beam spot. The shape of the bowed windows is schematic only.

and small shifts in beam position would not have led to drastic changes in target thickness.

During initial set-up of the beam at each new energy, the beam was carefully aligned using the beam profile monitors and scintillation screens described in Section 2.7 so that the beam was passing through the center of the target. One monitor, immediately after the target was frequently checked to ensure that the beam had not moved. In general, however, the beam, once established, was very position stable over many hours. Large movements of the beam, should they have occurred, would have caused excessive radiation spill further along the beam line, leading to prompt rectification. Large movements would also have initiated dramatic changes in the on-line spectra and in the detector counting rates, which would have been very obvious. These were not seen during the runs.

3.2 Data Corrections and Uncertainties

3.2.1 Data Corrections

As discussed earlier (Section 2.6), runs taken with an empty target proved that background contributions to the elastic scattering data from the target walls were negligible. Analysis of full target runs, with a time window shifted by one r.f. period, proved that random coincidences of particles were also negligible.

The efficiency of the counter telescopes for detecting, with a full energy pulse in the NaI counter, a proton of a particular in-

cident energy was determined according to the data presented in (Ca-77). The energy of the proton at the front face of the NaI counter or of the copper (if any) determined the detector efficiency, in accordance with the convention adopted in (Ca-77). This energy was calculated from the initial kinematics and proton energy losses in the materials the protons passed through between the target and the detector. These losses varied from 2 to 6 MeV, typically. The interpolation of the efficiency measurements to a particular energy utilized the method described previously (Section 3.1.2). The detection inefficiencies ranged from 4.2% to 17.4%, depending on the proton energy (see Figure 10).

The dead time corrections, discussed fully in Section 2.7, were applied to the data.

3.2.2 Data Uncertainties

Since the uncertainties associated with measurements of differential cross sections and analyzing powers are very different, the uncertainties in each type of measurement will be discussed separately.

The present measurements of differential cross sections involved uncertainties in: (1) the number of events detected, (2) the system dead time corrections, (3) the efficiency for detecting events, (4) the total proton flux incident on the target, (5) the target thickness, and (6) the solid angle determination. The statistical errors in the number of events detected are, of course,

different for each data point (see Table 6, Section 3.3). In general, however, the statistical uncertainty in each cross section was between 1 and 3%. The uncertainty in the dead time corrections, a relative uncertainty in each data point, was estimated to be not larger than 1%. An examination of the efficiency uncertainties quoted in (Ca-77) and an allowance for a possible lack of precision in the interpolation between the measured efficiencies resulted in an approximate uncertainty of 1% between cross sections at different beam energies. The accuracy of the determination of the total proton flux incident on the target was stated as ± 5% (Section 3.1.1). Approximately one half of this uncertainty may be considered an overall scale uncertainty, and one half as an uncertainty between data points at different beam energies. The precision of the target thickness measurement was previously stated to be ± 4.3% (Section 3.1.2), a contribution to the overall normalization uncertainty in the cross sections. Another contribution to the overall normalization uncertainty is the uncertainty in the solid angle determination, which was estimated to be not greater than 1%. The above uncertainties, excepting the statistical and dead time correction uncertainties, give an uncertainty between cross sections at different beam energies of 3.7%, when added in quadrature, and an overall scale uncertainty of an additional 5.7%.

A problem peculiar to the ^{4}He(p,d) data, acquired with the elastic scattering data, led to the possibility of a small beam misalignment (either lateral or rotational) for some or perhaps all of the data runs (see Appendix A for a full discussion). Such a

misalignment would change the scattering angle between the beam and the detected protons by a small amount (approximately 0.25^0). However, because measurements were made with both left and right counters and with both beam polarization directions, neither the cross sections nor the analyzing powers would be affected by this misalignment.

An important matter in the measurement of absolute cross sections is the reproducibility of the data. One illustration of the reproducibility of the data is given in the target bubbling tests, discussed in Section 3.1.3. In addition, repeated runs at the same angle and beam energy at different stages of an investigation gave statistically consistent values. For example, the cross section at $\Theta_{lab} = 144^0$ was measured 5 times during the investigation at 200 MeV, and the results were found to be completely consistent.

Uncertainties associated with the analyzing power measurements include possible errors in: (1) the measured left-right scattering asymmetry (statistical uncertainty), and (2) the value of the incident proton beam polarization (normalization uncertainty). The analyzing power experiments measured left-right scattering asymmetries with identical counter telescopes and with both beam polarization directions. Therefore, quantities such as the target thickness, proton beam flux, detector efficiencies and solid angles did not enter into the calculations, and the effects of any instrumental asymmetries were suppressed. The present methods also ensured that small uncertainties in the scattering angle due to errors in the

incident beam direction at the target would not affect the results. The measurement of separate dead times for the left and right detector combinations ensured that dead time inequalities did not result in false asymmetries.

One method of calculating the left-right scattering asymmetry ϵ_{He}, described in Section 3.4, used the formula:

$$\epsilon_{He} = \frac{N_{LU} + N_{RD} - N_{RU} - N_{LD}}{N_{LU} + N_{RD} + N_{RU} + N_{LD}}, \qquad 3.2$$

where N_{LU} is the number of particles detected by the left detector with the spin up, N_{RD} is the number of particles detected by the right detector with the spin down, etc. The derivation of eq. 3.2 assumed that the beam polarizations with spin up and spin down were of the same magnitude (see Section 3.4.2 for further discussion of this point). Then the statistical uncertainty in the asymmetry ($\Delta\epsilon$) can be represented by:

$$\Delta\epsilon = \left[\left(\frac{\partial\epsilon}{\partial N_{LU}}\right)^2(\Delta N_{LU})^2 + \left(\frac{\partial\epsilon}{\partial N_{RD}}\right)^2(\Delta N_{RD})^2 + \left(\frac{\partial\epsilon}{\partial N_{RU}}\right)^2(\Delta N_{RU})^2 + \left(\frac{\partial\epsilon}{\partial N_{LD}}\right)^2(\Delta N_{LD})^2\right]^{1/2}, \qquad 3.3$$

where $\frac{\partial\epsilon}{\partial N_{LU}}$ is the partial derivative of eq. 3.2 with respect to N_{LU}, and ΔN_{LU} is the statistical uncertainty in N_{LU} (approximated by $(N_{LU})^{1/2}$), etc.

Evaluating this equation leads to the formula:

$$\Delta\varepsilon = \left[\frac{4(N_{LU} + N_{RD})\ (N_{RU} + N_{LD})}{(N_{LU} + N_{RD} + N_{RU} + N_{LD})^3}\right]^{\frac{1}{2}} \qquad 3.4$$

The uncertainty in the value of the beam polarization involves uncertainties in the correction to the measured polarimeter asymmetry ε_{pp} due to C(p,2p) reactions in the CH_2 polarimeter target (see Section 2.4.2) and in the value of the analyzing power for p-p scattering which was used to relate the polarimeter asymmetries to the actual beam polarizations. The uncertainty in the polarimeter asymmetry caused by the carbon correction is estimated to be ± 3% at each energy (i.e., $(\Delta\varepsilon_{pp}/\varepsilon_{pp}) = 0.03$). The p-p analyzing powers P_{pp} used in this experiment, given in Table 7 in Section 3.4, were obtained from a recent phase shift analysis of all relevant p-p scattering data (Am-77). The uncertainty in these analyzing powers is approximately ± 2% at each energy (i.e., $(\Delta P_{pp}/P_{pp}) = 0.02$).

3.3 The Elastic Scattering Differential Cross Sections

Elastic scattering differential cross sections were measured at incident proton energies of 185, 200, 225, 250, 275, 300, 350, 400, 440 and 500 MeV. The 185 MeV beam was the lowest energy beam that could be extracted from the cyclotron. The energies of 440 MeV and 300 MeV were chosen to coincide with the Berger data (Be-76b) in the same angular region, so that the experiments could be directly

compared. The cross sections were measured at four or five angles between about 145^0 and 168^0 in the laboratory for each of the ten energies studied. The requirement that both front and back detector assemblies be positioned at integral degrees (see Section 2.4) determined the exact proton angles measured.

Before presenting the primary results from the experiment, some details of the method of calculating the cross section will be discussed. The data, because of the necessity for spin up, spin down, and (occasionally) spin off measurements for the studies of analyzing powers undertaken simultaneously at most beam energies, were obtained in two or more separate runs for the majority of points. A differential cross section was calculated for each run from the total number of counts obtained in both arms of the experiment. If more than one run existed at a particular angle and energy setting, these individual cross sections were combined to form a mean cross section according to the equation:

$$\frac{d\sigma}{d\Omega} = \sum_{i=1}^{n} \left(\frac{d\sigma}{d\Omega}\right)_i \times \frac{Q_i}{\left(\sum_{j=1}^{n} Q_j\right)}, \qquad 3.5$$

where Q_i is the integrated beam current on target for the i^{th} run. This is equivalent to a calculation of the mean cross section from the total yield from all appropriate runs ($\sum_{i=1}^{n} Y_i$), the total charge ($\sum_{j=1}^{n} Q_j$), and other relevant parameters. However, an advantage of the present method was that cross sections from individ-

ual runs could be examined for anomalous results. The statistical uncertainty in the cross section data presented is the uncertainty in the total number of counts obtained at that angular setting for that energy.

The $^4He(p,p)^4He$ differential cross sections are presented in Table 6, and are illustrated in Figure 28 versus cos Θ_{cm} and Θ_{cm}. The variables t and u in Table 6 are standard Mandelstam invariants. Some useful relationships between the variables t and u and center of mass system scattering parameters are given in Appendix B.

All of the cross sections were obtained using two symmetrical detector assemblies except for two points at 300 MeV, Θ_{lab} = 152^0 and 157^0, which were being measured with unpolarized beam. For the only run taken at 157^0, and for one of the two runs taken at 152^0, the back right wire chamber did not produce valid coordinates. The other back wire chamber operated normally, however, and the data from this telescope was processed in standard fashion. The individual cross sections from the two runs at 152^0, one with both arms operating, one with the single arm, were in agreement, within statistics. As a consequence of this occurance, however, these two data points have somewhat larger statistical uncertainties than do other points at this energy. Also, because of the possibility of a slight beam misalignment (see Appendix A), the cross sections at these two angles have a (proton) scattering angle uncertainty of $\pm 0.25^0$.

Referring to Figure 28 and Table 6, the most striking feature of these cross sections is the absence, in this angular region, of

TABLE 6

Elastic Scattering Cross Sections

Beam Energy (MeV)	θ_{lab} (degrees)	θ_{cm} (degrees)	$\cos\theta_{cm}$	$(\frac{d\sigma}{d\Omega})_{lab}$ (μb/sr)	$(\frac{d\sigma}{d\Omega})_{cm}$ (μb/sr)	Statistical Uncertainty (%)	$-t$ $(GeV/c)^2$	u $(GeV/c)^2$	$\frac{d\sigma\dagger}{dt}$ $(\mu b/(GeV/c)^2)$
185	152	159.4	-0.936	2.22	3.93	0.9	0.886	7.286	54.0
	158	163.9	- .961	2.29	4.17	0.9	.900	7.297	57.2
	163	167.6	- .977	2.23	4.13	0.9	.905	7.305	56.7
	168	171.3	- .988	2.04	3.82	0.9	.910	7.310	52.4
200	144	153.4	- .894	1.66	2.83	0.7	.938	7.227	35.8
	152	159.5	- .937	1.76	3.13	1.0	.961	7.248	39.6
	158	163.9	- .961	1.70	3.10	1.4	.973	7.261	39.2
	163	167.6	- .977	1.64	3.05	1.4	.981	7.269	38.6
	168	171.3	- .988	1.52	2.86	1.4	.987	7.274	36.2
225	144	153.5	- .895	1.36	2.34	1.1	1.062	7.163	26.2
	152	159.5	- .937	1.30	2.33	1.4	1.085	7.187	26.2
	158	164.0	- .961	1.27	2.33	1.5	1.099	7.200	26.2
	163	167.7	- .977	1.24	2.32	1.6	1.108	7.209	26.1
	168	171.3	- .988	1.18	2.23	1.4	1.114	7.216	25.1
250	144	153.6	- .896	1.01	1.74	1.7	1.185	7.100	17.5
	152	159.6	- .937	1.01	1.82	1.9	1.211	7.126	18.3
	158	164.1	- .962	0.967	1.79	2.1	1.226	7.141	18.0
	163	167.7	- .977	.949	1.79	1.7	1.236	7.151	18.0
	168	171.4	- .989	.929	1.78	2.3	1.243	7.158	17.9

TABLE 6 (continued)

Beam Energy (MeV)	θ_{lab} (degrees)	θ_{cm} (degrees)	$\cos\theta_{cm}$	$(\frac{d\sigma}{d\Omega})_{lab}$ (μb/sr)	$(\frac{d\sigma}{d\Omega})_{cm}$ (μb/sr)	Statistical Uncertainty (%)	$-t$ $(GeV/c)^2$	u $(GeV/c)^2$	$\frac{d\sigma}{dt}$ $(\mu b/(GeV/c)^2)$
275	144	153.7	-0.896	0.894	1.55	2.0	1.309	7.038	14.1
	152	159.7	- .938	.814	1.48	2.4	1.338	7.066	13.5
	158	164.1	- .962	.759	1.42	1.8	1.354	7.083	12.9
	163	167.8	- .977	.763	1.45	1.6	1.365	7.093	13.2
	168	171.4	- .989	.723	1.39	2.7	1.373	7.101	12.7
300	146	155.3	- .908	.671	1.19	2.9	1.443	6.985	9.88
	152	159.8	- .938	.625	1.15	3.2	1.465	7.007	9.52
	157	163.5	- .959	.596	1.12	5.0	1.480	7.023	9.29
	163	167.8	- .977	.558	1.07	3.8	1.495	7.037	8.90
	168	171.4	- .989	.586	1.14	2.9	1.503	7.046	9.46
350	146	155.5	- .910	.434	0.780	2.3	1.696	6.866	5.52
	152	159.9	- .939	.391	.727	2.2	1.723	6.892	5.14
	157	163.6	- .959	.358	.682	2.3	1.740	6.910	4.82
	163	167.9	- .978	.351	.683	2.1	1.757	6.926	4.83
	168	171.5	- .989	.317	.625	2.5	1.767	6.936	4.42
400	152	160.1	- .940	.290	.547	2.4	1.984	6.780	3.36
	157	163.7	- .960	.267	.516	2.6	2.004	6.800	3.17
	162	167.3	- .976	.251	.493	2.7	2.020	6.816	3.03
	168	171.6	- .989	.230	.461	2.9	2.034	6.830	2.83

TABLE 6 (continued)

Beam Energy (MeV)	θ_{lab} (degrees)	θ_{cm} (degrees)	$\cos\theta_{cm}$	$(\frac{d\sigma}{d\Omega})_{lab}$ (μb/sr)	$(\frac{d\sigma}{d\Omega})_{cm}$ (μb/sr)	Statistical Uncertainty (%)	-t $(GeV/c)^2$	u $(GeV/c)^2$	$\frac{d\sigma\dagger}{dt}$ $[\mu b/(GeV/c)^2]$
440	145	155.1	-0.907	0.237	0.434	3.9	2.156	6.654	2.41
	154	161.6	- .949	.201	.387	2.9	2.204	6.702	2.15
	162	167.4	- .976	.190	.379	3.0	2.234	6.733	2.10
	168	171.6	- .989	.157	.318	3.8	2.249	6.748	1.77
500	145	155.3	- .908	.166	.309	2.2	2.471	6.523	1.50
	151	159.6	- .937	.157	.303	2.6	2.509	6.560	1.47
	154	161.8	- .950	.148	.289	2.7	2.525	6.577	1.40
	160	166.1	- .971	.146	.294	2.7	2.552	6.603	1.42
	168	171.7	- .990	.117	.242	2.9	2.577	6.628	1.17

$\dagger \frac{d\sigma}{dt} \equiv \frac{d\sigma}{du}$

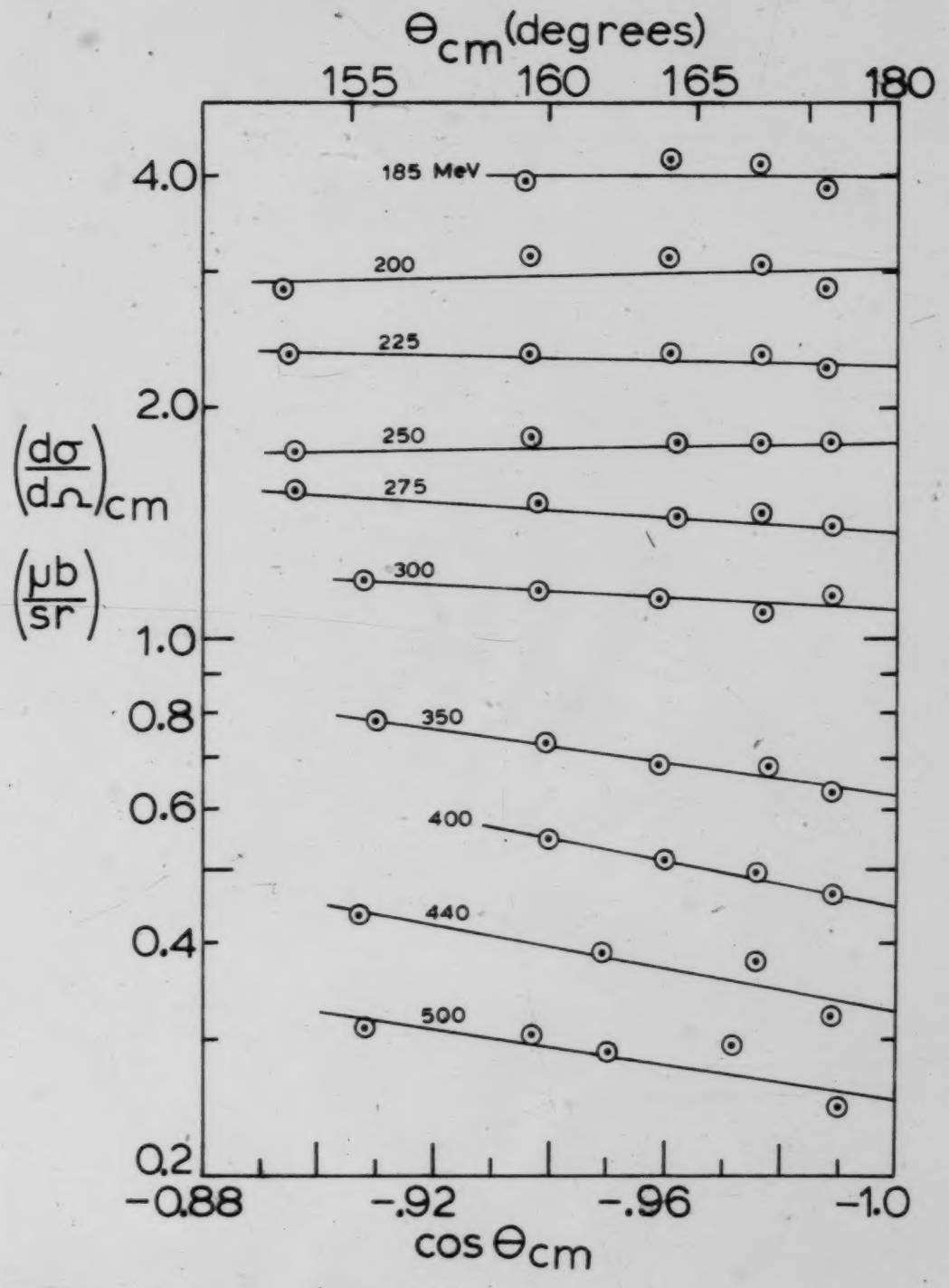

FIGURE 28. The elastic scattering differential cross sections as functions of cos θ_{cm} and θ_{cm}. The lines represent an exponential fit to the data as a function of cos θ_{cm}.

the marked backward peaking that has been observed at both lower and higher energies. The cross sections at 500 MeV decrease slightly towards $\cos \theta_{cm} = -1.0$. The slope of the angular distributions becomes more negative from 500 to 440 to 400 MeV. Then this slope becomes less negative until, at 300 and 275 MeV, the cross sections decrease very slightly towards $\cos \theta_{cm} = -1.0$. The cross sections are approximately constant at 250 and 225 MeV. At 200 and 185 MeV, the angular distributions exhibit weak backward peaking at the forward angles, which changes to decreasing cross sections at the most backward angles. It should be recalled, at this point, that a primary motivation for this investigation with small increments in the incident beam energy was the search for the presence of structure, in particular, a sharp minimum which might occur near 240 MeV (Le-76); this structure would extend over the entire angular range covered by the present experiment. There is no indication of such structure in the data, but a clear pattern of a change in the shape of the angular distribution at approximately the energy predicted for the minimum does emerge.

In order to display the energy dependence of the cross sections, the angular distributions were extrapolated to $\cos \theta_{cm} = -1.0$. The data were fitted with an exponential function of $\cos \theta_{cm}$ which was then used to calculate the 180^0 cross section; these functions are shown in Figure 28. The 180^0 cross sections obtained in this manner, together with similarly extrapolated values

from experiments at other energies (49 MeV - Da-67; 85 MeV - Vo-74; 100 MeV - Go-70; 147 MeV - Co-59; 156 MeV - Co-75; 298, 438, 648, and 840 MeV - Be-76b) are illustrated in Figure 29. Any extrapolation procedure has inherent uncertainties, especially for experiments that do not extend as far backward as the present experiment. However, even large differences in extrapolations on the scale of Figure 28 leave the trends in the excitation function of Figure 29 unchanged.

The predicted minimum in the 180^0 cross section is not present between 185 MeV and 300 MeV. However, the cross section at 180^0 as a function of proton energy exhibits double exponential behavior. There is a rapid decrease from low energies to about 200 MeV in nearly exponential fashion. Beyond 200 MeV, the cross section again appears to decrease exponentially with energy, but with a much smaller slope than previously. This change occurs very near the energy where the angular distributions change character.

Another trend in the experimental data evident in Figure 29 is that the Berger data (Be-76b) are consistently larger than the values of the extrapolated cross sections obtained in the present measurement, although the measurements do agree within stated absolute errors. In addition to their statistical uncertainties, which ranged from 6% to greater than 15%, Berger et al. (Be-76b) assigned a 10% normalization uncertainty to their data.

Further comparisons of the data from the present experiment and other experiments in the same energy region are shown in Figure 30. The present data at 185, 300 and 440 MeV, the Berger data at

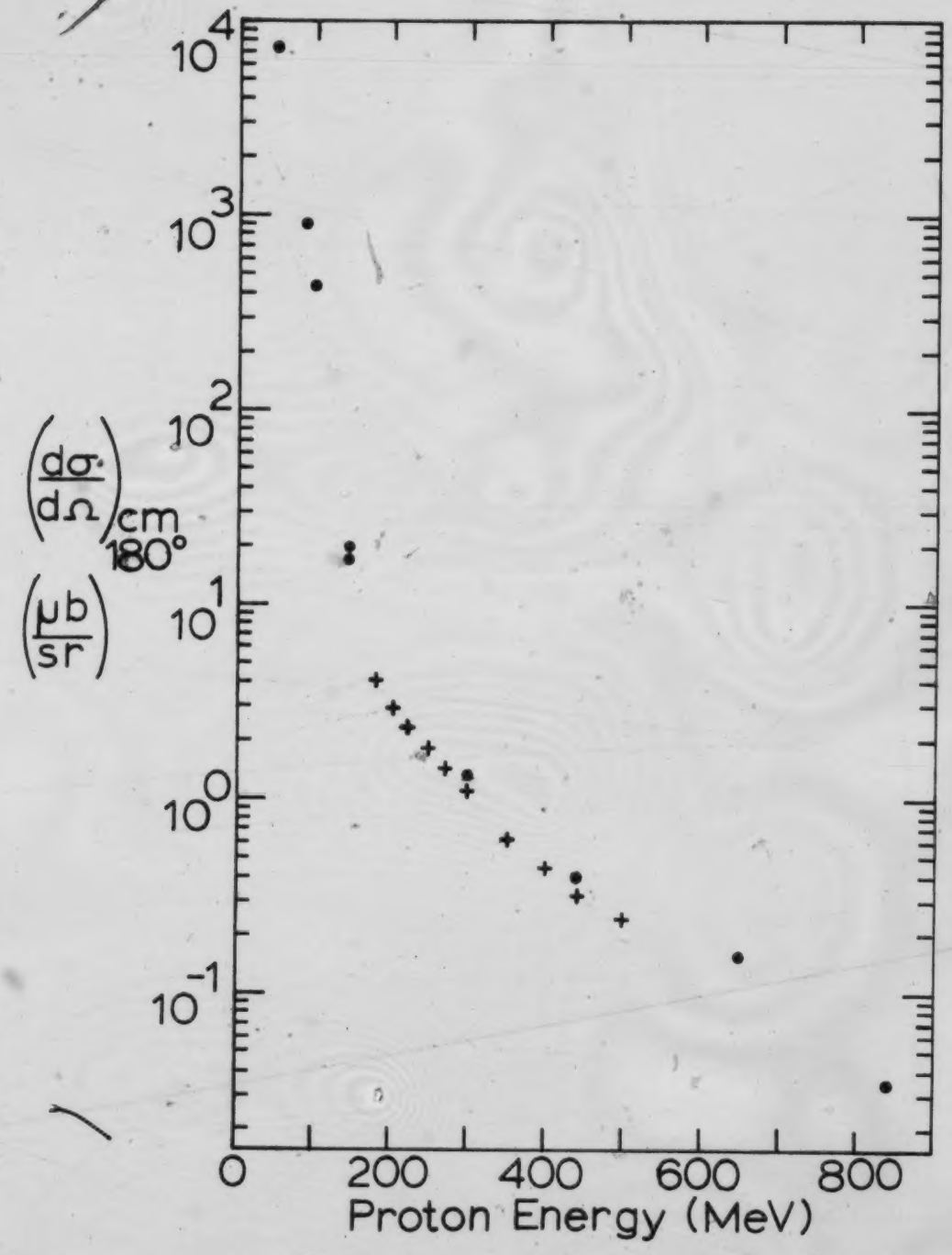

FIGURE 29. The elastic scattering cross sections extrapolated to 180^0, as a function of proton energy. The pluses are the present data, the circles are data from previous experiments (see text for references).

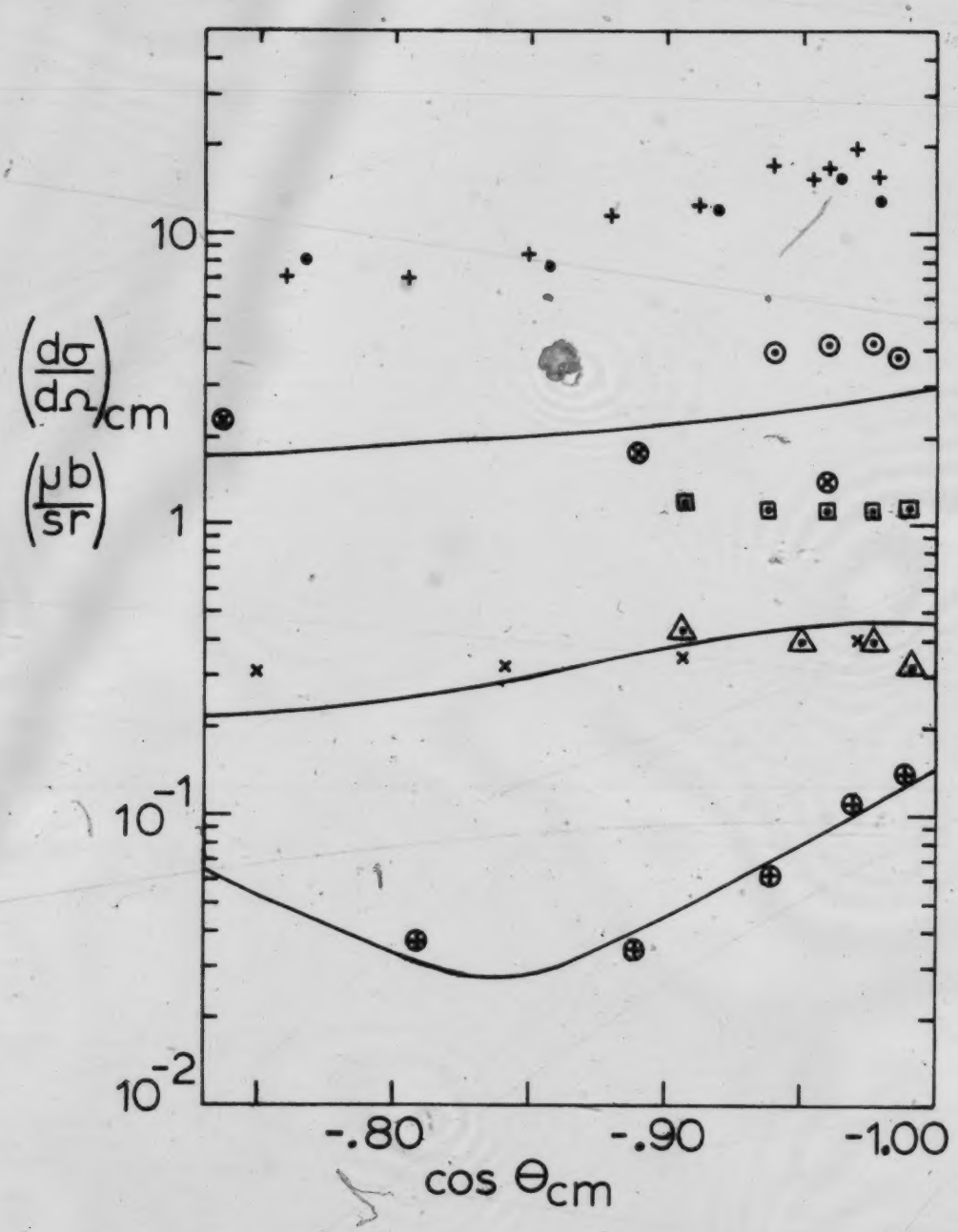

FIGURE 30. The elastic scattering differential cross sections vs. cos θ_{cm}, for the following energies: ⊙: 185 MeV, present data; ⊡: 300 MeV, present data; ▲: 440 MeV, present data; ●: 147 MeV, (Co-59); +: 156 MeV, (Co-75); ⊗: 298 MeV, (Be-76b); x: 438 MeV, (Be-76b); ⊕: 648 MeV, (Be-76b). The curves are triton exchange model calculations (Le-76) at 298, 438 and 648 MeV.

298, 438 and 648 MeV (Be-76b), the 156 MeV data from Comparat et al. (Co-75), and the 147 MeV data of Cormack et al. (Co-59) are presented. The solid lines shown in Figure 30 are the triton exchange model calculations of Lesniak et al. (Le-76) compared to the data of Berger, which will be discussed in Chapter IV. The present results are in substantial agreement with the Berger data at 440 MeV, while the Berger results are larger than the present results at 300 MeV by approximately 25%. The 156 MeV and 147 MeV data, which are very similar, illustrate the fact, evident in Figure 29, that the magnitude of the cross section below 185 MeV increases rapidly. The shape of the 156 MeV data is similar to the data at 185 MeV. In particular, very slight evidence (one data point) is seen in both the 147 MeV and 156 MeV data for a decreasing cross section for $|\cos \theta_{cm}| > 0.95$, as is observed near 200 MeV in the present experimental data.

Another interesting feature is the strong backward peaking reported at 648 MeV, which seems to be still stronger and narrower at 840 MeV. In the present data at 400 MeV and 440 MeV, the angular distributions decrease with increasing angle. At 500 MeV, the cross sections are still decreasing with angle, but not as rapidly. This may be the first evidence for the onset of the backward peak.

3.4 The Elastic Scattering Analyzing Powers

3.4.1 The Beam Polarization Calibration

The quantity which was actually determined in the present

measurement of the $^4He(p,p)^4He$ analyzing power P_{He} was the left-right scattering asymmetry ε_{He}. This is related to the analyzing power by:

$$\varepsilon_{He} = P_{He} P_B , \qquad 3.6$$

where P_B is the absolute polarization of the beam. Thus, an accurate determination of P_{He} depends not only on a precise measurement of ε_{He}, but also upon an accurate knowledge of the incident beam polarization.

The beam polarization was monitored by a polarimeter (described in Section 2.4), utilizing elastic proton-proton scattering as the calibrating reaction. This polarimeter measured the left-right scattering asymmetry ε_{pp}, given by:

$$\varepsilon_{pp} = P_{pp} P_B , \qquad 3.7$$

where P_{pp} is the analyzing power for p-p scattering at the polarimeter angle, $\Theta_{lab} = 17^0$. The measured polarimeter asymmetry was corrected for the effects of the carbon in the CH_2 target to obtain ε_{pp}. Calculations showed that p-p inelastic reactions (pion production) would not have produced significant effects in the polarimeter. The p-p analyzing powers used for the determination of the beam polarizations are given in Table 7. These analyzing powers were obtained from the recent phase shift analysis of the BASQUE group at TRIUMF (Am-77).

TABLE 7

Polarimeter Analyzing Powers

Proton Energy (MeV)	Proton-Proton Analyzing Powers*†
185	+0.291
200	.311
225	.341
250	.367
350	.436
400	.459
500	.506

*For $\theta_{lab} = 17^0$.

†From Am-77. The uncertainty in these analyzing powers is approximately $(\Delta P_{pp}/P_{pp}) = \pm 0.02$.

3.4.2 Calculation of the Analyzing Powers

For each measurement of the analyzing power, at least one run was made with the beam polarization (spin) up and one run with spin down. A limited number of measurements were made with spin off to investigate instrumental asymmetries. These were found, in general, to be ≤ 0.03.

The primary method of calculating the scattering asymmetry ε_{He} made use of the formula:

$$\varepsilon_{He} = \frac{N_{LU} + N_{RD} - N_{RU} - N_{LD}}{N_{LU} + N_{RD} + N_{RU} + N_{LD}}, \qquad 3.2$$

with the symbols previously defined in Section 3.2. Incorporating measurements taken with both polarization directions and both left and right detectors in this manner eliminated the need to use such factors as detector efficiencies and solid angles, and suppressed the effects of instrumental asymmetries.

This formula is an extension of the expression:

$$\varepsilon = \frac{N_L - N_R}{N_L + N_R}, \qquad 3.8$$

which is used with two detectors, but with one spin orientation.

In general, the spin up and spin down runs did not have beam polarization of the same magnitude, nor were the two runs of equal duration. The beam polarization was, therefore, taken as the mean of the polarizations for the two separate runs, weighted by the integrated beam current, and was calculated from:

$$\overline{P_B} = \frac{|P_U|Q_U + |P_D|Q_D}{Q_U + Q_D} , \qquad 3.9$$

where $Q_U(Q_D)$ is the integrated beam current on target for the spin up (down) run, having beam polarization $P_U(P_D)$. The helium analyzing powers were then calculated according to eq. 3.6 and 3.7.

In order to verify the above calculations, the helium analyzing powers were calculated by a second, completely independent method. This secondary method calculated an asymmetry ε_{He} for each run, including spin off runs, according to eq. 3.8. Similarly calculated for each run was the polarimeter left-right asymmetry ε_{pp}. Then a graph was plotted of ε_{He} vs. ε_{pp} and a best straight line was fitted to all of the points on the graph, with a statistical weighting factor. The slope of this straight line, 'B', is given by the relationship:

$$B = \frac{\varepsilon_{He}}{\varepsilon_{pp}} = \frac{P_{He}P_B}{P_{pp}P_B} = \frac{P_{He}}{P_{pp}} , \qquad 3.10$$

that is, the slope is the ratio of the mean scattering asymmetries from the helium and polarimeter targets, or equally, the ratio of the respective analyzing powers. The helium analyzing power was calculated with the aid of this equation.

3.4.3 The Elastic Scattering Analyzing Powers

The elastic scattering analyzing powers calculated by both methods are presented in Table 8. As can be seen upon examination of the results, the analyzing powers calculated by the two methods are in close agreement. The largest difference between the two methods is 0.012, and the average difference between the two values is 0.0032. Another important fact to note is that the sign of the difference appears to be randomly distributed, i.e., one method is neither consistently larger nor smaller than the other. However, the analyzing powers calculated by the primary method, i.e., using eq. 3.2, are the values which will be discussed below.

The analyzing powers are shown in Figure 31 (a to g) as a function of laboratory scattering angle for each of the seven energies measured. The error bars shown correspond to the statistical uncertainties. The statistical uncertainties in the data points are quite small at the lower energies, but become larger as the energy rises and the differential cross sections decrease.

The data at 500 MeV, 400 MeV, 350 MeV and 250 MeV show a similar angular dependence. The analyzing powers decrease from 145^0 to about 160^0 then increase very rapidly. The analyzing power reaches a minimum at 400 MeV, where the value at the peak is below -84%, and decreases rapidly in magnitude at both higher and lower

TABLE 8

Elastic Scattering Analyzing Powers

Beam Energy (MeV)	θ_{lab} (degrees)	Analyzing Power		Statistical Uncertainty
		Primary Calculation	Secondary Calculation	
185	152	-0.339	-0.337	0.013
	158	- .309	- .308	.013
	163	- .279	- .279	.013
	168	- .231	- .230	.014
200	144	- .416	- .418	.017
	152	- .393	- .392	.014
	158	- .382	- .382	.020
	163	- .366	- .366	.020
	168	- .311	- .308	.022
225	144	- .294	- .291	.018
	152	- .428	- .420	.019
	158	- .442	- .440	.019
	163	- .431	- .439	.022
	168	- .419	- .427	.019

TABLE 8 (continued)

Beam Energy (MeV)	θ_{lab} (degrees)	Analyzing Power: Primary Calculation	Analyzing Power: Secondary Calculation	Analyzing Power: Statistical Uncertainty
250	144	-0.284	-0.290	0.023
	152	- .430	- .429	.025
	158	- .495	- .500	.029
	163	- .533	- .534	.027
	168	- .397	- .397	.039
350	146	- .695	- .693	.029
	152	- .744	- .745	.028
	157	- .791	- .792	.028
	163	- .763	- .768	.030
	168	- .547	- .546	.032
400	152	- .789	- .787	.030
	157	- .843	- .844	.030
	162	- .730	- .730	.035
	168	- .681	- .681	.037
500	145	- .531	- .528	.024
	151	- .580	- .591	.036
	154	- .625	- .636	.034
	160	- .695	- .683	.046
	165	- .578	- .577	.035
	168	- .482	- .475	.047

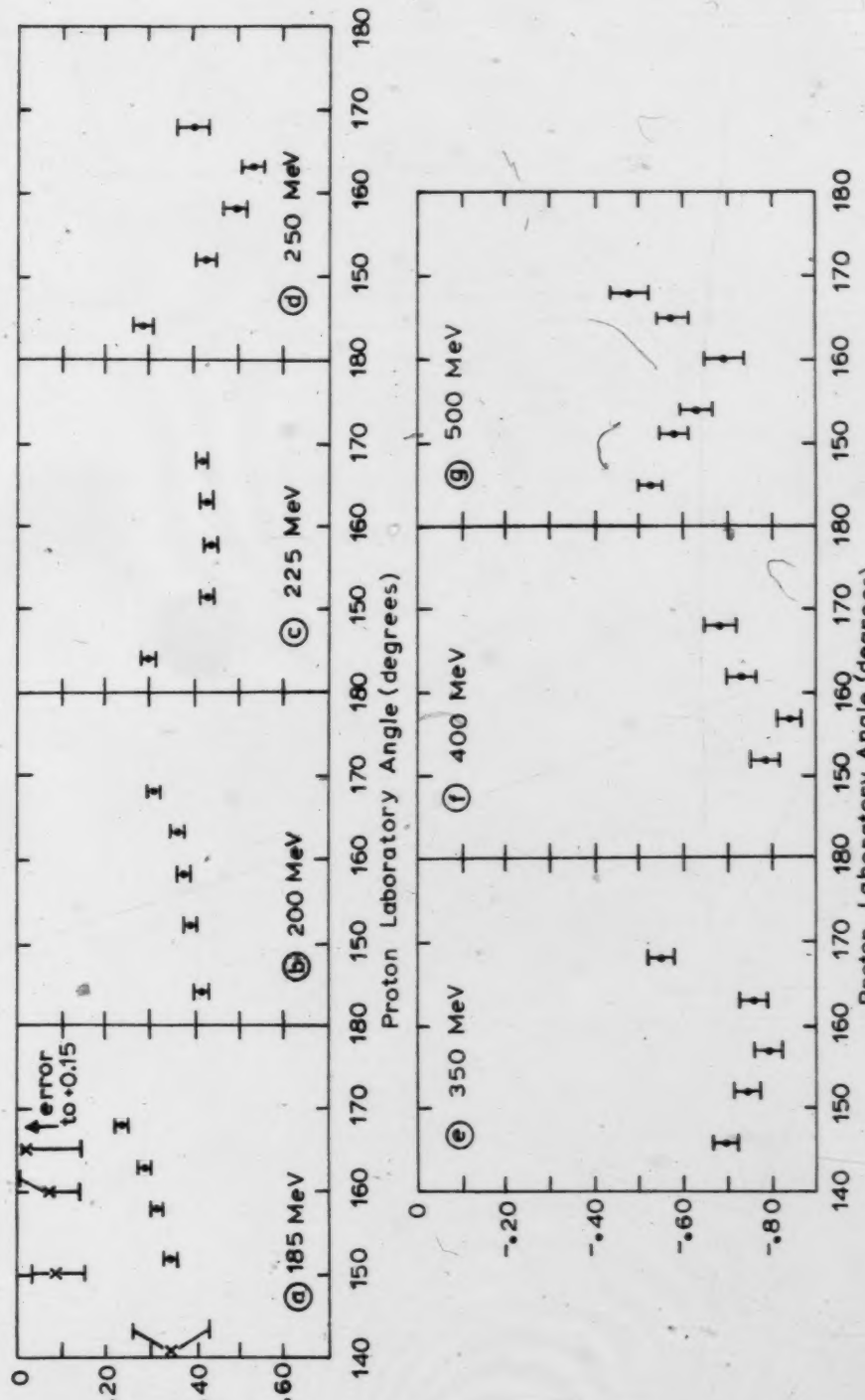

FIGURE 31. The elastic scattering analyzing powers as a function of θlab, shown separately for each beam energy. The uncertainties shown are the statistical uncertainties only. The data indicated by crosses in (a) are from (Co-59) at 147 MeV.

energies. At 225 MeV, the sharp dip that was evident at higher energies is not observed, although the magnitude is similar to the 250 MeV data. The 200 MeV and 185 MeV data are not peaked at all in this angular region. The analyzing powers at these two energies have their largest magnitude at the most forward angle measured, and this magnitude drops as the scattering angle increases. The magnitude of the analyzing power at a given angle is still dropping with decreasing energy. An important feature of this change in character is that it occurs at the same energy where the cross section angular distributions show some evidence of change. This may indicate a change in the reaction mechanism.

Also shown in Figure 31 (a) is the data in this angular region from the only other analyzing power measurements near the present energies (Co-59). The data at 147 MeV are seen to be in qualitative agreement, taking into consideration the energy difference between the experiments and the uncertainties of the 147 MeV data. The trend seen from 225 MeV to 185 MeV of an analyzing power which decreases in magnitude is seen to continue to 147 MeV.

A useful method of illustrating the trends in the analyzing powers with angle and energy utilizes a contour plot, shown in Figure 32. The angular coverage of the present experimental data and that of Cormack et al. (Co-59) are shown in the diagram. The drawing of the contours is inherently uncertain; wherever these uncertainties become excessive, the contours are dotted. The dip of $< -80\%$ near 400 MeV stands out clearly, surrounded by generally well-defined contours to -50%. Below 300 MeV (where analyzing power measure-

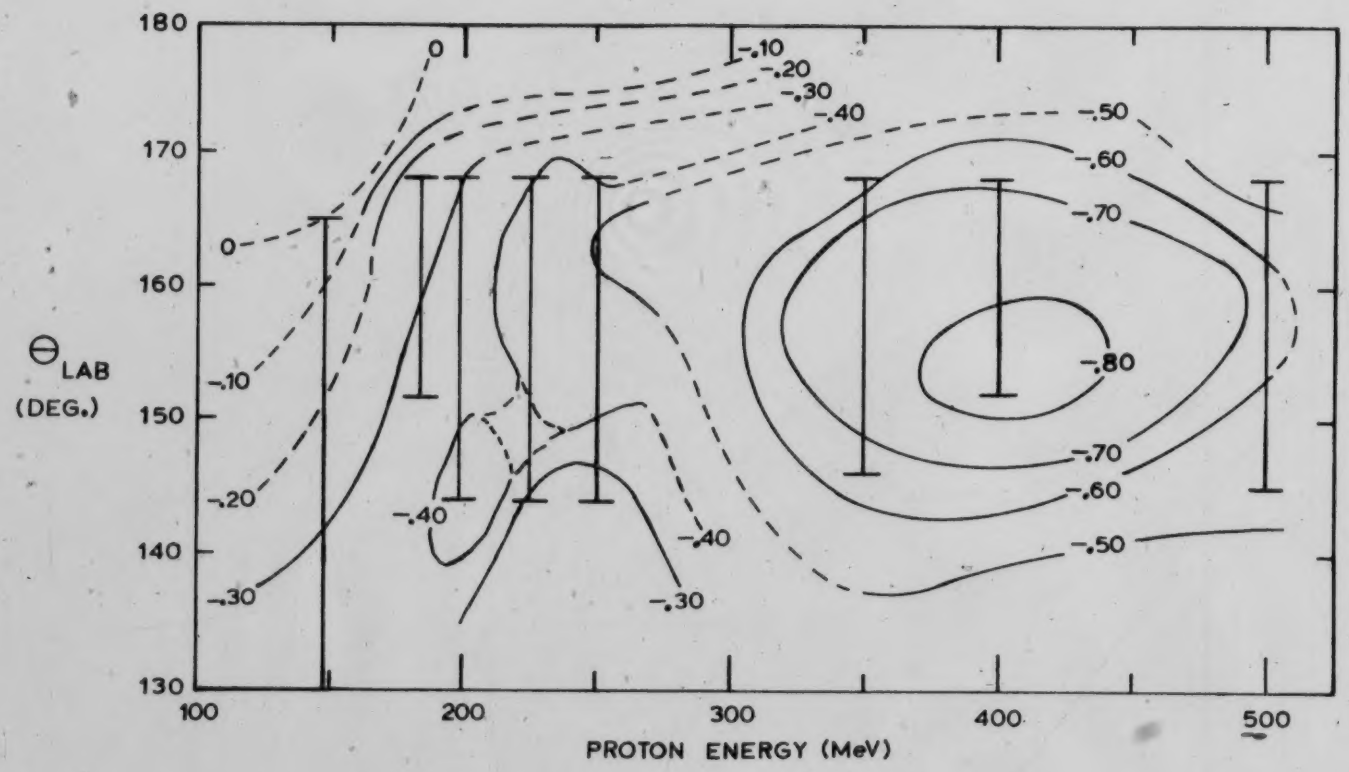

FIGURE 32. A contour plot of the elastic scattering analyzing powers as functions of θ_{lab} and proton energy. The straight lines indicate the range of the measurements at each energy.

ments would clarify the details of the polarization contours between 250 and 350 MeV), the contours take on a much more complex behaviour than that evident at higher energies. The isolated - 40% contour is not well established, but cannot be eliminated by the present data. The positive analyzing powers near $\theta_{cm} = 170^0$ and 150 MeV are suggested by the trends of the 147 MeV data, but have not been verified experimentally.

CHAPTER IV

THEORETICAL INTERPRETATIONS

The study of large angle proton elastic scattering from light nuclei, which has recently intensified (Vi-70, Al-72, Ko-73a, Du-74, Be-76b, Fr-77), can contribute to many interesting problems, among these being the large momentum behaviour of nuclear wave functions, the role of nucleon isobars in scattering processes, and the importance of two-step processes. However, after much theoretical investigation of large angle p-d scattering (for example, Ke-69, Cr-69, Ba-72, Ko-73b, No-74), very few definite conclusions have emerged. It is to be hoped that the study of backward p-^{4}He and p-^{3}He scattering, for example, will aid in resolving uncertainties.

4.1 The Triton Exchange Model

One component of such an examination is the recent investigation of the triton exchange model for backward p-^{4}He scattering (Ko-71 and Le-76). The triton exchange mechanism is illustrated in Figure 33(a), and is contrasted with direct scattering of the incoming proton (Figure 33(b)). Since the momentum transfer necessary for direct scattering ($\approx 2p$, where p is the center of mass momentum of the incoming proton) is much greater than that required for triton exchange ($\approx (3/4)p$), Lesniak *et al.* (Le-76) have assumed that, at intermediate energies, the triton exchange process is more probable.

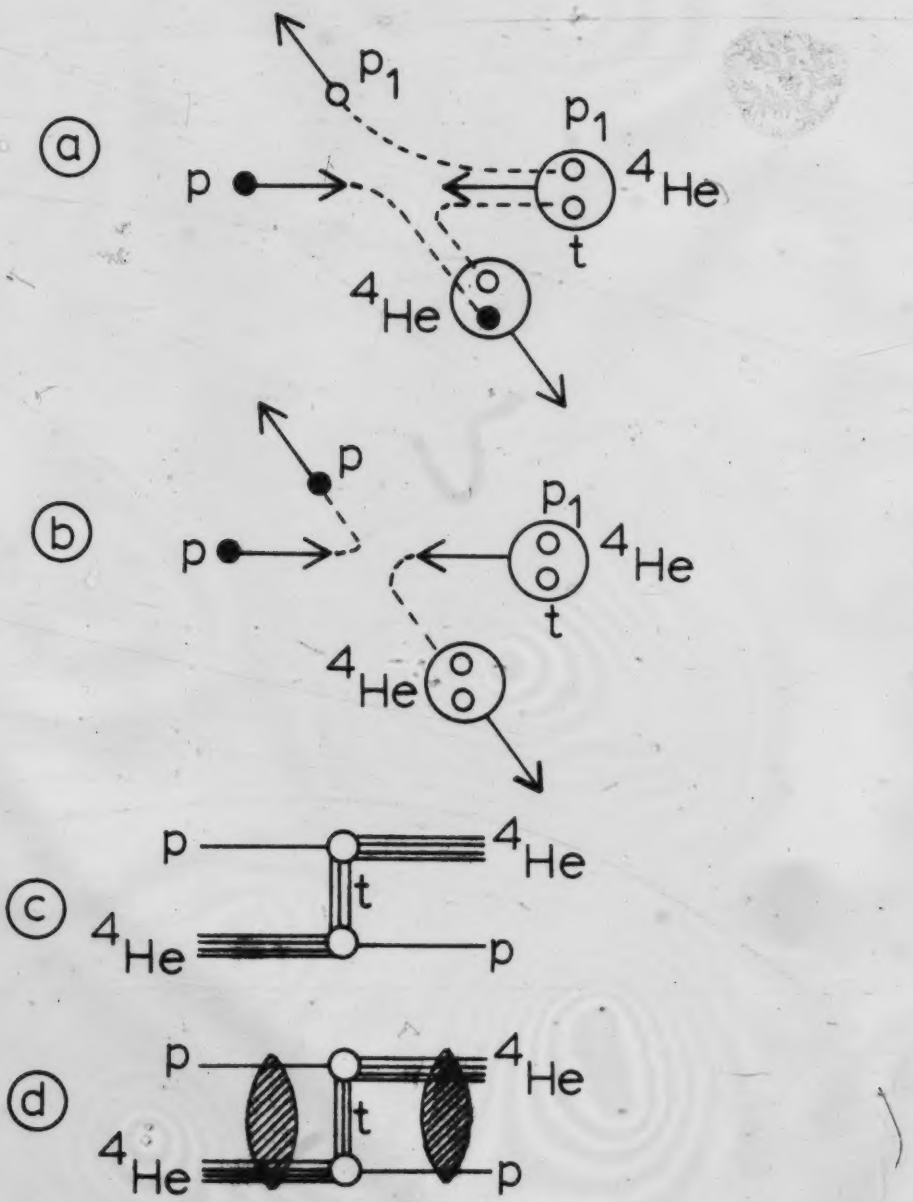

FIGURE 33. (a) A pictorial representation of the triton exchange mechanism for p-^{4}He elastic scattering. (b) A similar representation for the direct scattering mechanism. (c) The symbolic diagram for triton exchange. (d) The triton exchange diagram including absorption in both entrance and exit channels.

Their calculations included only the triton exchange mechanism (also shown in Figure 33(c)); however, they did include absorption effects for both incoming and outgoing particles (Figure 33(d)).

In the plane wave Born approximation (i.e., with no absorption effects), the differential cross section for the triton exchange process can be written (Ig-75):

$$\frac{d\sigma^{B}_{ex}}{d\Omega_{cm}} \propto (K_\alpha^2 + Q^2)^2 \; | \; \Psi_\alpha(Q) |^4 . \qquad 4.1$$

Here $K_\alpha^2 = 2\mu\varepsilon_\alpha$, with μ being the proton-triton reduced mass, ε_α being the (proton) binding energy of ^{4}He ($\simeq$19.8 MeV), and $\Psi_\alpha(Q)$ being the Fourier transform of the relative proton-triton wave function (or, the ^{4}He single particle wave function in momentum representation). As well:

$$Q = \left| \vec{p}_i - \frac{1}{4}\vec{\alpha}_f \right| = \left[\frac{9}{16}p^2 + \frac{1}{2}p^2(1 + \cos\theta_{cm}) \right]^{\frac{1}{2}}, \qquad 4.2$$

with $\vec{p}_i$ the momentum of the incoming proton, $\vec{\alpha}_f$ the momentum of the outgoing alpha particle (in the center of mass system), and p the magnitude of $\vec{p}_i$. $\Psi_\alpha(Q)$ is obtained by fitting a single particle wave function for ^{4}He to the electromagnetic form factor for ^{4}He, determined from electron elastic scattering (Fr-67).

Lesniak et al. (Le-76) used a wave function of the form:

$$\chi(r) = N \frac{1}{r} \exp(-\alpha r)\left(1 - \exp(-\beta r)\right)^n, \qquad 4.3$$

where N is a normalization constant, and α, β and n are parameters to be determined. Their resulting $|\Psi_\alpha(Q)|$ is shown as a function of Q^2 in Figure 34. The sharp dip in $\Psi_\alpha(Q)$ at $\approx$4.3 fm^{-2} originates from a minimum in the ^{4}He form factor near a four-momentum transfer squared of 10.5 fm^{-2} (Fr-67). This minimum in $|\Psi_\alpha(Q)|$ corresponds to 180^0 p-^{4}He elastic scattering at a beam energy of T_p = 242 MeV; it is this reasoning that led to the suggestion (Le-76) that a minimum might occur in the 180^0 excitation function at approximately 240 MeV. Kopeliovich and Potashnikova (Ko-71) went through a similar argument in the Born approximation with a different single particle wave function and predicted a minimum at 190 MeV.

In the calculations that Lesniak et al. (Le-76) performed to include the absorption effects, they concluded that some simplifying assumptions about the mathematical form of the absorption functions were necessary in order to make the calculations manageable. They expressed the absorptions in terms of the proton-proton elastic scattering amplitude and the proton-triton interaction potential $V_{pt}(r)$. The proton-proton scattering amplitude was parametrized as a Gaussian function of the momentum transfer, and was considered a high energy parametrization. The proton-triton interaction $V_{pt}(r)$ was also parametrized as a Gaussian function of the p-t separation 'r'. The p-t interaction parametrization was much less certain than the p-p parametrization because of the almost total lack of data on p-^{3}H elastic scattering at intermediate energies.

Other major assumptions used in their development (Le-76)

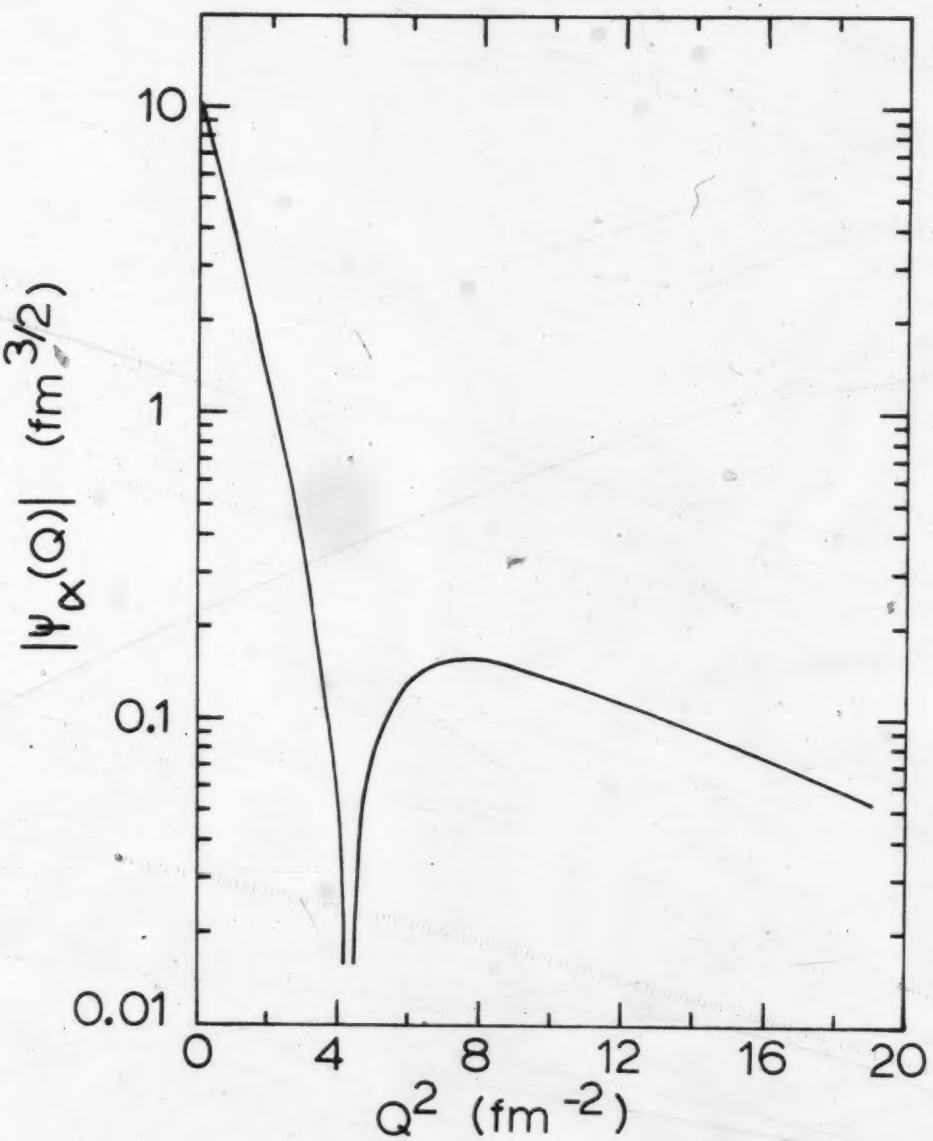

FIGURE 34. The ^{4}He single particle wave function in momentum representation as a function of Q^2.

were that all interactions were spin independent, and that the wave functions could be written in an eikonal (small angle) approximation. The eikonal trajectory was chosen along a vector:

$$\hat{p} = \frac{\vec{p}_i - \vec{p}_f}{|\vec{p}_i - \vec{p}_f|}, \qquad 4.4$$

so that the approximation should have been most accurate for $\Theta = 180^0$, becoming less accurate for more forward angles.

One significant result of these calculations was that cross sections calculated with absorption effects were one to two orders of magnitude smaller than cross sections calculated in the Born approximation at 438 and 648 MeV. Furthermore, the shapes of the angular distributions were much different for the two calculations.

The Lesniak triton exchange calculations are compared to the present data at 300 and 440 MeV and previous cross sections at 298, 438 and 648 MeV (Be-76b) in Figure 30 (Section 3.3). A comparison with the 840 MeV Berger data was not given. The theory is seen to agree at 648 MeV very well for $|\cos \Theta_{cm}| > 0.85$. Both the slope and the magnitude of the calculated cross sections are in close agreement with the data. There is less agreement at more forward angles, but this may simply be an indication that the eikonal approximation is no longer as accurate in this region. At 440 MeV, the agreement is quite good. At 300 MeV, however, the slope of the theoretical cross section is opposite to the trend of the data, and the calculated 180^0 cross section is high by almost a factor of 3.

The fact that the present experimental data show no indications of the suggested minimum near 240 MeV may be another indication that the triton exchange model is in some difficulty at these lower energies.

The differences at 300 MeV have been attributed (Le-76) to the fact that the high energy parametrization of the proton-proton scattering amplitude (and also of the proton-triton interaction) is no longer appropriate. For this reason, no definite statement on the position or the depth of the predicted minimum was made.

Another possible reason for the lack of success of the model near 300 MeV is that triton exchange may no longer be the dominant mechanism. (This is assuming that triton exchange does dominate at higher energies; other possible models will be discussed below). One of the most probable competing mechanisms at these energies is the direct scattering process (Figure 33(b)). Direct scattering could be significant at these energies, where the momentum transfer, although larger than that of triton exchange, is still much lower than that needed for direct scattering at 500-600 MeV. For example, the momentum transfers, for 180^0 scattering, at 298 and 648 MeV are 38 and 88 fm^{-2}, respectively (Le-76). This example also illustrates the difficulty of calculating the direct scattering contribution at these energies, since the ^{4}He form factor has only been measured to 20 fm^{-2} (Fr-67). Definitive calculations of the direct scattering contributions may therefore have to await the results of a measurement of the form factor for ^{4}He at higher momentum transfers,

which is currently in progress (Ar-77). If triton exchange and direct scattering are both significant in this energy region, then the interference between the two processes could also be important.

There is reason to believe that triton exchange may play a significant role in backward p-^{4}He scattering; however, this model only considers one aspect of a much broader picture. The present data indicate that a more complete theoretical description is necessary. Obvious, although admittedly difficult extensions to the present theory would be to improve the absorption approximations, to include spin dependence in the interactions, and to include direct scattering and direct scattering-triton exchange interference terms in the calculations with the present triton exchange term. An especially interesting and possibly very crucial test of a more complete triton exchange theory would be the calculation of analyzing powers to be compared with the present analyzing power measurements.

4.2 Non-Eikonal Multiple Scattering Model

It has been suggested previously that the lack of knowledge of electromagnetic form factors at large momentum transfers was an important factor why the direct scattering approach to p-^{4}He backward scattering was not pursued. However, Gurvitz, Alexander, and Rinat (Gu-76) have done essentially the inverse calculation, using large momentum transfer proton scattering cross sections to predict the form factors of light nuclei such as ^{2}H and ^{4}He.

Gurvitz *et al.* (Gu-75, Gu-75a, Gu-76) have formulated a non-

eikonal theory for multiple hadron scattering on nuclei (see Figure 35). However, in order to calculate cross sections for p-^{2}H and p-^{4}He scattering, form factors were needed at values of momentum transfer far greater than those measured. By looking at the cross section angular distributions for p-^{2}H elastic scattering at several energies, they postulated an extrapolated form factor for ^{2}H very different from those previously suggested. Using their postulated values, they found that the single scattering mechanism alone (Figure 35(a)) provided a dominant part of the p-^{2}H cross sections at large angles and high energies ($k_L \geq 1$ GeV/c). They also obtained close agreement with the data at several energies at all angles. A subsequent measurement of the ^{2}H electromagnetic form factor (Ar-75) confirmed these predictions remarkably well.

Gurvitz et al. (Gu-76) have also produced extrapolated form factors for ^{3}H, ^{3}He and ^{4}He that have not been verified experimentally. However, the use of these form factors did significantly improve their theoretical fits to the data in the higher energy regions which they studied. Until the form factors have been measured in the regions of extrapolation, they could best be tested by comparing predictions obtained with their use to all relevant data, including that presented herein. If the single scattering mechanism with the postulated ^{4}He form factor could be shown to contribute a large fraction of the backward p-^{4}He elastic scattering cross sections in the present energy range, the importance of triton exchange might be seriously questioned.

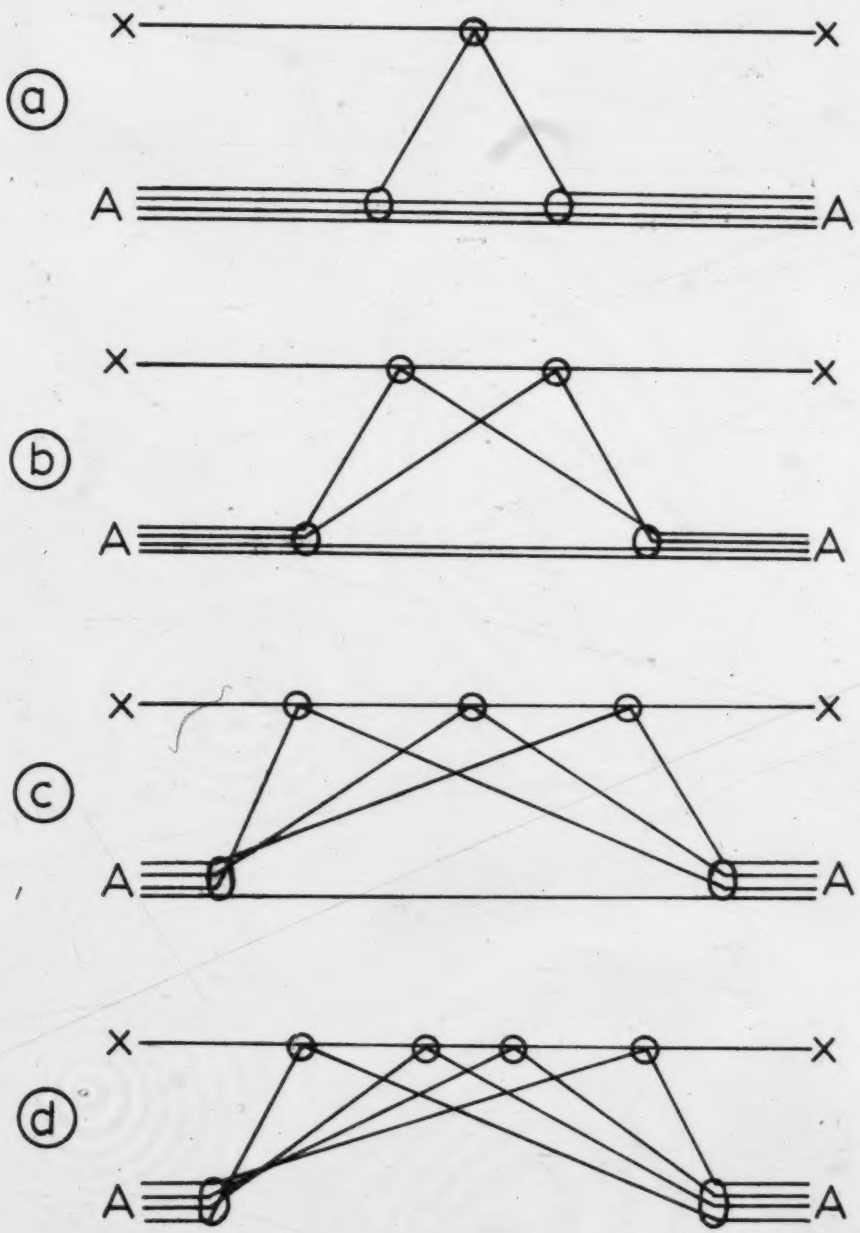

FIGURE 35. Multiple scattering diagrams for a hadron 'x' scattering from a nucleus 'A' : (a) single scattering, (b) double scattering, (c) triple scattering, and (d) quadruple scattering.

Another possible use of the extrapolated form factors would be to calculate the direct scattering terms that were discussed in Section 4.1, in connection with the triton exchange model. (The direct scattering process discussed in Section 4.1 is not identical to Gurvitz's single scattering mechanism. The former reaction includes, among several possible detailed mechanisms, the latter.)

Since the Gurvitz et al. theory (Gu-75a) incorporates several assumptions, it may not be the optimum theory with which to determine form factors in this manner. Nevertheless, the procedure of using hadron scattering to obtain nuclear form factors at high momentum transfers does illustrate a most valuable use of backward proton elastic scattering and is certainly worthy of further investigation.

It has been recently suggested (Wa-77a) that the Gurvitz et al. single scattering mechanism might explain the large, negative analyzing powers of the present experiment. If single scattering (Figure 35(a)) were the dominant mechanism in p-^{4}He backward elastic scattering, then that scattering would be related to small angle nucleon-nucleon elastic scattering at an appropriate energy. In that case, the strong, positive polarization in forward angle nucleon-nucleon scattering (Lo-70, Am-77) should be mirrored in strong, negative polarizations for p-^{4}He scattering at backward angles. A very preliminary calculation showed that large, negative analyzing powers were indeed predicted by such a theory, but that the angular distributions were not similar. More detailed calculations are in

progress in this regard.

4.3 Nucleon Isobar Models

One of the first discussions of the possible role of nucleon excited states (isobars, or N*'s) in intermediate energy scattering and reaction processes was by Kerman and Kisslinger (Ke-69). In their examination of p-d backward scattering at 1 GeV, they added the effects of the exchange of a pre-existing isobar (specifically the N*(1688 MeV)) (Figure 36(b)) to standard nucleon exchange (Figure 36(a)), and obtained a better fit to the experimental data. This model was also applied with some success to p-d scattering at 580 MeV (Vi-70). Sharma and Mitra (Sh-74) generalized the above N*-exchange model to include the effects of several isobars, and obtained reasonable agreement with experimental p-d cross sections between 365 and 1500 MeV. Thereafter, much theoretical attention has been devoted to the question of the existence of isobars in nuclei, in general, and in particular to their effect in backward elastic scattering (see, for example, Be-75, We-77, and references therein). The work in backward elastic scattering has concentrated almost exclusively on p-d scattering.

Another approach (Cr-69, Ba-72, and Ko-73b) has been to investigate the effects of a 'triangle' mechanism (Figure 36(c)) in p-d scattering. This approach utilizes the resonance effects of the $p + p \rightarrow d + \pi^+$ reaction, in which the N* (1236 MeV) may be produced in an intermediate state. One motivation behind such a theory

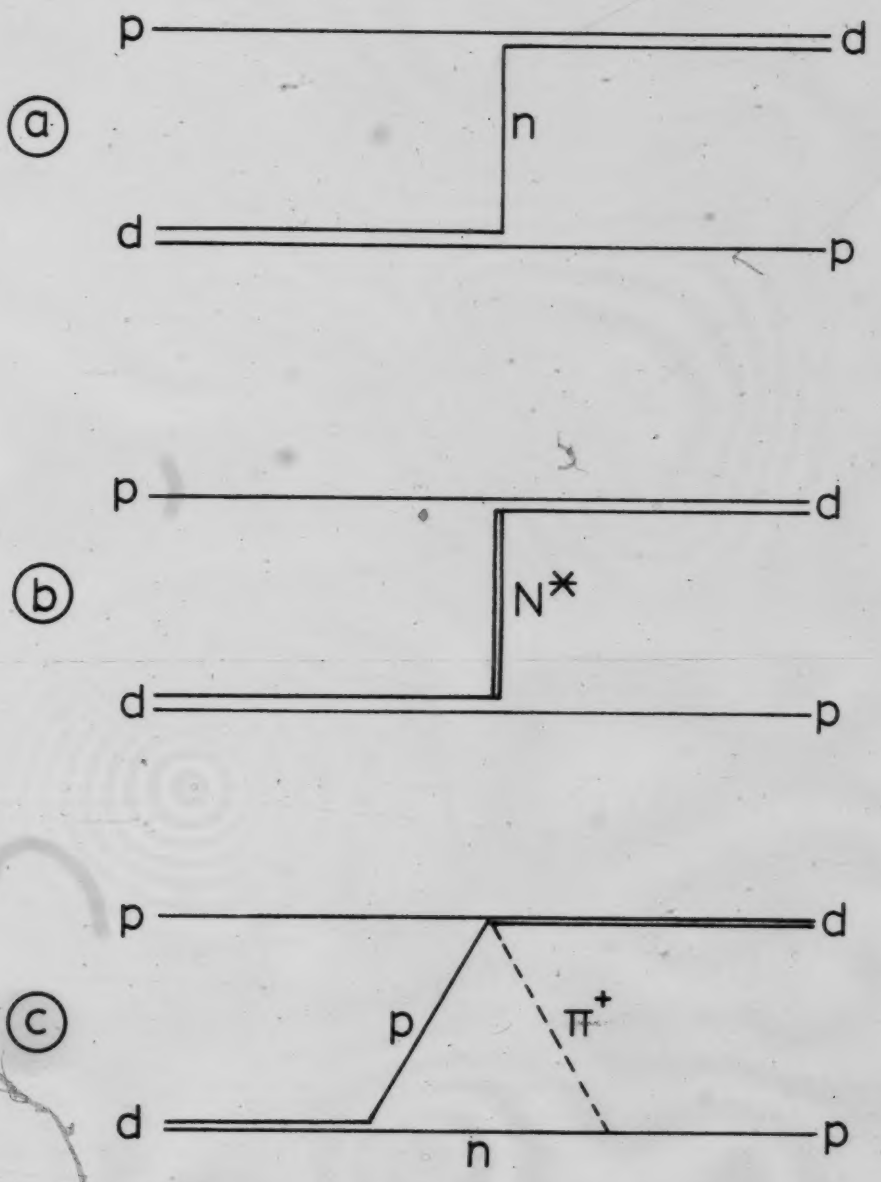

FIGURE 36. Proton-deuteron backward elastic scattering via (a) nucleon exchange, (b) nucleon isobar exchange, and (c) the 'triangle' mechanism.

is that the largest enhancement of the p-d 180^0 excitation function is near 600 MeV proton laboratory energy, which is close to the invariant mass of two nucleons plus the N*(1236 MeV). This theory has been shown (Ko-73b) to reproduce both the 600 MeV p-d cross section angular distribution (Al-72) and the shoulder in the 180^0 excitation function fairly well. A recent paper (Fr-77) has postulated that a 2N - π exchange mechanism (similar to Figure 36(c)), again with possible intermediate N* contributions, could explain some of the features of backward p-^{3}He elastic scattering. Similarly, a 3N - π exchange mechanism could be postulated as one contribution to p-^{4}He backward elastic scattering. However, since no detailed calculations have been carried out on these last two possible mechanisms, their importance relative to other proposed mechanisms is most uncertain at the present time.

All of the calculations of the above mechanisms have required several assumptions to obtain their results, and have had varying amounts of success in reproducing the experimental data. Several recent authors (No-74, Be-75, and We-77) agree that the analysis of p-d scattering in terms of isobar models is far from conclusive.

4.4 Phenomenology of the Present Cross Sections

The experimental cross sections obtained for p-^{4}He elastic scattering were presented in Figure 28 (Section 3.3) as functions of $\cos \theta_{cm}$. In that figure, the cross sections exhibited a strong dependence on the beam energy, or, equivalently, the total energy of the

system. A useful procedure is to show the cross sections as functions of an energy-dependent variable, so that kinematic factors are largely removed from the cross sections, and more important dependences may become visible. Two such plots of the present data are shown in Figures 37 and 38, where the differential cross sections in the center of mass system are plotted versus the Mandelstam variables u and -t, respectively. Some relationships between t and u and center of mass system scattering parameters are given in Appendix B.

In Figure 37, the cross sections at different energies increase rapidly with increasing u, although, in general, the points at one energy decrease with increasing u. If the cross sections were dominated by the exchange of a single particle (the triton), the cross sections should be proportional to $(u - M_T^2)^{-2}$ (Du-74), where M_T is the mass of the triton. This function is plotted in Figure 37, arbitrarily normalized at 7.3 $(GeV/c)^2$. A common dependence on this function is not observed, suggesting that triton exchange may not be a dominant part of the scattering process. However, complications caused by absorption effects, for example, could modify this plausible argument.

However, in Figure 38, the cross sections are plotted as functions of (-t), and in general, the cross sections fall with increasing (-t), both from energy to energy and at a given energy. The trend of this t-dependence is illustrated by the solid line in Figure 38, which has the functional form $(-t)^{-2.5}$. The curve is arbitrarily normalized at $-t = 1.0$ $(GeV/c)^2$. The functional de-

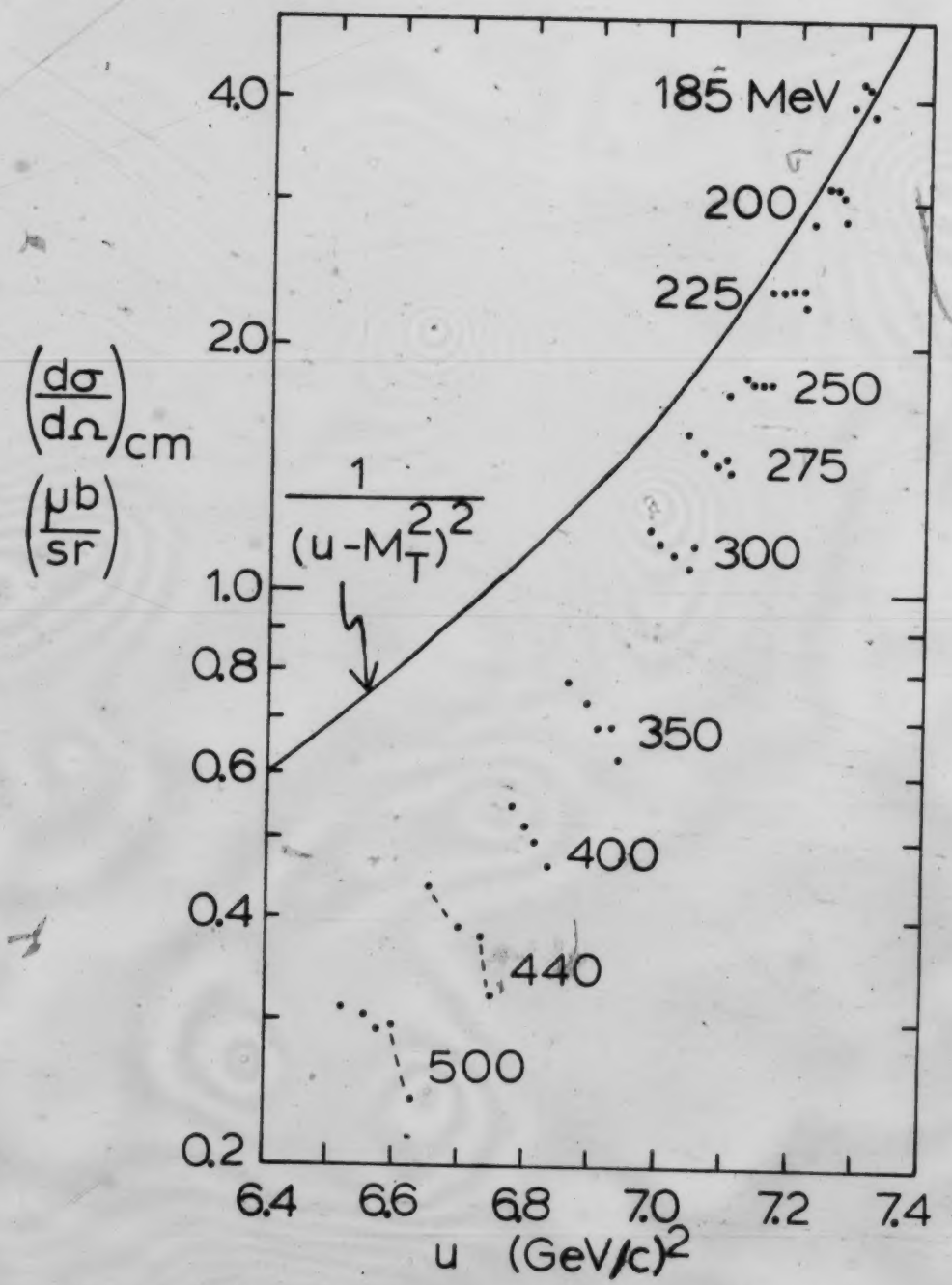

FIGURE 37. The elastic scattering differential cross sections plotted as a function of the variable 'u'. The curve is the expected u-dependence of the cross section, if the reaction is dominated by triton exchange.

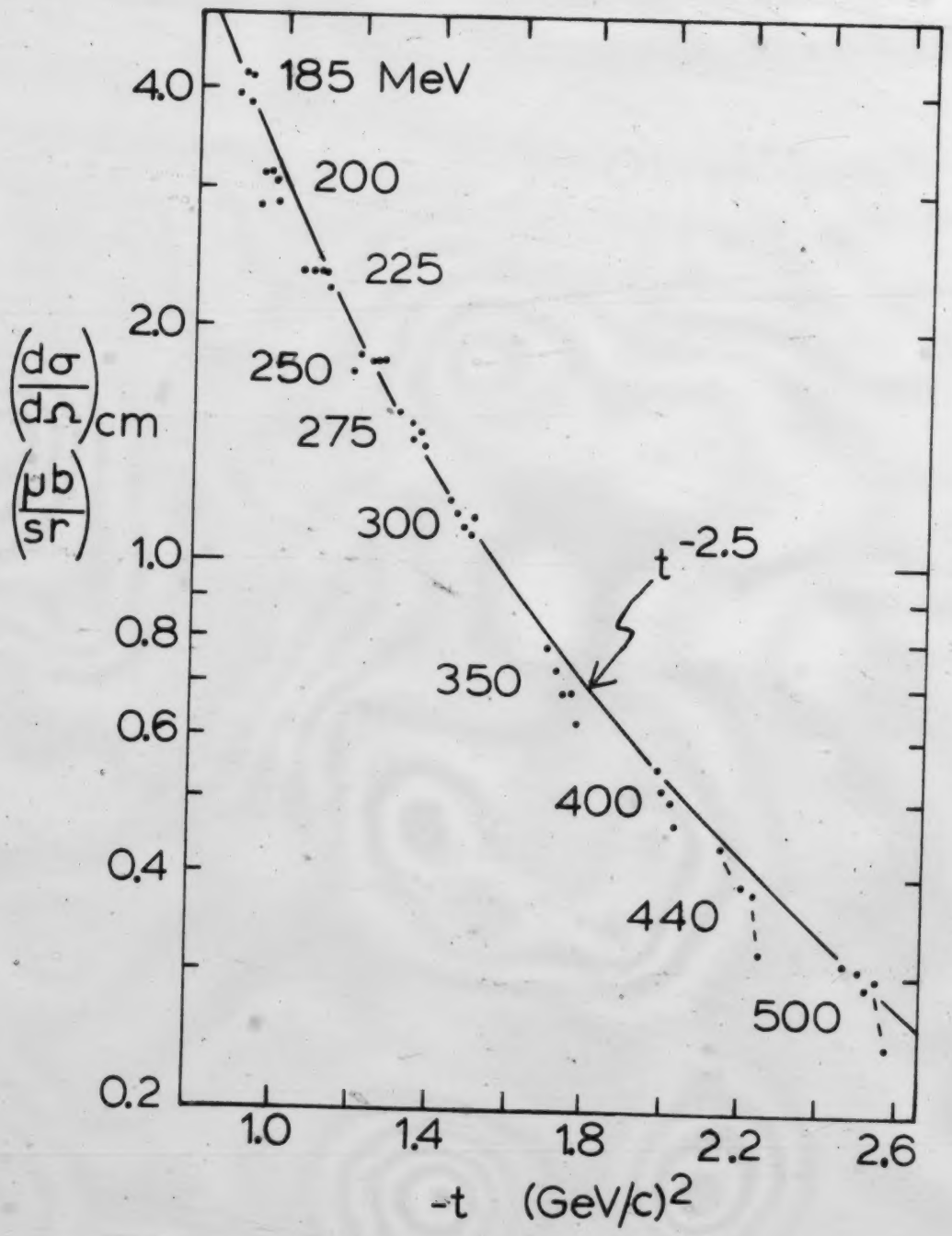

FIGURE 38. The elastic scattering differential cross sections as a function of the variable '-t'. The curve proportional to $t^{-2.5}$ is purely phenomenological, to show the trends of the data.

pendence $(-t)^{-2.5}$, which is seen to represent the data very well, is purely phenomenological, to show the trends of the data. The dependence on t, the momentum transfer squared between the two protons, suggests that some form of direct scattering may be the dominant reaction mechanism. A complete, theoretical calculation will be necessary to confirm or reject this supposition, however.

The cross sections for the $^4He(p,d)^3He$ reaction (see Appendix A for a full discussion of these data) are similarly plotted as functions of u and (-t) in Figures 39 and 40. In contrast to the elastic scattering cross sections just discussed, the (p,d) cross sections show a general dependence on u. However, a unique dependence on t is clearly not present. The cross sections decrease from energy to energy, but increase at a given energy as a function of (-t).

Figure 41(a) presents the diagram for p-^{4}He elastic scattering in terms of triton exchange (Section 4.1). In direct analogy, Figure 41(b) presents a diagram for $^4He(p,d)^3He$ in terms of deuteron exchange. If the $^4He(p,d)$ reaction does proceed via deuteron exchange, a general dependence of the cross section on the function $(u - M_D^2)^{-2}$ (Du-74) is to be expected. This function is plotted in Figure 39 and does, indeed, follow the cross sections very closely. This suggests that the reaction may proceed via deuteron exchange, although this argument could be modified by complications such as absorption effects.

In Appendix A, the similarities of the 180^0 excitation functions for the reactions $^4He(p,d)^3He$ and $^3He(p,p)^3He$ were noted.

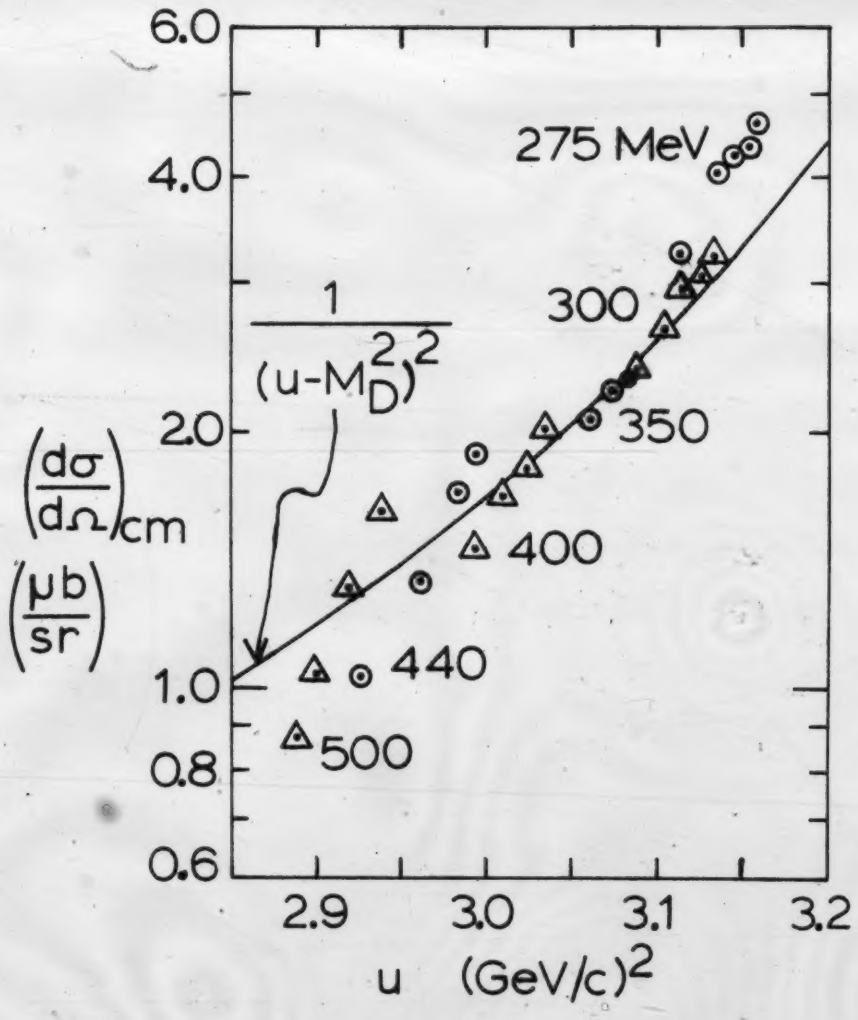

FIGURE 39. The $^4He(p,d)^3He$ differential cross sections as a function of the variable 'u'. The curve shows the u-dependence expected if the reaction is dominated by deuteron exchange.

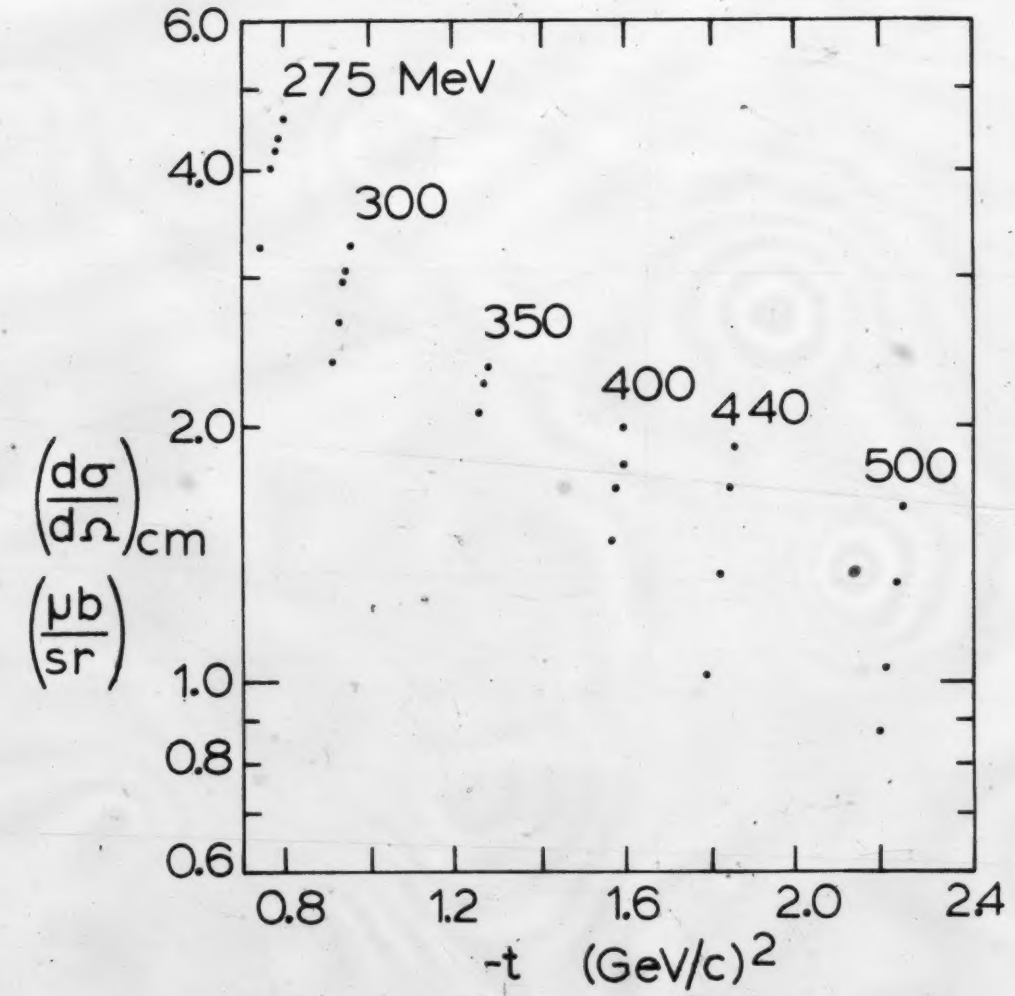

FIGURE 40. The $^4He(p,d)^3He$ differential cross sections as a function of the variable '-t'.

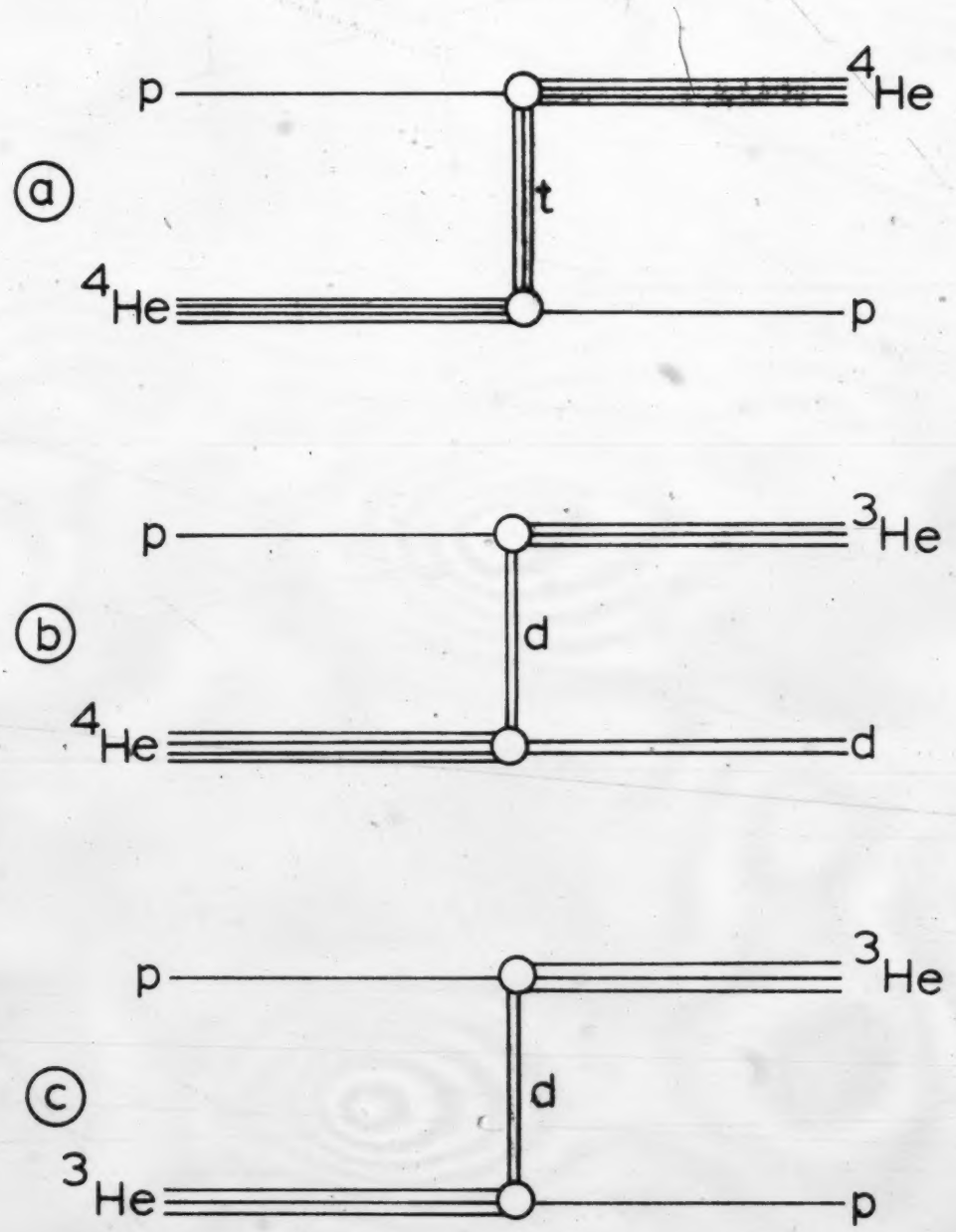

FIGURE 41. (a) The triton exchange diagram for p-^{4}He elastic scattering. (b) The deuteron exchange diagram for the reaction p + ^{4}He → d + ^{3}He. (c) The deuteron exchange diagram for p-^{3}He elastic scattering.

Figure 41(c) presents a possible reaction mechanism for p-^{3}He elastic scattering, which could also proceed via deuteron exchange. The only difference between Figure 41 (b) and (c) is an extra neutron in Figure 41(b). If this extra neutron is largely a spectator and takes a very small role in the reaction, then the two reactions would proceed almost identically, explaining the close similarities between the two reactions.

CHAPTER V

CONCLUSIONS

We have measured differential cross sections for proton-^{4}He elastic scattering for 10 proton energies between 185 and 500 MeV, from 144^0 to 168^0 in the laboratory system. The elastic scattering analyzing powers were obtained at 7 energies in this range. Data has also been presented for the reaction $^4He(p,d)^3He$ in the same angular region, consisting of differential cross sections at 6 energies $\geq$ 275 MeV, and analyzing powers at 3 beam energies.

The experimental arrangement provided kinematic redundancy in the definition of desired events, which resulted in negligible backgrounds in the regions of interest. The experiment featured good counting statistics, with a large majority of the cross sections having statistical uncertainties smaller than 3%. An accurate, absolute normalization of the data was obtained, including a direct, in-beam measurement of the effective thickness of the cryogenic ^{4}He target.

The elastic scattering differential cross sections do not exhibit the backward peaking that has been observed at both lower and higher energies, but, instead, are approximately constant or slowly decreasing with angle at most of the energies measured. The elastic scattering analyzing powers are large and negative, and show strong dependence on both energy and angle. The possible structure in the 180^0 elastic scattering excitation function suggested for

energies near 240 MeV is not observed in the data. However, distinct changes in the cross section angular distributions, the analyzing power angular distributions, and the 180^0 excitation function are all evident near 200 MeV.

The ^{4}He(p,d) differential cross sections display strong backward peaking. The ^{4}He(p,d) analyzing powers are small and negative, and show less energy dependence than do the elastic scattering analyzing powers. The ^{4}He(p,d) excitation function at 180^0 is very similar to that of the reaction ^{3}He(p,p) over the range of energies of the present experiment. One possible explanation for this fact is that the extra neutron in ^{4}He (compared to ^{3}He) could act largely as a spectator in a deuteron exchange process.

Further theoretical studies of p-^{4}He backward elastic scattering are clearly indicated. Existing triton exchange model calculations do not appear to describe the data well at low energies ($E \leq 300$ MeV). Possible extensions to the calculations, including better absorption approximations and the inclusion of spin dependent interactions, might, however, improve the agreement with the data. In addition, calculations of the direct scattering process, triton exchange-direct scattering interference contributions, and multiple scattering processes would assist in clarifying the reaction mechanisms involved in this energy range. In particular, the comparison of theoretical predictions with the measured analyzing powers would be useful and possibly very crucial tests in selecting a dominant reaction mechanism.

Experimentally, very few polarizations, or analyzing powers have been measured in the intermediate energy region. In particular, analyzing powers for $^{3}He(p,p)^{3}He$ at backward angles would be most interesting for comparison with the present $^{4}He(p,d)^{3}He$ analyzing powers. Another, most interesting experiment would be the extension of the present study from 500 to approximately 650 MeV to explore the emergence of the strong backward peak previously observed at 648 MeV, but not seen in the present data at 500 MeV. The backward peaking must grow rapidly above 500 MeV, and a search over a fine energy grid between 500 and 650 MeV, similar to the present search between 185 and 300 MeV, would prove very interesting indeed. An existing triton exchange model follows the backward peak quite well at 648 MeV, and such an experiment would investigate whether the triton exchange model will be in agreement with the details of the emergence of this backward peak. This would aid in clarifying whether triton exchange is the dominant mechanism in the region. Other suggestions for future interesting experiments include: (1) a comprehensive study of backward elastic scattering of protons from light nuclei, such as ^{3}He and ^{3}H, similar to the present study of p-^{4}He elastic scattering, and (2) the measurement of complete angular distributions of cross sections and analyzing powers for proton scattering from ^{4}He and other light nuclei in this energy range.

REFERENCES

REFERENCES

Al-72 J.C. Alder, W. Dollhoff, C. Lunke, C.F. Perdrisat, W.K. Roberts, P. Kitching, G. Moss, W.C. Olsen, and J.R. Priest, Phys. Rev. C6 (1972) 2010.

Am-77 C. Amsler, TRIUMF BASQUE group, private communication, (1977). See also G.A. Ludgate, Ph.D. Thesis, University of London (Bedford College), (1976) unpublished.

Ar-75 R.G. Arnold, B.T. Chertok, E.B. Dally, A. Grigorian, C.L. Jordan, W.P. Schutz, R. Zdarko, F. Martin, and B.A. Mecking, Phys. Rev. Lett. 35 (1975) 776.

Ar-77 R.G. Arnold, B.T. Chertok, S. Rock, W.P. Schutz, Z.M. Szalata, D. Day, J.S. McCarthy, F. Martin, B.A. Mecking, I. Sick, and G. Tamas, Proc. Seventh Int. Conf. on High Energy Physics and Nuclear Structure, Zurich (1977), p. 250.

As-77 E. Aslanides, T. Bauer, R. Bertini, R. Beurtey, A. Boudard, F. Brochard, G. Bruge, A. Chaumeaux, H. Catz, J.M. Fontaine, R. Frascaria, D. Garreta, P. Gorodetzky, J. Guyot, F. Hibou, D. Legrand, M. Matoba, Y. Terrien, J. Thirion, and E. Lambert, Phys. Lett. 68B (1977) 221.

Ba-67 R.H. Bassel and C. Wilkin, Phys. Rev. Lett. 18 (1967) 871; R.H. Bassel and C. Wilkin, Phys. Rev. 174 (1968) 1179.

Ba-72 G.W. Barry, Ann. Phys. (N.Y.) 73 (1972) 482.

Ba-74 S.D. Baker, R. Beurtey, G. Bruge, A. Chaumeaux, J.M. Durand, J.C. Faivre, J.M. Fontaine, D. Garreta, D. Legrand, J. Saudinos, J. Thirion, R. Bertini, F. Brochard, and F. Hibou, Phys. Rev. Lett. 32 (1974) 839. See also Phys. Today 27, No. 5 (1974) 20.

Ba-75 R.J. Barrett, B.D. Anderson, H.B. Willard, A.N. Anderson, and N. Jarmie, Nucl. Inst. and Meth. 129 (1975) 441.

Be-75 R. Beurtey, in High Energy Physics and Nuclear Structure-1975, edited by D.E. Nagle, A.S. Goldhaber, C.K. Hargrave, R.L. Burman, and B.G. Storms (American

Institute of Physics, New York, 1975), p. 653.

Be-76a J. Berger, J. Duflo, L. Goldzahl, F. Plouin, J. Oostens, M. Van Den Bossche, L. Vu Hai, G. Bizard, C. Le Brun, F. L. Fabbri, P. Picozza, and L. Satta, Phys. Rev. Lett. 37 (1976) 1195.

Be-76b J. Berger, J. Duflo, L. Goldzahl, F. Plouin, J. Oostens, M. Van Den Bossche, L. Vu Hai, G. Bizzard, C. Le Brun, F.L. Fabbri, P. Picozza, and L. Satta, Phys. Lett. 63B (1976) 111.

Bo-68 E.T. Boschitz, W.K. Roberts, J.S. Vincent, K. Gotow, P.C. Gugelot, C.F. Perdrisat, and L.W. Swenson, Phys. Rev. Lett. 20 (1968) 1116; E.T. Boschitz, W.K. Roberts, J.S. Vincent, M. Blecher, K. Gotow, P.C. Gugelot, C.F. Perdrisat, L.W. Swenson, and J.R. Priest, Phys. Rev. C6 (1972) 457; E.T. Boschitz, in High Energy Physics and Nuclear Structure, edited by S. Devons (Plenum Press, New York, 1970), p. 288.

Bu-70 S. Buhler, Proc. Int. Conf. on Cryogenic Engineering, Berlin (1970), p. 306.

Ca-75 E.B. Cairns and W.K. Dawson, IEEE Trans. Nucl. Sci. NS-22 (1975) 301.

Ca-77 J.M. Cameron, P. Kitching, R.H. McCamis, C.A. Miller, G.A. Moss, J.G. Rogers, G. Roy, A.W. Stetz, C.A. Goulding, and W.T.H. Van Oers, Nucl. Inst. and Meth. 143 (1977) 399.

Ch-72 G. Charpak, H.G. Fisher, C.R. Gruhn, A. Minten, F. Sauli, G. Plch, and G. Flugge, Nucl. Inst. and Meth. 99 (1972) 279.

Co-59 A.M. Cormack, J.N. Palmieri, N.F. Ramsey, and R. Wilson, Phys. Rev. 115 (1959) 599; see also an erratum in J.N. Palmieri, R. Goloskie, and A.M. Cormack, Phys. Lett. 6 (1963) 289.

Co-75 V. Comparat, R. Frascaria, N. Fujiwara, N. Marty, M. Morlet, P.G. Roos, and A. Willis, Phys. Rev. C12 (1975) 251.

Cr-69 N.S. Craigie and C. Wilkin, Nucl. Phys. B14 (1969) 477.

Cz-67 W. Czyz and L. Lesniak, Phys. Lett. 24B (1967) 227.

Da-67 B.W. Davies, M.K. Craddock, R.C. Hanna, Z.J. Moroz, and L.P. Robertson, Nucl. Phys. A97 (1967) 241.

Du-74 L. Dubal and C.F. Perdrisat, Lett. al Nuovo Cimento 11 (1974) 265.

Fa-76 J. Fain, J. Gardes, A. Lefort, L. Meritet, J.F. Pauty, G. Peynet, M. Querrou, F. Vazeille, and B. Ille, Nucl. Phys. A262 (1976) 413.

Fi-73 S. Fiarman and W.E. Meyerhof, Nucl. Phys. A206 (1973) 1.

Fr-67 R.F. Frosch, J.S. McCarthy, R.E. Rand, and M.R. Yearian, Phys. Rev. 160 (1967) 874.

Fr-77 R. Frascaria, I. Brissaud, N. Marty, M. Morlet, F. Reide, A. Willis, R. Beurtey, A. Boudard, M. Garcon, G.A. Moss, Y. Terrien and W.T.H. Van Oers, Phys. Lett. 66B (1977) 329.

Ge-77 J.V. Geaga, M.M. Gazzaly, G.J. Igo, J.B. McClelland, M.A. Nasser, A.L. Sagle, H. Spinka, J.B. Carroll, V. Perez-Mendez, and E.T.B. Whipple, Phys. Rev. Lett. 38 (1977) 1265.

Go-68 K. Gotow, E.T. Boschitz, W.K. Roberts, J.S. Vincent, P.C. Gugelot, C.F. Perdrisat, and L.W. Swenson, Phys. Rev. Lett. 21 (1968) 1816.

Go-70 N.P. Goldstein, A. Held, and D.G. Stairs, Can. J. Phys. 48 (1970) 2629.

Gu-75 S.A. Gurvitz, Y. Alexander, and A.S. Rinat, Phys. Lett. 59B (1975) 22.

Gu-75a S.A. Gurvitz, Y. Alexander, and A.S. Rinat, Ann. Phys. (N.Y.) 93 (1975) 152.

Gu-76 S.A. Gurvitz, Y. Alexander, and A.S. Rinat, Ann. Phys. (N.Y.) 98 (1976) 346.

Ig-75 G. Igo, in High Energy Physics and Nuclear Structure -1975, edited by D.E. Nagle, A.S. Goldhaber, C.K. Hargrave, R.L. Burman, and B.G. Storms (American Institute of Physics, New York, 1975), p. 63.

Ik-72 M. Ikeda, Phys. Rev. C6 (1972) 1608.

Ke-69 A.K. Kerman and L.S. Kisslinger, Phys. Rev. 180 (1969) 1483.

Kl-77 R. Klem, G. Igo, R. Talaga, A. Wriekat, H. Courant, K. Einsweiler, T. Joyce, H. Kagan, Y. Makdisi, M. Marshak, B. Mossberg, E. Peterson, K. Ruddick, and T. Walsh, Phys. Lett. 70B (1977) 155.

Kl-77a R. Klem, G. Igo, R. Talaga, A. Wriekat, H. Courant, K. Einsweiler, T. Joyce, H. Kagan, Y. Makdisi, M. Marshak, B. Mossberg, E. Peterson, K. Ruddick, and T. Walsh, Phys. Rev. Lett. 38 (1977) 1272.

Ko-70 V.I. Komarov, G.E. Kosarev, and O.V. Savchenko, Sov. J. Nucl. Phys. 11 (1970) 399.

Ko-71 B.Z. Kopeliovich and I.K. Potashnikova, Sov. J. Nucl. Phys. 13 (1971) 592.

Ko-73a V. I. Komarov, G.E. Kosarev, G.P. Reshetnikov, and O.V. Savchenko, Sov. J. Nucl. Phys. 16 (1973) 129.

Ko-73b V.M. Kolybasov and N. Ya. Smorodinskaya, Sov. J. Nucl. Phys. 17 (1973) 630.

Ku-70 E. Kujawski, Phys. Rev. C1 (1970) 1651.

Le-76 H. Lesniak, L. Lesniak, and A. Tekou, Nucl. Phys. A267 (1976) 503.

Lo-70 W.O. Lock and D.F. Measday, Intermediate Energy Nuclear Physics, (Methuen and Co., London, 1970).

McM-65 P.G. McManigal, R.D. Eandi, S.N. Kaplan, and B.J. Moyer, Phys. Rev. 137 (1965) B620.

No-74 J.V. Noble and H.J. Weber, Phys. Lett. 50B (1974) 233.

Pa-67 H. Palevsky, in High Energy Physics and Nuclear Structure, edited by G. Alexander (North Holland Publishing Co., Amsterdam, 1967), p. 151; H. Palevsky, J.L. Friedes, R.J. Sutter, G.W. Bennett, G.J. Igo, W.D. Simpson, G.C. Phillips, D.M. Corley, N.S. Wall, R.L. Stearns, and B. Gottschalk, Phys. Rev. Lett. 18 (1967) 1200.

Ri-65 J.R. Richardson, Progress in Nuclear Techniques and Instrumentation 1 (1965) 1.

Ri-73 J.R. Richardson, IEEE Trans. Nucl. Sci. NS-20 (1973) 207.

Ri-75 J.R. Richardson, E.W. Blackmore, G. Dutto, C.J. Kost, G.H. Mackenzie, and M.K. Craddock, IEEE Trans. Nucl. Sci. NS-22 (1975) 1402.

Ro-72 G. Roy, University of Alberta Internal Report UAE-NPL-53 (1972) unpublished.

Ro-74 J.G. Rogers, TRIUMF Design Note TRI-DNA-74-4 (1974) unpublished.

Ro-75 G. Roy, J. Beveridge, and P. Bosman, Proc. Fourth Int. Symp. on Polarization Phenomena in Nuclear Reactions, Zurich (1975), p. 862.

Ro-75a J.G. Rogers, TRIUMF Design Note TRI-DNA-75-3 (1975) unpublished.

Ro-75b J.G. Rogers, TRIUMF Design Note TRI-DNA-75-13 (1975) unpublished.

Ro-77 J.G. Rogers, TRIUMF Design Note TRI-DN- 77-5 (1977) unpublished.

Sh-74 J.S. Sharma and A.N. Mitra, Phys. Rev. D9 (1974) 2547; J.S. Sharma, V.S. Bhasin, and A.N. Mitra, Nucl. Phys. B35 (1971) 466.

St-75 A.W. Stetz, TRIUMF Design Note TRI-DNA-75-4 (1975) unpublished.

St-77 A.W. Stetz, J.M. Cameron, D.A. Hutcheon, R.H. McCamis, C.A. Miller, G.A. Moss, G. Roy, J.G. Rogers, C.A. Goulding, and W.T.H. Van Oers, Nucl. Phys.-Int. Energy, to be published (1977).

Ve-75 S.L. Verbeck, J.C. Fong, G. Igo, C.A. Whitten, Jr., D.L. Hendrie, Y. Terrien, V. Perez-Mendez, and G.W. Hoffman, Phys. Lett. 59B (1975) 339.

Vi-70 J.S. Vincent, W.K. Roberts, E.T. Boschitz, L.S. Kisslinger, K. Gotow, P.C. Gugelot, C.F. Perdrisat, L.W. Swenson, and J.R. Priest, Phys. Rev. Lett. 24 (1970) 236.

Vo-66 E.W. Vogt and J.R. Richardson, IEEE Trans. Nucl. Sci. NS-13 (1966) 262.

Vo-74 L.G. Votta, P.G. Roos, N.S. Chant, and R. Woody III, Phys. Rev. C10 (1974) 520.

Wa-70 J.B. Warren, in High Energy Physics and Nuclear Structure, edited by S. Devons (Plenum Press, New York, 1970), p. 566.

Wa-71 J.B. Warren, Proc. Fifth Int. Cyclotron Conference edited by R.W. McIlroy (Butterworths, London, 1971), p. 73.

Wa-77 S.J. Wallace and Y. Alexander, Phys. Rev. Lett. 38 (1977) 1269.

Wa-77a S.J. Wallace, private communication, (1977).

We-77 H.J. Weber and H. Arenhovel, to be published, (1977).

APPENDIX A

$^{4}He(p,d)^{3}He$ DIFFERENTIAL CROSS SECTIONS AND ANALYZING POWERS

APPENDIX A

$^4He(p,d)^3He$ DIFFERENTIAL CROSS SECTIONS AND ANALYZING POWERS

1. The Differences between $^4He(p,p)$ and $^4He(p,d)$

Together with the acquisition of the p-^{4}He elastic scattering data, a large body of data on the reaction $^4He(p,d)^3He$ was obtained. The analysis of this data was almost identical to that of the elastic scattering data (Section 2.6), except for a few departures to be discussed below.

An important difference between the two reactions was that the kinematics for the (p,d) reaction were slightly different from elastic scattering kinematics. For example, at 500 MeV, one position for the back detectors was 154^0. The front detectors were then placed at 9^0, according to elastic scattering kinematics. But, the ^{3}He particles corresponding to 154^0 deuterons are produced at 8.3^0 (or, conversely, 9^0 ^{3}He's correspond to 152^0 deuterons). When the data was analyzed, however, the angular correlation of the (p,d) events for the FR-BL detector combination exhibited a larger offset than was expected from the kinematic differences. The data for the FL-BR detector combination showed a smaller offset than expected. One possible explanation is that the proton beam passed through the target at an angle of approximately 0.25^0, caused by a curvature of the beam by the fringe field of the main cyclotron. Alternatively,

a lateral displacement of the beam on target by 2-3 mm to the left would account for the observations.

These effects were only significant when a large kinematic difference for the (p,d) events and the beam misalignment combined to place ^{3}He particles, corresponding to deuterons entering a central MWPC window, near the edge of the FR plastic detector. (The two effects tended to cancel each other for the other detector combination.) In such cases, both of the defining MWPC windows were moved to a smaller (deuteron) angle, and the window size was decreased.

At certain energies, the (p,d) reaction products may have been partially rejected by lower level discriminators. At 275 and 300 MeV, the backward deuterons had very low energies (as low as 21 MeV at the NaI detectors), and the NaI discriminators may have rejected some valid events. The forward-going ^{3}He particles at 500 MeV also produced signals close to the discriminator levels on the front plastic scintillators. Thus, the cross sections at 275, 300 and 500 MeV should be regarded as lower limits only, albeit reasonably accurate lower limits. At both 300 and 500 MeV, the discriminator levels, while close, did not noticeably affect the energy spectra in question. At 275 MeV, however, the left (BL) NaI discriminator was definitely cutting into the events. Therefore, the 275 MeV cross sections were calculated from the BR-FL data only (and thus have a (deuteron) production angle uncertainty of $\pm 0.25^0$).

One further difference for the (p,d) data was the fact that events were located in a region of higher background than were the elastic scattering events (see Figure 19, Section 2.6). Standard

analysis (Section 2.6) eliminated this background, except for the 440 MeV data. Analysis of the only target empty run at 440 MeV ($\theta_d = 168^0$) gave a background of approximately 2% of the full target yield, appropriately normalized. This proportion of background events was subtracted from each data point at 440 MeV.

The deuterons incident on the NaI detectors had energies between 21 and 64 MeV, after energy losses from 9 to 15 MeV between the target and the NaI. The efficiencies of the NaI counters for detecting deuterons in this energy range were calculated from optical model predictions for the total reaction cross sections for deuterons in sodium and iodine (Gi-77). The calculated inefficiencies ranged from less than 1% to approximately 5%. The associated uncertainty was at most 20% of the inefficiency, or less than 1% uncertainty in the cross section.

Except for this efficiency uncertainty, the other uncertainties in the cross section, discussed in Section 3.2 for the elastic scattering cross sections are identical for the (p,d) cross sections presented below. The uncertainties in the 275, 300 and 500 MeV cross sections due to the possibility of electronic elimination of valid events are difficult to assess, but it is estimated that cross section increases of the order of 10% for these data points would be the maximum increases expected.

The uncertainties in the analyzing powers are identical to the uncertainties in the elastic scattering analyzing powers (Section 3.2).

2. Data Presentation and Discussion

The cross sections for the reaction $^4He(p,d)^3He$, measured at 275, 300, 350, 400, 440 and 500 MeV, are presented in Table 9 and are illustrated in Figure 42 versus $\cos \Theta_{cm}$ and Θ_{cm}.

The most striking feature of the data is the backward peaking of the cross sections. Backward peaking is evident at 275 MeV, and increases with energy to 500 MeV, where the peaking is quite sharp. This backward peaking of the cross section is in marked contrast to the trend seen in the elastic scattering cross sections. There, the cross section angular distributions are nearly constant at lower energies and tend to decrease, not increase with angle, as the energy rises.

Another, very significant difference between the $^4He(p,d)$ and $^4He(p,p)$ cross sections is their absolute magnitude, which is much larger for the (p,d) reaction. This is illustrated in Figure 43, which presents the ratio of the 180^0 extrapolated cross section for the $^4He(p,d)$ reaction (obtained via the procedure described in Section 3.3) to the elastic scattering cross section at each incident proton energy.

The $^3He(p,p)^3He$ backward cross sections have been measured recently at 415, 600 and 800 MeV by Frascaria *et al.* (Fr-77) and at 156 MeV by Langevin-Joliot *et al.* (La-70). The ratio of the $^4He(p,d)^3He$ 180^0 cross section to the $^3He(p,p)^3He$ 180^0 cross section at the same beam energy (obtained from (Fr-77)) is also presented in Figure 43. All the values plotted in Figure 43 are ratios of two extrapolated

TABLE 9

^{4}He(p,d) Cross Sections

Beam Energy (MeV)	θ_{lab} (degrees)	θ_{cm} (degrees)	cos θ_{cm}	$(\frac{d\sigma}{d\Omega})_{lab}$ (μb/sr)	$(\frac{d\sigma}{d\Omega})_{cm}$ (μb/sr)	Statistical Uncertainty (%)	-t (GeV/c)^2	u (GeV/c)^2	$\frac{d\sigma}{dt}$† (μb/(GeV/c)^2)
275*	144.0	159.5	-0.937	1.19	3.24	2.3	0.754	3.114	25.7
	152.0	164.3	- .963	1.36	4.03	2.5	.774	3.135	32.0
	158.0	167.8	- .977	1.36	4.21	1.9	.786	3.146	33.5
	163.0	170.6	- .987	1.35	4.33	1.7	.793	3.154	34.4
	168.0	173.4	- .993	1.40	4.60	2.6	.798	3.159	36.5
300*	146.0	160.8	- .944	0.850	2.37	2.4	.916	3.090	17.2
	152.0	164.3	- .963	.895	2.65	3.2	.932	3.106	19.2
	157.0	167.2	- .975	.954	2.94	3.8	.943	3.117	21.3
	163.0	170.6	- .987	.946	3.04	2.8	.953	3.127	22.0
	168.0	173.4	- .993	.987	3.25	2.1	.959	3.133	23.5
350	156.2	166.8	- .974	.673	2.08	2.2	1.260	3.062	12.8
	162.2	170.2	- .985	.703	2.26	1.9	1.272	3.074	13.9
	167.2	173.0	- .993	.709	2.34	2.2	1.280	3.081	14.4
400	151.3	164.0	- .961	.485	1.45	2.5	1.566	2.995	7.72
	156.3	166.9	- .974	.540	1.68	2.4	1.581	3.010	8.98
	162.0	170.2	- .985	.555	1.80	1.7	1.594	3.023	9.59
	168.0	173.5	- .994	.592	1.98	1.7	1.604	3.033	10.5

TABLE 9 (continued)

Beam Energy (MeV)	θ_{lab} (degrees)	θ_{cm} (degrees)	$\cos\theta_{cm}$	$(\frac{d\sigma}{d\Omega})_{lab}$ (μb/sr)	$(\frac{d\sigma}{d\Omega})_{cm}$ (μb/sr)	Statistical Uncertainty (%)	-t (GeV/c)^2	u (GeV/c)^2	$\frac{d\sigma}{dt}$† (μb/(GeV/c)^2)
440	145.0	160.4	-0.942	0.360	1.01	3.1	1.797	2.927	4.90
	154.0	165.7	- .969	.432	1.33	1.9	1.832	2.962	6.42
	162.0	170.2	- .985	.517	1.69	1.7	1.853	2.984	8.14
	168.0	173.5	- .994	.556	1.87	1.8	1.864	2.994	9.01
500*	150.6	163.8	- .960	.287	0.869	1.6	2.206	2.889	3.66
	153.6	165.5	- .968	.332	1.03	1.3	2.217	2.900	4.35
	159.6	168.9	- .981	.400	1.30	1.3	2.237	2.920	5.49
	167.6	173.3	- .993	.472	1.61	1.3	2.255	2.938	6.76

†$\frac{d\sigma}{dt} \equiv \frac{d\sigma}{du}$

*Cross sections at these energies should be regarded as lower limits only, due to the possibility that the reaction products may have been partially rejected by lower level discriminators (see text for a full discussion). The maximum cross section increases expected due to this problem would be of the order of 10%.

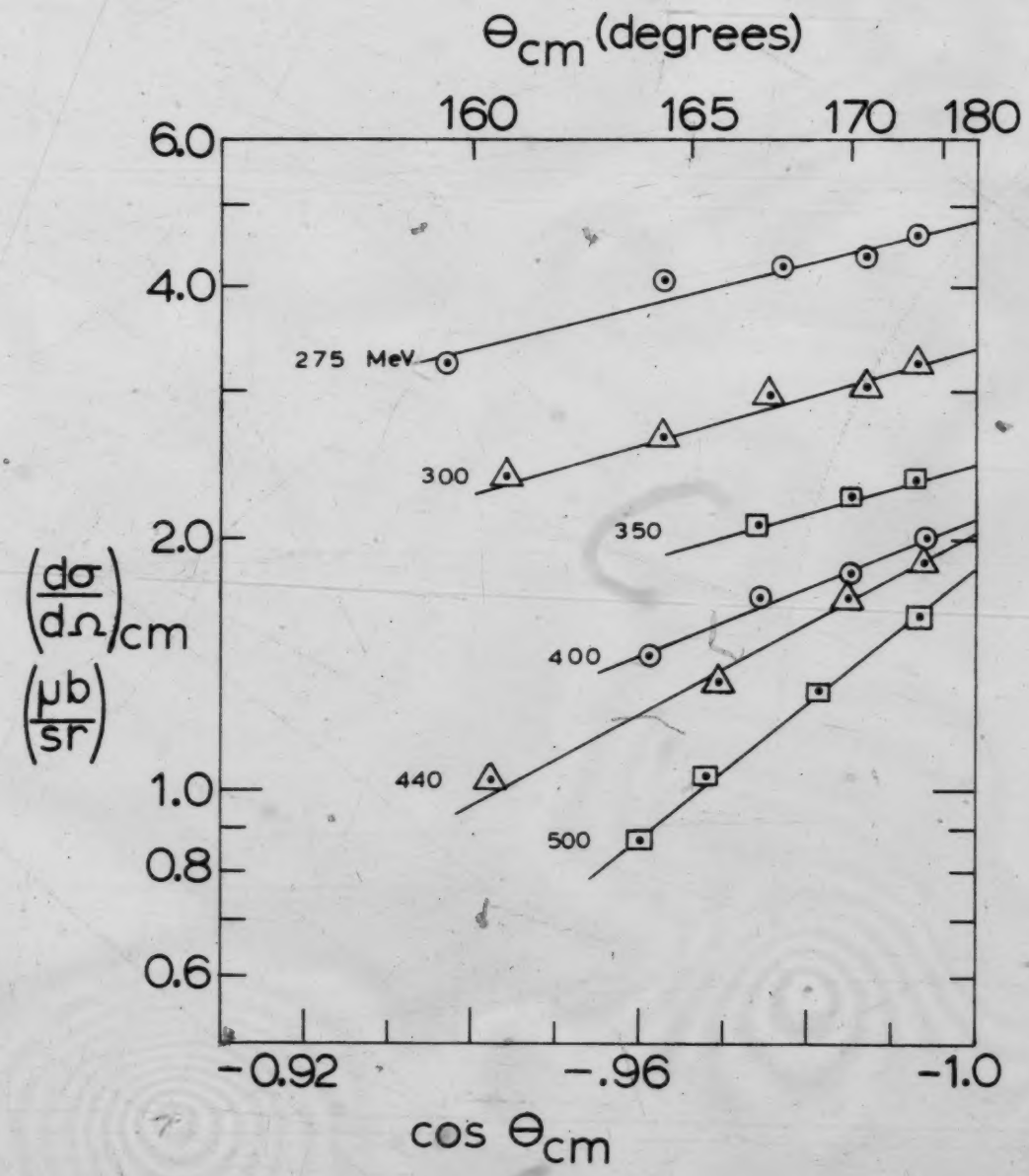

FIGURE 42. The differential cross sections for the reaction $^{4}He(p,d)^{3}He$ vs. cos θ_{cm} and θ_{cm}. The lines represent an exponential fit to the data as a function of cos θ_{cm}.

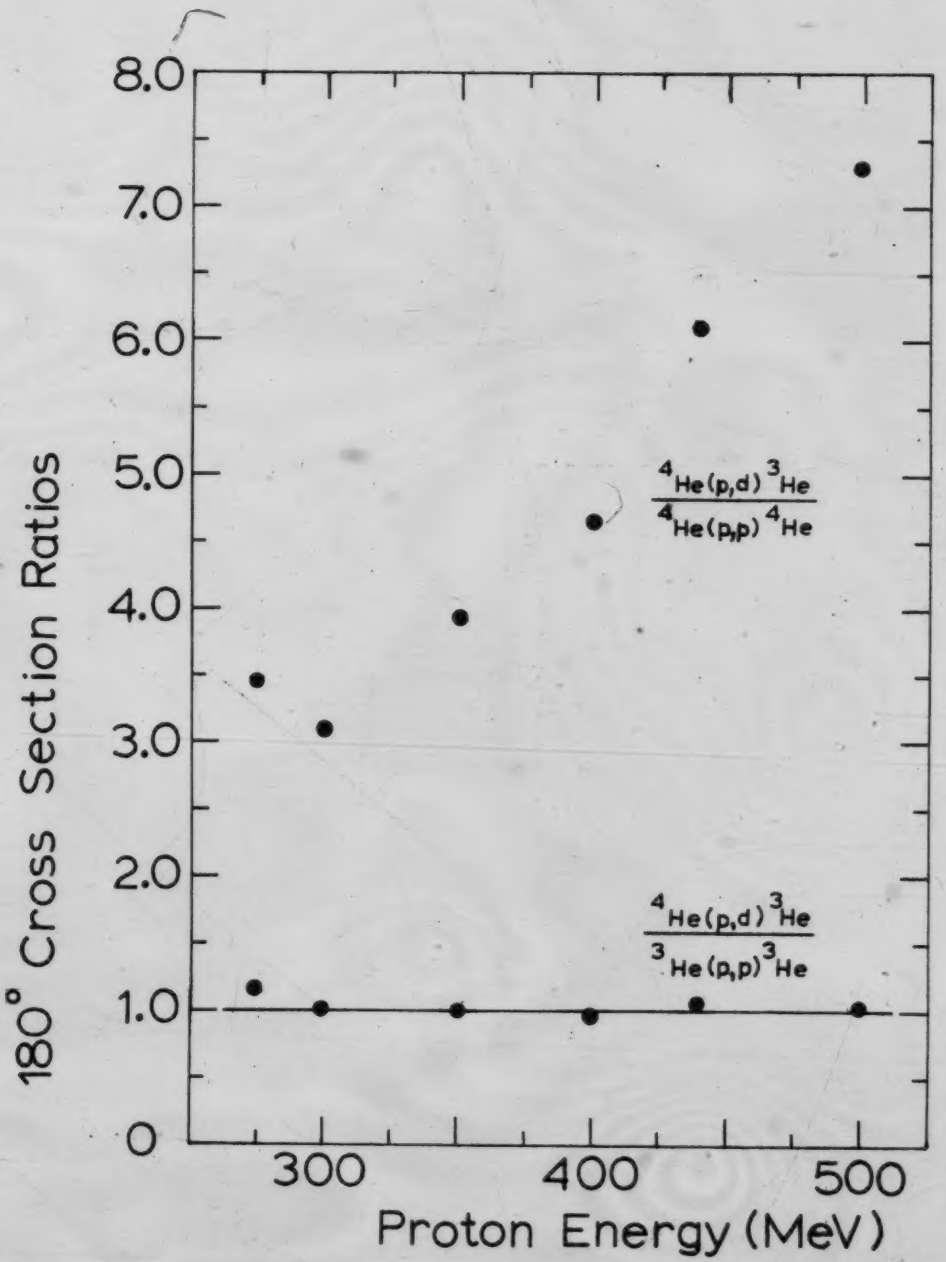

FIGURE 43. The ratios of the 180^0 extrapolated cross sections for the reactions indicated as a function of proton energy.

cross sections, and thus have intrinsic uncertainties; the points involving the ^{3}He(p,p) cross sections have somewhat larger uncertainties still, because of the energy interpolations between widely separated data points. The trends, however, are well established. As is evident in Figure 43, the ^{4}He(p,d)^{3}He and ^{3}He(p,p)^{3}He cross sections at 180^0 are very close to being equal at each energy. In addition, the ^{3}He(p,p)^{3}He angular distributions at 415 and 600 MeV (Fr-77) (which are very similar to each other) exhibit backward peaking which has approximately the same magnitude as the ^{4}He(p,d) angular distributions. These similarities strongly suggest that the two reaction mechanisms are analogous.

A limited number of ^{4}He(p,d)^{3}He analyzing powers were also measured at 350, 400 and 500 MeV; these analyzing powers are presented in Table 10 and are illustrated in Figure 44 (a to c) as functions of Θ_{lab}. The uncertainties illustrated are the statistical uncertainties only.

The ^{4}He(p,d) analyzing powers are negative, as were the ^{4}He(p,p) analyzing powers presented in Section 3.4, but are much smaller in magnitude than the elastic scattering analyzing powers. Another contrasting feature of the ^{4}He(p,d) analyzing powers is that they do not appear as energy-dependent as were the elastic scattering analyzing powers. The ^{4}He(p,d) analyzing powers are very similar at 400 and 500 MeV. The 350 MeV analyzing powers have magnitudes similar to the 400 and 500 MeV data, but exhibit a different angular dependence than the other data. This change in shape is not well established, however.

TABLE 10

^{4}He(p,d) Analyzing Powers

Beam Energy (MeV)	θ_{lab} (degrees)	Analyzing Power		
		Primary Calculation	Secondary Calculation	Statistical Uncertainty
350	156.2	-0.145	-0.145	0.031
	162.2	- .239	- .239	.031
	167.2	- .190	- .192	.030
400	151.3	- .214	- .215	.036
	156.3	- .210	- .222	.036
	162.0	- .155	- .152	.024
	168.0	- .105	- .118	.026
500	150.6	- .334	- .339	.031
	153.6	- .278	- .275	.025
	159.6	- .246	- .244	.025
	167.6	- .133	- .124	.024

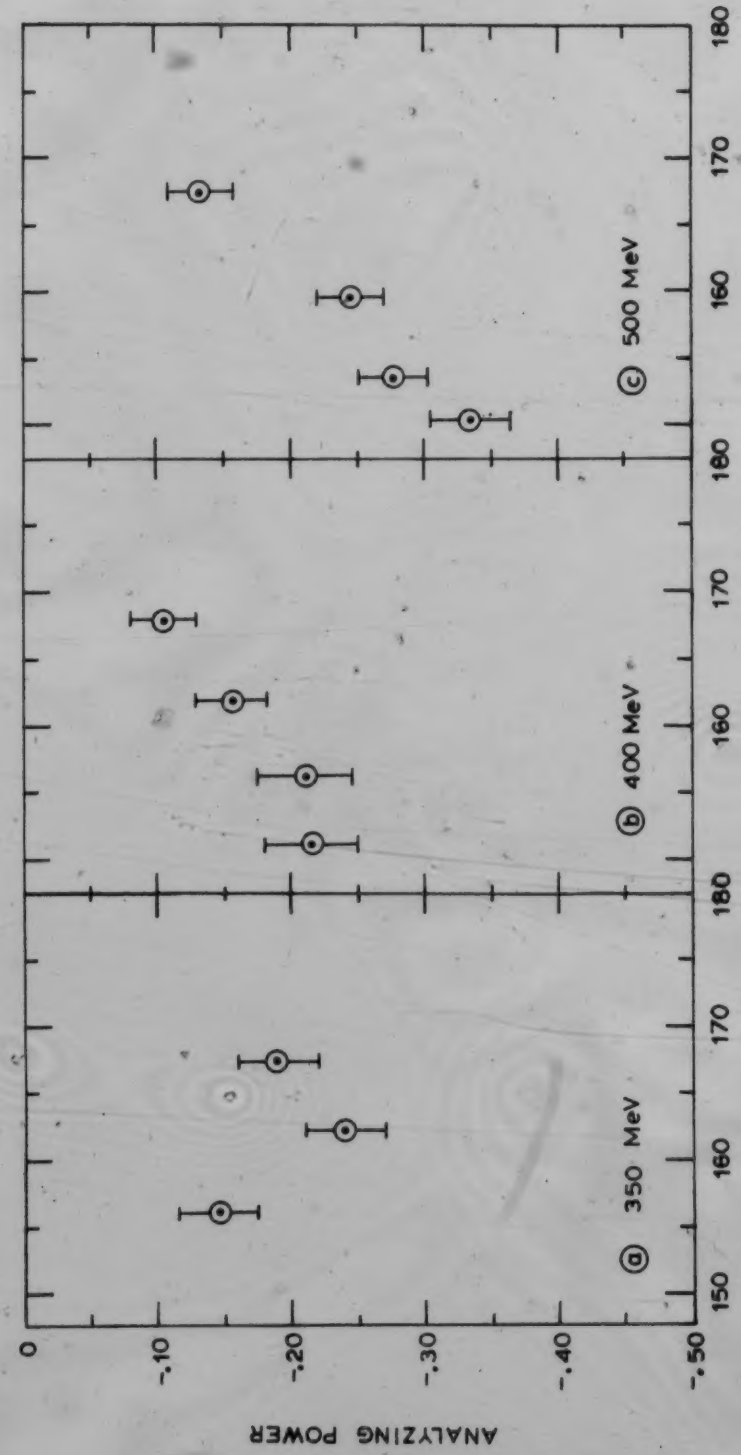

FIGURE 44. The analyzing powers for the reaction $^4He(p,d)^3He$ as a function of θ_{lab}, shown separately for each beam energy. The uncertainties shown are the statistical uncertainties only.

In the light of the great similarities in the backward cross sections for $^{4}He(p,d)$ and $^{3}He(p,p)$, analyzing power measurements for $^{3}He(p,p)$ could be very informative. A comparison between the analyzing powers for the two reactions in this energy region may significantly clarify the reaction mechanisms involved.

REFERENCES

Fr-77 R. Frascaria, I. Brissaud, N. Marty, M. Morlet, F. Reide, A. Willis, R. Beurtey, A. Boudard, M. Garcon, G.A. Moss, Y. Terrien and W.T.H. Van Oers, Phys. Lett. 66B (1977) 329.

Gi-77 D. Ginther and W.T.H. Van Oers, private communication, (1977).

La-70 H. Langevin-Joliot, Ph. Narboni, J.P. Didelez, G. Duhamel, L. Marcus, and M. Roy-Stephan, Nucl. Phys. A158 (1977) 309.

APPENDIX B

MANDELSTAM VARIABLES

APPENDIX B

MANDELSTAM VARIABLES

The Mandelstam variables s, t, and u are frequently the most convenient variables with which to describe intermediate and high energy processes in nuclear and particle physics. The definitions of these variables and some pertinent relationships between the Mandelstam variables and variables associated with the center of mass system are presented below. Rigorous derivations of the equations are not presented, but may be found in the references (Ha-64, Ma-70, and Wi-71) or in most textbooks on elementary particle theory. A system of units have been chosen such that $\hbar = c = 1$.

Consider the general process:

$$a + b \rightarrow c + d,$$

shown in Figure 45. The particles have rest masses m_i, for i = a, b, c, and d. They have three momenta $\vec{q}_i$ (with magnitudes q_i) and total energies E_i, given by:

$$E_i^2 = m_i^2 + q_i^2. \qquad \text{B.1}$$

The particles also have four-momenta k_i, defined by $k_i = (E_i, \vec{q}_i)$, where:

$$k_i^2 = E_i^2 - q_i^2 = + m_i^2. \qquad \text{B.2}$$

An additional requirement, the conservation of energy and momentum, is:

$$k_a + k_b = k_c + k_d. \qquad \text{B.3}$$

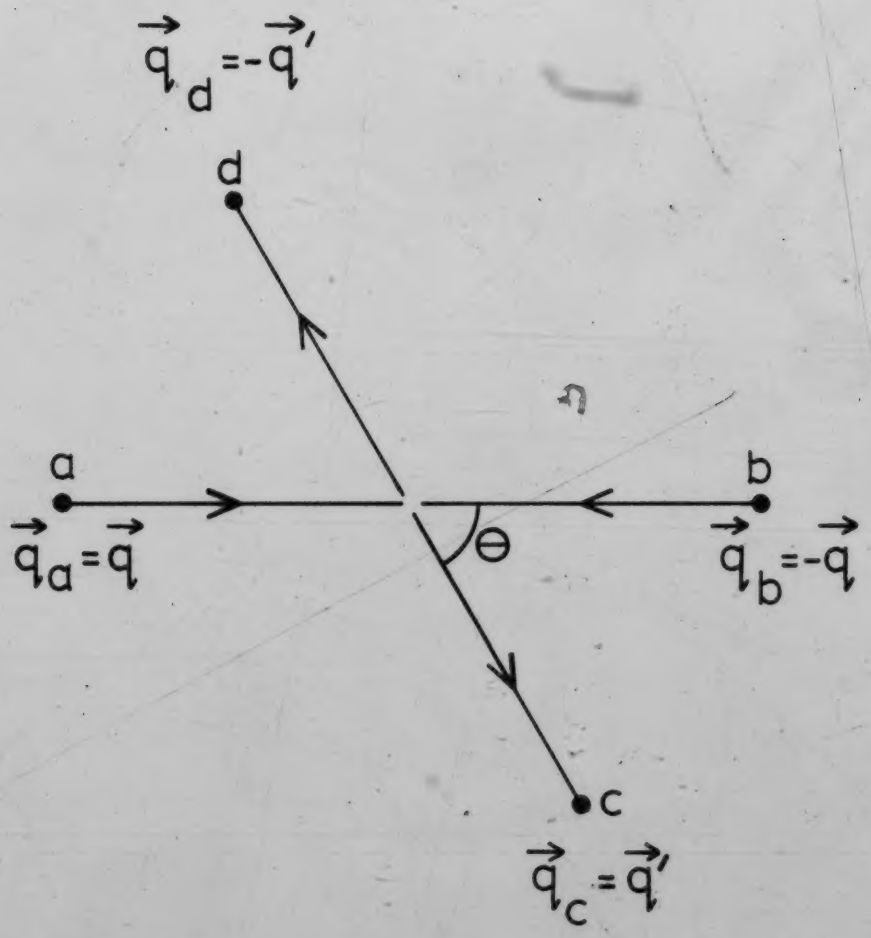

FIGURE 45. A diagram of the general process a + b → c + d, in the center of mass system.

The Mandelstam variables are defined as:

$$s \equiv (k_a + k_b)^2, \qquad \text{B.4}$$

$$t \equiv (k_a - k_c)^2, \text{ and} \qquad \text{B.5}$$

$$u \equiv (k_a - k_d)^2. \qquad \text{B.6}$$

The quantity s is the squared total center of mass energy of the system. The variable t (u) is the squared four-momentum transfer between particles a and c (a and d). It can be shown that:

$$s + t + u = m_a^2 + m_b^2 + m_c^2 + m_d^2. \qquad \text{B.7}$$

In the center of mass system (Figure 45), eq. B.5 and B.6 become:

$$t = m_a^2 + m_c^2 - 2E_aE_c + 2\,q\,q'\cos\theta, \qquad \text{B.8}$$

$$u = m_a^2 + m_d^2 - 2E_aE_d - 2\,q\,q'\cos\theta, \qquad \text{B.9}$$

where θ is the center of mass scattering angle.

For elastic scattering ($m_a = m_c$, $m_b = m_d$), then $|\vec{q}| = |\vec{q}'| = q$, $E_a = E_c$, and $E_b = E_d$. Then, eq. B.8 simplifies to:

$$t = -2q^2(1 - \cos\theta). \qquad \text{B.10}$$

u can either be calculated from eq. B.9 or, knowing t, from equations B.4 and B.7.

Another useful formula for t, which applies to elastic scattering in the laboratory system, is:

$$t = -2m_d T_{d_{LAB}}, \qquad \text{B.11}$$

where $T_{d_{LAB}}$ is the kinetic energy of particle 'd' in the laboratory system.

REFERENCES

Ha-64 R. Hagedorn, Relativistic Kinematics, (W. Benjamin Inc., New York, 1964).

Ma-70 A.D. Martin and T.D. Spearman, Elementary Particle Theory, (North Holland Publishing Co., Amsterdam, 1970).

Wi-71 W.S.C. Williams, An Introduction to Elementary Particles, (Academic Press, New York, 1971).